RADIATIVE TRANSFER THEORY FOR ACTIVE AND PASSIVE REMOTE SENSING OF SEA ICE

by

Hong Tat Ewe

B.Eng., University of Malaya, Malaysia
August 1992

Submitted in Partial Fulfillment
of the Requirements for the Degree of

MASTER OF SCIENCE

IN ELECTRICAL ENGINEERING AND COMPUTER SCIENCE

at the

MASSACHUSETTS INSTITUTE OF TECHNOLOGY

May 1994

Signature of Author _____
Department of Electrical Engineering and Computer Science
May 1994

Certified by _____
Professor Jin Au Kong
Thesis Supervisor

Certified by _____
Dr. Robert T. Shin
Thesis Supervisor

Accepted by _____
Professor Frederic R. Morgenthaler
Chairman, Departmental Committee on Graduate Students

RADIATIVE TRANSFER THEORY FOR ACTIVE AND PASSIVE REMOTE SENSING OF SEA ICE

by
Hong Tat Ewe

Submitted to the Department of Electrical Engineering and Computer Science
May 1994 in partial fulfillment for the requirements of the
degree of Master of Science

ABSTRACT

A large number of measurements at microwave frequencies have been carried out to study the feasibility of using airborne and spaceborne sensors to measure sea ice properties. However, in order to better interpret the electromagnetic signatures from sea ice, a good understanding of the scattering mechanisms involved is essential. In this thesis, a theoretical model is developed based on the sea ice physical properties. The sea ice is modeled as a multilayer structure where each layer has randomly orientated scatterers embedded in the pure ice background. The scatterers can model both the brine inclusions and the air bubbles.

The approach is to use the radiative transfer theory to solve for the fully polarimetric bistatic scattering coefficients for active remote sensing and the brightness temperatures for passive remote sensing. For two layer model, numerical method is applied where radiative transfer equations are first expanded in Fourier series in the azimuthal direction and the resulting equations for each harmonic are discretized using Gaussian quadrature method. The numerical solutions are obtained by solving for the eigenvalues and eigenvector and matching the boundary conditions. The bistatic scattering coefficients are obtained by re-introducing the azimuthal dependence. Rough surface effects are incorporated into the model by modifying the boundary conditions using the first-order solution based on the small perturbation method. The results show that co-polarized (HH and VV) returns are higher than cross-polarized (HV) returns in the forward and backward directions, and vise versa in the direction of $\phi = 90°$. It is also shown that cross-polarized scattering coefficients in the forward and backward directions depend strongly on the shape of scatterer. For spherical and spheroidal scatterers aligned in the vertical direction, the cross-polarized returns arise from multiple scattering and are lower than those of ellipsoidal scatterers.

The two layer model is then extended to multilayer case which is solved by implementing the effective boundary condition method. The method starts by first solving the bottom two layer problem. This is followed by applying the effective boundary conditions obtained to the calculation of next two layer case above. This process is repeated until the top layer is reached. The calculation of both first-year (FY) sea ice and multi-year (MY) sea ice cases using the multilayer model shows the significance of the air bubbles, compared to the brine inclusions, in the scattering characteristics. The MY case shows significantly higher scattering returns.

The emissivity of the sea ice layer is obtained by integrating the bistatic scattering coefficients over the upper hemisphere and relating the reflectivity to the emissivity. By assuming uniform physical temperature for sea ice, the brightness temperature is then computed. It is shown that the brightness temperature is sensitive to the dielectric constant of the scatterers which affects the absorption and scattering characteristics of the layer. The effect of the bottom rough interface on the brightness temperature is larger than that of the top rough interface when the waves can penetrate through the medium. For FY sea ice with mostly brine inclusions, the brightness temperature calculated is higher than that of the MY sea ice.

Thesis Supervisor: Professor J. A. Kong
Professor of Electrical Engineering
Thesis Supervisor: Dr. Robert T. Shin
Assistant Group Leader, Lincoln Laboratory

ACKNOWLEDGEMENTS

First and foremost, I would like to express my sincerest thanks to Professor Jin Au Kong for his valuable guidance, thoughtful advice and supervision of the thesis. I greatly treasure the learning experience I have had from his enlightening teaching of electromagnetic wave theory. Thank you very much.

I would also like to thank Dr. Robert T. Shin deeply for his supervision of the thesis, consistent encouragement and fruitful discussions. His precious insights and constructive comments guided me in every stage of my research. My sincere appreciation to Dr. Shin.

Many thanks to Dr. Eric Yang for his excellent ideas and helpful discussions in all of the projects we have worked on together. Projects such as EMSARS and GPS measurements not only broaden the scope but also enhance the enjoyment of my research.

My sincere gratitude to all the members in our group for their help, support and friendship. Thanks to Chih Chien Hsu for all his help and fruitful conversation. To Dr. M. Ali Tassoudji and Joel Johnson, I must say what a wonderful team for writing the solutions for the 6.014 text book. Thanks and gratitude I extend to you two for all your assistance, advice, and friendship. Dr. Murat Veysoglu has been the right person with whom to discuss interesting physical topics. My appreciation to him for all the enlightening discussions. Special thanks to Dr. Lars Bomholt for the great experiences that we have shared in exploring the computer world from Internet to Mosaic, from 3D graphics to programming bugs. Also thanks to Drs. William Au (fractals), Vitaly Feldman (X and Motif), John Oates, Jean-Claude Souyris, and Kung Hau Ding for their encouragement. I would also like to express my gratitude to Li-Fang Wang, Kevin Li, Pierre Coutu (RT for sea ice), Sean Shih, Yan Chang, Francesca Scire and all the present and former members of this group for making this group such a wonderful and nice group to work with. To Kit Wah Lai, the group's secretary, thanks for your help and patience.

My deep appreciation to Professors Tan Hon Siang (NTU, Singapore) and Chuah Hean Teik (UM, Malaysia) for their teaching, advice and confidence in me. To my friends here and in Malaysia, I thank them for their encouragement and friendship.

Last but not least, I would like to thank my family for their continuous support, understanding and love. To them, I dedicate this work.

Xie4 xie! Terima kasih! Thank you!

To My Parents

Contents

List of Figures

Chapter 1

Introduction

1.1 Background

It is known that global climate change depends on a large number of factors, among them sea ice. Since sea ice covers roughly 13% of the world ocean surface during some portion of the year and vigorously interacts with the atmosphere and the ocean, any change in the thermal and geological properties of sea ice will affect the global climate directly [1,2]. There is also a vast amount of water restored and frozen within the sea ice area. If only a small amount of the world's sea ice melts because of global warming due to the greenhouse effect, it is believed that the rise in the sea level would flood large areas of flat and highly populated land with water. Navigation through the sea ice area also requires a better understanding of ice drift and sea ice extent [1]. All of these factors make the study of the thermal and mechanical properties of sea ice very important.

Over the years, many detailed measurements of sea ice properties have been carried out by researchers. These include on-site measurement and airborne and

spaceborne remote sensing measurements. Spaceborne remote sensing is becoming more popular, because large areas can be covered without direct physical access to the hostile environment. For the remote sensing of sea ice, altimeters and optical sensors are used in conjunction with microwave sensors. The advantages of using microwave sensors over the other type of sensors are that microwaves can penetrate through clouds and do not depend on the illumination of the sun.

There are two basic types of microwave sensors, active and passive. Active sensors such as radars, synthetic aperture radars (SAR) and scatterometers, transmit a microwave signal to the target area, and then receive the radar return in magnitude and phase. The measured data is then fed into a computer for further processing. Passive sensors do not transmit any signal, but instead measure the thermal emission from the area sensed. For active remote sensing, there are two ways of carrying out the measurements: monostatic and bistatic. In monostatic measurements, the sensor transmits and receives microwave signals at the same location, whereas in bistatic measurements, the sensor transmits in one location and receives the return signal in a different location. References [3]-[13] report on active remote sensing measurement results, mostly in the form of backscattering coefficients versus the angle of incidence. Recently, there has been a great deal of interest in obtaining additional measurements for bistatic scattering coefficients. As is pointed out in [14], in order to reconstruct sea ice parameters such as the dielectric constant of ice from measurements, bistatic measurement are essential. Measurement results of sea ice from passive sensor systems are found in references [15-22]. Normally, these results are presented in the form of emissivity or brightness temperature versus the

looking angle or frequency. Emissivity is defined as $1 - r$, where r is the reflectivity of the medium, and brightness temperature is the product of the emissivity and the uniform physical temperature of the medium. Some efforts have been made to combine the measurement results of active and passive remote sensing [23,24]. This will provide more information about the sea ice properties, such as age (first year or multiyear), thickness, extent, fractional volume of brine inclusions, ice extent and surface roughness.

The need to develop an accurate theoretical model for the correct interpretation of remote sensing measurement results is apparent. In order to develop the model, a good and accurate understanding of sea ice physical properties and parameters is very important. From [25,26], it is known that a first year sea ice layer consists of parallel pure ice platelets with brine inclusions (salted water solution) embedded within them. The shape of the brine inclusions is almost ellipsoidal. Generally, the brine inclusions are more randomly distributed near the air-ice interface, and become more vertically distributed away from the air-ice interface. During the summer time, some of the ice melts and the brine is drained into the ocean. This leaves the inclusions filled with air. This process repeats year after year developing a type of ice called multiyear ice. Based on this understanding, a theoretical model of the sea ice layer can be constructed and studied. The important parameters which will affect the electromagnetic returns are the dielectric constants of the pure ice, ocean water and brine inclusions, the shape, size, fractional volume and distribution of the brine inclusions, frequency, thickness of sea ice layer, temperature, salinity and the roughness of air-ice and ice-water interfaces [27-31].

There are three approaches to characterize scattering and emission for active and passive measurements using the proposed physical model of sea ice. They are Wave Theory (WT), Radiative Transfer Theory (RT) and Modified Radiative Transfer Theory (MRT).

In the wave theory, Maxwell's equations are used to solve for the scattering properties of sea ice by introducing the scattering and absorption characteristics of the medium [32-42]. All the multiple scattering, interference and diffraction effects can be incorporated into the theory. However, due to its complicated formulation, certain approximations have to be made before numerical method can be applied to solve practical problems.

Radiative transfer theory, on the other hand, has been used widely in the microwave remote sensing community to calculate the scattering properties of different terrains such as vegetation and sea ice [43-55]. This theory is based on the energy transport equation and was used chiefly in the study of astrophysics [56]. However, for the past twenty years, its use has been expanded to other fields. The theory assumes no correlation between the fields and thus only considers the addition of intensities. The propagation of energy in the medium is characterised by the phase matrix and the extinction matrix [57]. The advantage of RT theory over wave theory is that it is simple and, more importantly, multiple scattering effects can be handled more easily. Furthermore, rough surface effects can be included by modifying the boundary conditions of the interfaces. For surfaces with large radius of curvature the Kirchhoff's approximation can be used [57]. In the case where the wavelength is small compared to the scale of roughness, a special case of Kirch-

hoff's's method called the Geometrical Optics approximation (GO) is used. If the surface RMS height is much smaller than the wavelength, the Small Perturbation Method (SPM) can be applied [57,58].

Modified Radiative Transfer Theory (MRT) can be derived from Maxwell's equations. It includes the coherent effects between the scatterers and the boundaries [57]. These coherent effects are used to explain the oscillatory behavior of the scattering coefficients as a function of frequency.

For this research, a theoretical model of sea ice based on the physical properties of sea ice is constructed. Radiative transfer theory is chosen because of its simplicity and ability to incorporate multiple scattering effects in the calculations. The extinction matrix and phase matrix of a medium with ellipsoidal scatterers is calculated. Rough surface effects is incorporated by modifying the boundary conditions, and the Small Perturbation Method (SPM) is used. The discrete ordinate-eigenanalysis method is applied to solve for the polarimetric bistatic scattering coefficients of the multilayer sea ice model. The emissivity (e) or brightness temperatures for such a configuration are also calculated. The effect of different sea ice parameters on the polarimetric bistatic scattering results and the brightness temperature for co and cross-polarization is explored. Some comparisons with the available passive measurement data is also carried out.

1.2 Sea Ice Physical Structure

Since sea water is not pure water but contains dissolved material such as inorganic salts and organic material, the freezing process of sea ice is very complicated [25]. Basically, when the surface of sea water approaches the freezing point, small platelets of pure ice parallel to the sea surface form in large numbers on top of the sea water. Because of the effects of wind and wave movement which tend to force the platelets toward a vertical position, the brine inclusions embedded within these platelets are randomly distributed [25,26]. As the freezing process proceeds, thicker sea ice layers are formed. Due to the vertical temperature gradient which favors ice growth in the vertical direction, the brine inclusions formed are more vertically distributed. The brine inclusions are generally ellipsoidal [30,31]. The amount of brine incorporated is also largely growth-rate dependent. In frazil ice, the brine inclusions are located between the crystal boundaries whereas in columnar ice, the inclusions are trapped within the ice crystals [25]. During the next warming season, draining channels are created when the brine inclusions expand. Due to the gravity force, some of the brine will flow through the channels towards the ocean leaving air inclusions where the brine inclusions were. In fact, brine drainage starts immediately after ice formation, but at a very slow rate during the growth season. As a result, multiyear sea ice layer normally contains a combination of brine and air inclusions.

1.3 Modeling of Sea Ice

Generally, the size of sea ice extent varies strongly with the season. Reports on the sea ice coverage over the past 18 years [68] show that in the spring of each polar region, sea ice extends to the mid-latitudes, and in late summer and early fall, the size decreases to the region of the Artic Basin and the Antartic margins. Even within a short period of time, the change in thickness of ice layer, its physical temperature, and its brine distribution vary. This makes the work of getting a correct model of sea ice pretty complicated. However, with a better understanding of the real sea ice physical structure and the freezing process involved, a feasible model can be obtained. For both first year (FY) and multiyear (MY) sea ice, a multilayer structure is constructed. Each layer consists of a pure ice background with a certain fractional volume of brine inclusions. The shape, size and distribution of the brine inclusions can be chosen to fit in the real physical dimensions. The difference between the two types of ice is that for multiyear ice, there are two kinds of scatterers, brine and air ellipsoids, whereas first year ice contains only brine ellipsoids. The configurations for both the first year and multiyear sea ice model are shown in Figures 1.1 and 1.2.

1.4 Description of the Thesis

This thesis consists of six chapters. The first chapter gives an introduction to microwave remote sensing, a short review of the methods available to predict theoretical returns from geophysical terrain and a description of ice formation process.

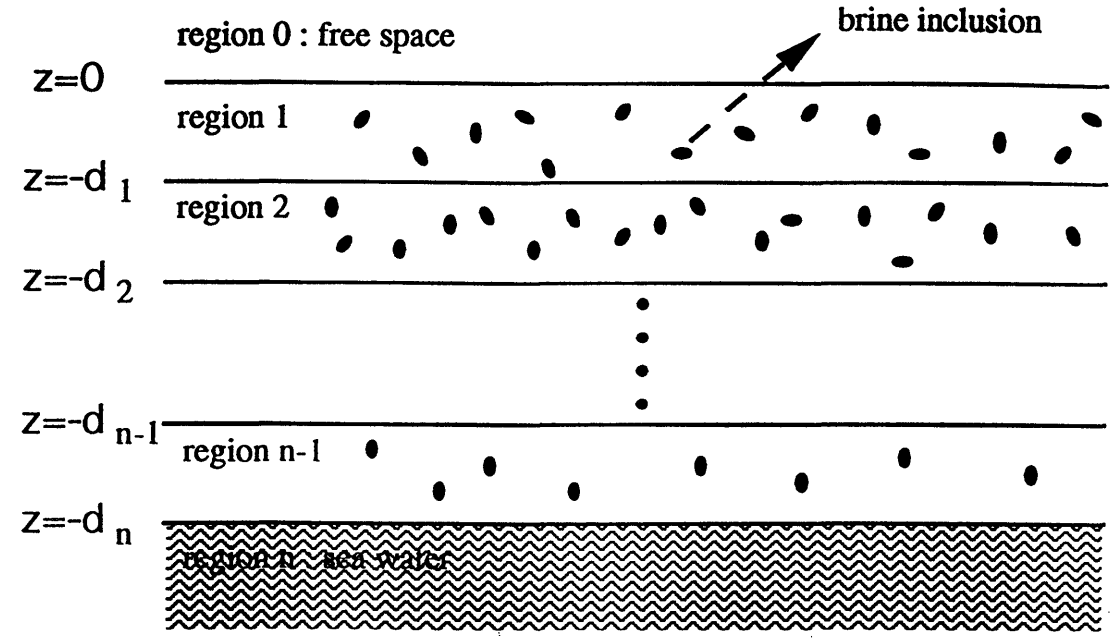

Figure 1.1: Configuration for first year sea ice model

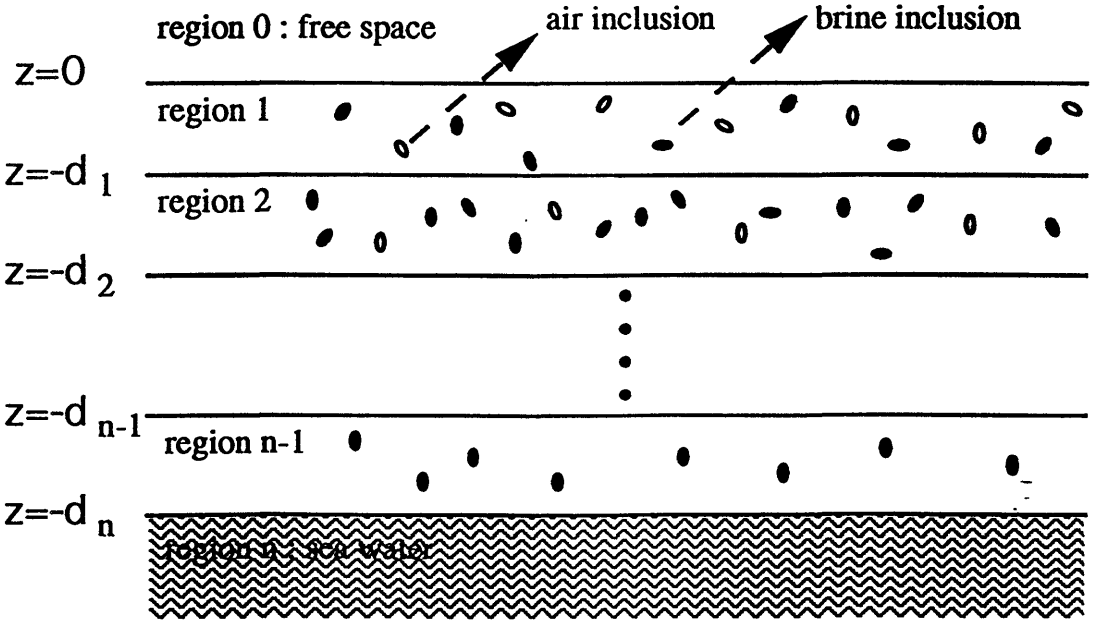

Figure 1.2: Configuration for multiyear sea ice model

Configurations of the sea ice model constructed are also included.

The Stokes vector, bistatic scattering coefficients and other parameters are defined in Chapter 2. A description of radiative transfer theory is presented. This is followed by the definition of the extinction and phase matrices. The boundary conditions for the sea ice model are then discussed. A complete numerical procedure for solving the radiative transfer equations for a two layer medium with planar interfaces is also included. Theoretical results are plotted and the effects of various physical parameters on the calculated bistatic scattering coefficients are illustrated.

The approach is extended to a two layer medium with rough interfaces in Chapter 3. New boundary conditions have to be derived to incorporate the rough interface effects and these are elaborated.

For a multilayer medium, the fully polarimetric numerical calculations become more complicated. Thus, the layer by layer approach, which uses the concept of an effective reflection matrix, is presented in Chapter 4.

Chapter 5 starts with a brief introduction to passive remote sensing. The numerical method involved is elaborated. Theoretical results are obtained for all the configurations of sea ice mentioned above. The trends are studied and compared with the available measurement data.

Finally, summary and suggestions for future work are presented in Chapter 6.

Chapter 2

Theoretical Model for a Two Layer Random Medium with Planar Interfaces

2.1 Configuration and Definition

Let us first define $(\overline{E}_i)$ as the incident field, and we are interested in the scattered field $(\overline{E}_s)$ when the electromagnetic wave enters a layered medium. This scattered field can be related to the incident field by a scattering matrix $(\overline{\overline{F}})$ as in the following expression:

$$\begin{bmatrix} E_{vs} \\ E_{hs} \end{bmatrix} = \frac{e^{ikr}}{r} \begin{bmatrix} f_{vv} & f_{vh} \\ f_{hv} & f_{hh} \end{bmatrix} \cdot \begin{bmatrix} E_{vi} \\ E_{hi} \end{bmatrix} \tag{2.1}$$

where the incident field $(\overline{E}_i)$ is decomposed into two polarizations, the vertically and horizontally polarized electric fields (E_{vi}, E_{hi}). The scattered field is also decomposed into the same two polarizations. In the above equation, $k = \omega\sqrt{\mu\epsilon}$ is the wave number, r is the distance between the layered medium and the receiver, and $f_{\alpha\beta}$ is an element of the scattering matrix.

The Stokes vector can also be used to represent the incident and scattered specific intensities. It has four parameters, I_v, I_h, U and V, where I_v is the vertically polarized specific intensity, I_h is the horizontally polarized specific intensity, and U and V represent the correlation between two polarizations. The incident and scattered specific intensities are defined as [57]

$$\overline{I}_i = \begin{bmatrix} I_{vi} \\ I_{hi} \\ U_i \\ V_i \end{bmatrix} = \frac{1}{\eta} \begin{bmatrix} E_{vi}E_{vi}^* \\ E_{hi}E_{hi}^* \\ 2\,\mathrm{Re}\,(E_{vi}E_{hi}^*) \\ 2\,\mathrm{Im}\,(E_{vi}E_{hi}^*) \end{bmatrix} \tag{2.2}$$

and

$$\overline{I}_s = \begin{bmatrix} I_{vs} \\ I_{hs} \\ U_s \\ V_s \end{bmatrix} = \frac{1}{\eta} \lim_{\substack{r\to\infty \\ A\to\infty}} \frac{r^2}{A\cos\theta_s} \begin{bmatrix} \langle E_{vs}E_{vs}^* \rangle \\ \langle E_{hs}E_{hs}^* \rangle \\ 2\,\mathrm{Re}\,\langle E_{vs}E_{hs}^* \rangle \\ 2\,\mathrm{Im}\,\langle E_{vs}E_{hs}^* \rangle \end{bmatrix} \tag{2.3}$$

where η is the characteristic impedance, A is the illuminated area, θ_s is the scattered angle and $\langle\rangle$ denotes ensemble average.

The unit of specific intensity is watts $\mathrm{m}^{-2}\mathrm{Sr}^{-1}\mathrm{Hz}^{-1}$. The radiation field is homogeneous if the intensity is the same at all points and is considered isotropic if the intensity in all directions is the same. It is also invariant along the ray path in free space [57].

The scattering effects of geophysical terrain can be studied through the Mueller matrix ($\overline{\overline{M}}$), which relates the incident and scattered Stokes vectors. The relationship is shown below:

$$\overline{I}_s(\theta, \phi + \pi) = \overline{\overline{M}} \cdot \overline{I}_i(\pi - \theta, \phi) = \begin{bmatrix} M_{11} & M_{12} & M_{13} & M_{14} \\ M_{21} & M_{22} & M_{23} & M_{24} \\ M_{31} & M_{32} & M_{33} & M_{34} \\ M_{41} & M_{42} & M_{43} & M_{44} \end{bmatrix} \cdot \overline{I}_i(\pi - \theta, \phi) \quad (2.4)$$

where

$$M_{11} = \lim_{A \to \infty} \frac{1}{A \cos\theta} \langle |f_{vv}|^2 \rangle \quad (2.5)$$

$$M_{12} = \lim_{A \to \infty} \frac{1}{A \cos\theta} \langle |f_{vh}|^2 \rangle \quad (2.6)$$

$$M_{13} = \lim_{A \to \infty} \frac{1}{A \cos\theta} \mathrm{Re} \langle f_{vv} f_{vh}^* \rangle \quad (2.7)$$

$$M_{14} = -\lim_{A \to \infty} \frac{1}{A \cos\theta} \mathrm{Im} \langle f_{vv} f_{vh}^* \rangle \quad (2.8)$$

$$M_{21} = \lim_{A \to \infty} \frac{1}{A \cos\theta} \langle |f_{hv}|^2 \rangle \quad (2.9)$$

$$M_{22} = \lim_{A \to \infty} \frac{1}{A \cos\theta} \langle |f_{hh}|^2 \rangle \quad (2.10)$$

$$M_{23} = \lim_{A \to \infty} \frac{1}{A \cos\theta} \mathrm{Re} \langle f_{hv} f_{hh}^* \rangle \quad (2.11)$$

$$M_{24} = -\lim_{A \to \infty} \frac{1}{A \cos\theta} \mathrm{Im} \langle f_{hv} f_{hh}^* \rangle \quad (2.12)$$

$$M_{31} = \lim_{A \to \infty} \frac{1}{A \cos\theta} 2 \mathrm{Re} \langle f_{vv} f_{hv}^* \rangle \quad (2.13)$$

$$M_{32} = \lim_{A \to \infty} \frac{1}{A \cos\theta} 2 \mathrm{Re} \langle f_{vh} f_{hh}^* \rangle \quad (2.14)$$

$$M_{33} = \lim_{A \to \infty} \frac{1}{A \cos\theta} \mathrm{Re} \langle f_{vv} f_{hh}^* + f_{vh} f_{hv}^* \rangle \quad (2.15)$$

$$M_{34} = -\lim_{A \to \infty} \frac{1}{A \cos\theta} \mathrm{Im} \langle f_{vv} f_{hh}^* - f_{vh} f_{hv}^* \rangle \quad (2.16)$$

$$M_{41} = \lim_{A\to\infty} \frac{1}{A\cos\theta} 2\,\mathrm{Im}\,\langle f_{vv} f_{hv}^* \rangle \tag{2.17}$$

$$M_{42} = \lim_{A\to\infty} \frac{1}{A\cos\theta} 2\,\mathrm{Im}\,\langle f_{vh} f_{hh}^* \rangle \tag{2.18}$$

$$M_{43} = \lim_{A\to\infty} \frac{1}{A\cos\theta} \mathrm{Im}\,\langle f_{vv} f_{hh}^* + f_{vh} f_{hv}^* \rangle \tag{2.19}$$

$$M_{44} = \lim_{A\to\infty} \frac{1}{A\cos\theta} \mathrm{Re}\,\langle f_{vv} f_{hh}^* - f_{vh} f_{hv}^* \rangle \tag{2.20}$$

where A is the illuminated area, r is the observation distance from the receiver, θ is the scattered and incident angles and $f_{\alpha\beta}$ are the elements of the scattering matrix. It can also be seen that the elements of Mueller matrix are closely related to the elements of scattering matrix.

The bistatic scattering coefficients $\gamma_{\beta\alpha}(\theta_{os}, \phi_{os}; \theta_{oi}, \phi_{oi})$ are defined as

$$\gamma_{\beta\alpha}(\theta_{os}, \phi_{os}; \theta_{oi}, \phi_{oi}) = 4\pi \frac{\cos\theta_{os}\ I_{o\beta s}(\theta_{os}, \phi_{os})}{\cos\theta_{oi}\ I_{o\alpha i}} \tag{2.21}$$

where $\alpha, \beta = v$ (vertical polarization) or h (horizontal polarization), $I_{o\beta s}$ is the scattered power of polarization β, and $I_{o\alpha i}$ is the incident power of polarization α. In the backscattering direction, $\theta_{os} = \theta_{oi}$ and $\phi_{os} = \pi - \phi_{oi}$, and thus the backscattering cross sections per unit area are defined to be

$$\sigma_{\beta\alpha}(\theta_{oi}) = \cos\theta_{oi}\ \gamma_{\beta\alpha}(\theta_{oi}, \pi + \phi_{oi}; \theta_{oi}, \phi_{oi}) \tag{2.22}$$

For passive remote sensing, the emissivity is given by [57]

$$e_\alpha(\theta_{oi}) = 1 - \Sigma_\beta \frac{1}{4\pi} \int_0^{\frac{\pi}{2}} d\theta_{os} \sin\theta_{os} \int_0^{2\pi} d\phi_{os}\ \gamma_{\beta\alpha}(\theta_{os}, \phi_{os}; \theta_{oi}, \phi_{oi}) \tag{2.23}$$

where $\gamma_{\beta\alpha}(\theta_{os}, \phi_{os}; \theta_{oi}, \phi_{oi})$ is the bistatic scattering coefficient. By finding the bistatic scattering coefficients for different scattered angles and polarizations and then summing them up for a particular incident polarized wave (α) at an incident angle (θ_{oi}), the emissivity of the medium can be calculated.

The definition of the absorptivity of a body is the ratio of the total thermal energy absorbed to the total incident thermal energy [57]. For a black body, the absorptivity a is equal to 1, which means the emissivity is also equal to 1. For most of the real materials, the emissivity is less than unity and depends on the angle of observation and the polarization. Let $I_\alpha(\theta, \phi)$ be the specific intensity received by a radiometer from the observed object where α is the polarization and (θ, ϕ) denotes the angular dependence. A new parameter called the brightness temperature $T_{\alpha B}(\theta, \phi)$ can be defined as follows:

$$T_{\alpha B}(\theta, \phi) = I_\alpha(\theta, \phi)\frac{\lambda^2}{K} \tag{2.24}$$

where λ is the wavelength and K is Boltzmann's constant. The brightness temperature can be further related to the real physical temperature T by the following expression:

$$T_{\alpha B}(\theta, \phi) = e_\alpha(\theta_{oi})T \tag{2.25}$$

where again $e_\alpha(\theta_{oi})$ is the emissivity.

The physical configuration of the problem is shown in Figure 2.1. This two-layer structure with flat interfaces is the basic structure of the problem. Later,

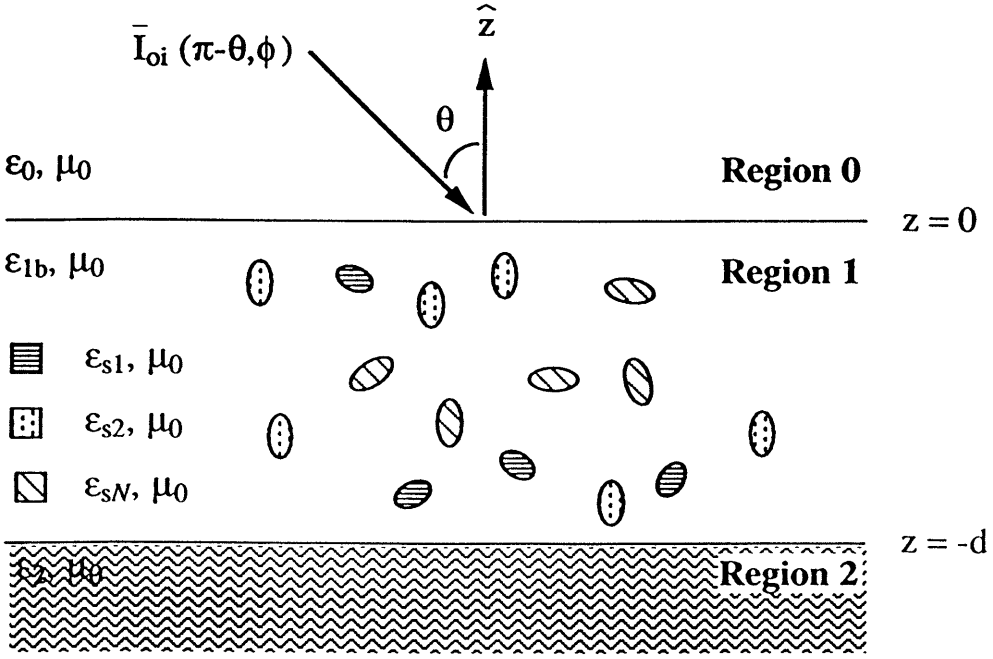

Figure 2.1: Configuration for two layer medium with planar interfaces with different types of scatterers.

rough surfaces can be added in and multilayer structures can be constructed based on this simple configuration. Region 0 is the free space halfspace with ϵ_0 and μ_0. Region 1 is a dielectric slab (ϵ_{1b}, μ_0) with N types of discrete scatterers embedded in it. These scatterers can be either vertically distributed or randomly distributed. The shape, size and permittivities $(\epsilon_{s1}, \epsilon_{s2}, ..., \epsilon_{sN})$ of the scatterers can be chosen to fit the realistic sea ice configurations. The thickness of the slab is d. Region 2 is a homogeneous dielectric halfspace characterized by ϵ_2 and μ_0. The interfaces between regions $(z = 0, z = -d)$ are flat. The incident specific intensity $\bar{I}_{oi}(\pi - \theta, \phi)$ is also shown.

In Figure 2.2, the polarization vectors for upward (θ_1) and downward (θ_2) propagation are shown. The angle (θ) is measured from the $\hat{z}$ axis and the angle

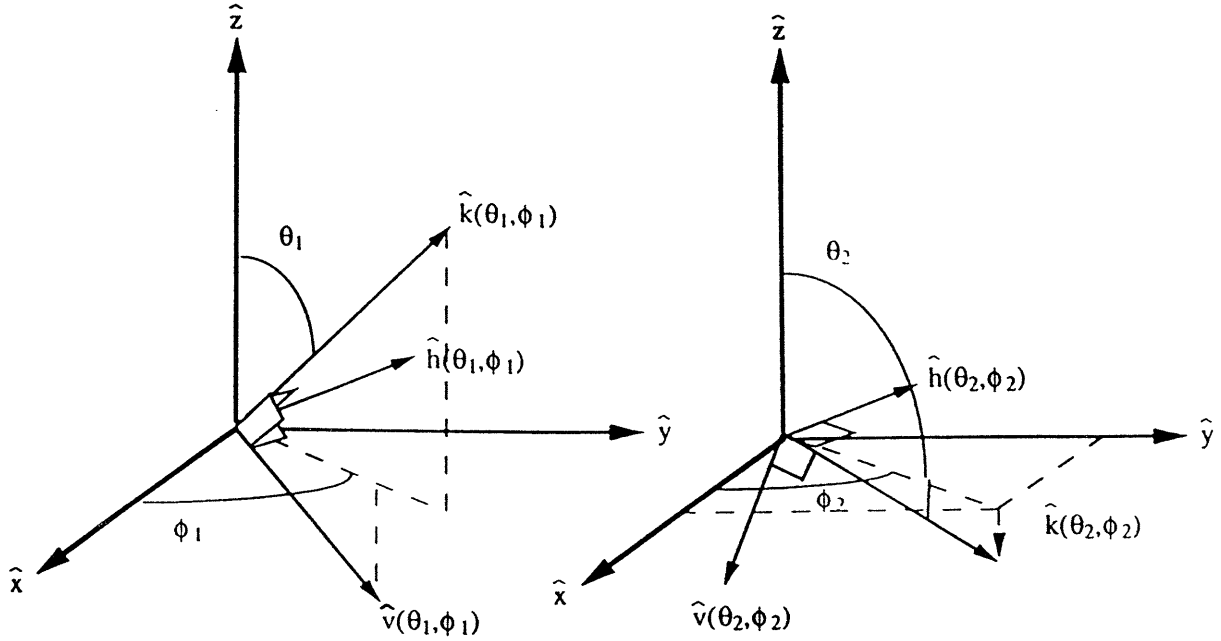

Figure 2.2: The polarization vectors for upward (θ_1) and downward (θ_2) propagation.

(ϕ) extends from the $\hat{x}$ axis. The $\hat{v}$, $\hat{h}$ and $\hat{k}$ vectors are orthogonal to each other and can be expressed in the cartesian coordinates as follows:

$$\hat{k} = \sin\theta\cos\phi\ \hat{x} + \sin\theta\sin\phi\ \hat{y} + \cos\theta\ \hat{z} \tag{2.26}$$

$$\hat{v} = \cos\theta\cos\phi\ \hat{x} + \cos\theta\sin\phi\ \hat{y} - \sin\theta\ \hat{z} \tag{2.27}$$

$$\hat{h} = -\sin\phi\ \hat{x} + \cos\phi\ \hat{y} \tag{2.28}$$

2.2 Radiative Transfer Theory

The radiative transfer equation is based on the energy transport equation, which deals with the propagation of intensities in the medium. It has been widely used in the microwave remote sensing community to model the returns from geophysical media [43-55]. In general, there are two scattering effects which affect the measured brightness temperature and radar scattering coefficients: volume scattering and rough surface scattering. Volume scattering is due to the inhomogeneities in the medium. There are two theoretical models which deal with volume scattering: (1) In discrete scatterer model, the medium is treated as a homogeneous dielectric medium embedded with scatterers of different sizes, shapes, orientations and permittivities. Among the different shapes of the scatterers, spheres, spheroids, ellipsoids, discs and cylinders are widely used. (2) In random medium model, the permittivity of the medium consists of two parts, a mean part and a fluctuating part. The fluctuating part is characterized by its variance and spatial correlation. In this thesis, the first model is chosen because the physical geometry of the scatterers can be better related to the numerical solutions in this model.

The Stokes vector mentioned in Section 2.1 is used in the radiative transfer equation. The Mueller matrix can be obtained from the solution of the radiative transfer equation. The radiative transfer equation in region 1 is shown below:

$$\cos\theta \frac{d}{dz}\overline{I}(\theta,\phi,z) = -\overline{\overline{\kappa}}_e(\theta,\phi)\cdot\overline{I}(\theta,\phi,z) + \int_{4\pi} d\Omega' \quad \overline{\overline{P}}(\theta,\phi;\theta',\phi')\cdot\overline{I}(\theta',\phi',z) \quad (2.29)$$

where $\overline{\overline{P}}(\theta,\phi;\theta',\phi')$ is a 4×4 phase matrix, which relates scattered intensities (θ,ϕ)

to the incident intensities (θ', ϕ') and $\overline{\overline{\kappa}}_e$ is the extinction matrix which includes the absorption loss in the background medium and scatterers as well as scattering loss due to the scatterers.

2.3 Phase and Extinction Matrix

2.3.1 Single Species of Scatterer

As defined in Section 2.1, the scattered field $(\overline{E}_s)$ is related to the incident field $(\overline{E}_i)$ by the scattering function matrix $\overline{\overline{F}}(\theta_s, \phi_s; \theta_i, \phi_i)$. The relation is shown below:

$$\overline{E}_s = \frac{e^{ikr}}{r}\overline{\overline{F}}(\theta_s, \phi_s; \theta_i, \phi_i) \cdot \hat{e}_i E_0 \tag{2.30}$$

Both E_s and E_i can be decomposed into vertically and horizontally polarized components; the relation is:

$$\begin{bmatrix} E_{vs} \\ E_{hs} \end{bmatrix} = \frac{e^{ikr}}{r} \begin{bmatrix} f_{vv}(\theta_s, \phi_s; \theta_i, \phi_i) & f_{vh}(\theta_s, \phi_s; \theta_i, \phi_i) \\ f_{hv}(\theta_s, \phi_s; \theta_i, \phi_i) & f_{hh}(\theta_s, \phi_s; \theta_i, \phi_i) \end{bmatrix} \cdot \begin{bmatrix} E_{vi} \\ E_{hi} \end{bmatrix} \tag{2.31}$$

with

$$f_{ab}(\theta_s, \phi_s; \theta_i, \phi_i) = \hat{a}_s \cdot \overline{\overline{F}}(\theta_s, \phi_s; \theta_i, \phi_i) \cdot \hat{b}_i \tag{2.32}$$

and $a, b = v, h$.

The incident Stokes vector and the scattered Stokes vector can be related by

the following expression:

$$\overline{I}_s = \frac{1}{r^2}\overline{\overline{L}}(\theta_s, \phi_s; \theta_i, \phi_i) \cdot \overline{I}_i \tag{2.33}$$

where $\overline{\overline{L}}$ is the Stokes matrix.

By using

$$I_v = \frac{|E_v|^2}{\eta} \tag{2.34}$$

$$I_h = \frac{|E_h|^2}{\eta} \tag{2.35}$$

$$U = \frac{2}{\eta}\mathrm{Re}(\mathrm{E_v E_h^*}) \tag{2.36}$$

$$V = \frac{2}{\eta}\mathrm{Im}(\mathrm{E_v E_h^*}) \tag{2.37}$$

and the scattering function matrix $\overline{\overline{F}}(\theta_s, \phi_s; \theta_i, \phi_i)$, the Stokes matrix $\overline{\overline{L}}(\theta_s, \phi_s; \theta_i, \phi_i)$ can be derived and has the final form of:

$$\overline{\overline{L}}(\theta_s, \phi_s; \theta_i, \phi_i) = \begin{bmatrix} |f_{vv}|^2 & |f_{vh}|^2 & \mathrm{Re}\,(f_{vv} f_{vh}^*) & -\mathrm{Im}\,(f_{vv} f_{vh}^*) \\ |f_{hv}|^2 & |f_{hh}|^2 & \mathrm{Re}\,(f_{hv} f_{hh}^*) & -\mathrm{Im}\,(f_{hv} f_{hh}^*) \\ 2\ \mathrm{Re}\,(f_{vv} f_{hv}^*) & 2\ \mathrm{Re}\,(f_{vh} f_{hh}^*) & \mathrm{Re}\,(f_{vv} f_{hh}^* + f_{vh} f_{hv}^*) & -\mathrm{Im}\,(f_{vv} f_{hh}^* - f_{vh} f_{hv}^*) \\ 2\ \mathrm{Im}\,(f_{vv} f_{hv}^*) & 2\ \mathrm{Im}\,(f_{vh} f_{hh}^*) & \mathrm{Im}\,(f_{vv} f_{hh}^* + f_{vh} f_{hv}^*) & \mathrm{Re}\,(f_{vv} f_{hh}^* - f_{vh} f_{hv}^*) \end{bmatrix} \tag{2.38}$$

The phase matrix $\overline{\overline{P}}(\theta_s, \phi_s; \theta_i, \phi_i)$ is obtained by incoherent averaging of the Stokes matrix over the type, size, shape and spatial orientation of the scatterers.

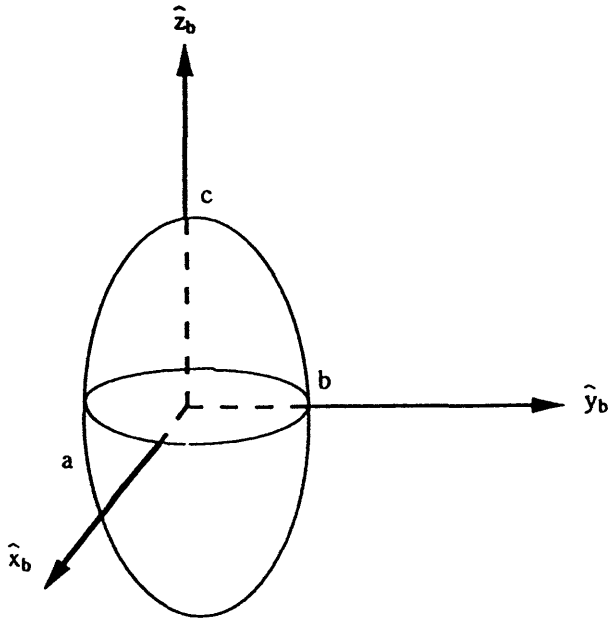

Figure 2.3: Ellipsoidal scatterer in its primary coordinate system $\hat{x}_b$, $\hat{y}_b$ and $\hat{z}_b$.

The phase matrix for a mixture of one species of ellipsoids (Figure 2.3) is given by:

$$\begin{aligned}\overline{\overline{P}}(\theta_s,\phi_s;\theta_i,\phi_i) &= n_o \int da \int db \int dc \int d\alpha \int d\beta \int d\gamma \\ &\quad \cdot \mathrm{p}(a,b,c,\alpha,\beta,\gamma) \cdot \overline{\overline{L}}(\theta_s,\phi_s;\theta_i,\phi_i) \qquad (2.39)\end{aligned}$$

where n_o is the number of scatterers per unit volume; a, b, c are the length of the ellipsoid semi-major axis; α,β,γ are the Eulerian angles which describe the orientation of the ellipsoid and $\mathrm{p}(a,b,c,\alpha,\beta,\gamma)$ is the joint probability density function for the quantities $a,b,c,\alpha,\beta,\gamma$.

Phase matrices for single species of ellipsoidal scatterers with vertical and random orientation distributions are given in the Appendix B.2.

The extinction matrix in the radiative transfer equation actually represents the attenuation rate in the coherent wave propagation [46,57]. It is given by:

$$\bar{\bar{\kappa}}_{et}(\theta,\phi) = \begin{bmatrix} -2\,\mathrm{Re}(M_{vv}) & 0 \\ 0 & -2\,\mathrm{Re}(M_{hh}) \\ -2\,\mathrm{Re}(M_{hv}) & -2\,\mathrm{Re}(M_{vh}) \\ 2\,\mathrm{Im}(M_{hv}) & -2\,\mathrm{Im}(M_{vh}) \end{bmatrix} \begin{bmatrix} -\mathrm{Re}(M_{vh}) & -\mathrm{Im}(M_{vh}) \\ -\mathrm{Re}(M_{hv}) & \mathrm{Im}(M_{hv}) \\ -\mathrm{Re}(M_{vv}+M_{hh}) & \mathrm{Im}(M_{vv}-M_{hh}) \\ -\mathrm{Im}(M_{vv}-M_{hh}) & -\mathrm{Re}(M_{vv}+M_{hh}) \end{bmatrix} \tag{2.40}$$

where

$$M_{pq} = \frac{i2\pi n_o}{k}\langle f_{pq}(\theta,\phi;\theta,\phi)\rangle \qquad p,q = v,h \tag{2.41}$$

and $\langle\rangle$ is the ensemble average over the size and orientation distribution of the scatterers. In order to use this definition, the real and imaginary part of the scattering functions must be calculated to a sufficient accuracy [45].

The total extinction matrix is actually a summation of the scattering loss due to the scatterers and also the absorption losses due to the scatterers and the background medium [46].

$$\bar{\bar{\kappa}}_e(\theta,\phi) = \bar{\bar{\kappa}}_{ab} + \bar{\bar{\kappa}}_{as}(\theta,\phi) + \bar{\bar{\kappa}}_{ss}(\theta,\phi) \tag{2.42}$$

$\bar{\bar{\kappa}}_{ab}$ is given by:

$$\bar{\bar{\kappa}}_{ab} = 2\,\mathrm{Im}(k_b)(1-f_v)\cdot\bar{\bar{I}} \tag{2.43}$$

where $\overline{\overline{I}}$ is the identity matrix, k_b is the complex wave number in the background medium and f_v is the fractional volume occupied by the scatterers.

The approach to obtain the scattering loss matrix is straightforward. By summing up all the components scattered from direction (θ_i, ϕ_i) into other directions, the scattering loss matrix can be readily calculated from the phase matrix as follows:

$$\overline{\overline{\kappa}}_{ss}(\theta_i,\phi_i) = \begin{bmatrix} \kappa_{sv}(\theta_i,\phi_i) & 0 & 0 & 0 \\ 0 & \kappa_{sh}(\theta_i,\phi_i) & 0 & 0 \\ 0 & 0 & \frac{\kappa_{sv}(\theta_i,\phi_i)+\kappa_{sh}(\theta_i,\phi_i)}{2} & 0 \\ 0 & 0 & 0 & \frac{\kappa_{sv}(\theta_i,\phi_i)+\kappa_{sh}(\theta_i,\phi_i)}{2} \end{bmatrix} \quad (2.44)$$

where:

$$\kappa_{sv}(\theta_i,\phi_i) = \int_0^{2\pi} d\phi_s \int_0^{\pi} \sin\theta_s d\theta_s [p_{11}(\theta_s,\phi_s;\theta_i,\phi_i) + p_{21}(\theta_s,\phi_s;\theta_i,\phi_i)] \quad (2.45)$$

$$\kappa_{sh}(\theta_i,\phi_i) = \int_0^{2\pi} d\phi_s \int_0^{\pi} \sin\theta_s d\theta_s [p_{12}(\theta_s,\phi_s;\theta_i,\phi_i) + p_{22}(\theta_s,\phi_s;\theta_i,\phi_i)] \quad (2.46)$$

A more detailed description of the extinction matrix for vertically and randomly distributed ellipsoidal scatterers can be found in the Appendix B.3.

2.3.2 Multiple Species of Scatterer

The calculation of extinction matrix can be easily extended to a layer containing N different types of scatterers. Each type of scatterer will have its own size, shape and orientation. This combination is very useful in the modelling of realistic sea ice structures, especially for multilayer sea ice. The phase matrix for multiple species of scatterers can be computed by averaging the phase matrix for a single species of

the scatterers incoherently. The expression is shown below:

$$\overline{\overline{P}}_{total}(\theta,\phi;\theta',\phi') = \sum_{i=1}^{N} \overline{\overline{P}}_i(\theta,\phi;\theta',\phi') \tag{2.47}$$

where $\overline{\overline{P}}_i$ is the phase matrix for scatterers of type i.

The same practice can be applied to the calculation of the extinction matrix, which gives

$$\overline{\overline{\kappa}}_{as_{total}}(\theta,\phi) = \sum_{i=1}^{N} \overline{\overline{\kappa}}_{as_i}(\theta,\phi) \tag{2.48}$$

$$\overline{\overline{\kappa}}_{ss_{total}}(\theta,\phi) = \sum_{i=1}^{N} \overline{\overline{\kappa}}_{ss_i}(\theta,\phi) \tag{2.49}$$

$$\overline{\overline{\kappa}}_{ab_{total}} = 2\,\mathrm{Im}\,(k_b)(1-\sum_{i=1}^{N} f_{v_i}) \cdot \overline{\overline{I}} \tag{2.50}$$

2.4 Boundary Conditions

Boundary conditions at interfaces $z = 0$ and $z = -d$ are needed to completely solve the radiative transfer equation. Based on the principle of conservation of energy, the boundary conditions for planar surfaces are shown below [46]:

Let the incident source in region 0 be

$$\overline{I}_{0i}(\theta_0,\phi_0) = \overline{I}_{0i}\delta(\cos\theta_0 - \cos\theta_{0i})\delta(\phi_0 - \phi_{0i}) \tag{2.51}$$

then the boundary conditions are:

Interface 1 ($z = 0$)*:*

$$\bar{I}(\pi - \theta, \phi, z = 0) = \bar{\bar{T}}_{01}(\theta_0) \cdot \bar{I}_{0i}(\pi - \theta_0, \phi_0) + \bar{\bar{R}}_{10}(\theta) \cdot \bar{I}(\theta, \phi, z = 0) \qquad (2.52)$$

Interface 2 ($z = -d$)*:*

$$\bar{I}(\theta, \phi, z = -d) = \bar{\bar{R}}_{12}(\theta) \cdot \bar{I}(\pi - \theta, \phi, z = -d) \qquad (2.53)$$

where $\bar{\bar{R}}_{10}(\theta)$ is the reflection matrix which relates the upward going intensities in region 1 to the reflected downward going intensities in the same region at interface 1 ($z = 0$), $\bar{\bar{R}}_{12}(\theta)$ is the reflection matrix which relates the downward going intensities in region 1 to the reflected upward going intensities in the same region at interface 2 ($z = -d$). Similarly, $\bar{\bar{T}}_{01}(\theta)$ is the transmission matrix which relates the downward going intensities in region 0 to the transmitted downward going intensities in region 1 at interface 1 ($z = 0$).

The solution of radiative transfer equation inside region 1 is then matched with the following boundary condition to obtain the scattered Stokes vector:

$$\bar{I}_{0s}(\theta_0, \phi_0, z = 0) = \bar{\bar{R}}_{01}(\theta_0) \cdot \bar{I}_{0i}(\pi - \theta_0, \phi_0) + \bar{\bar{T}}_{10}(\theta) \cdot \bar{I}(\theta, \phi, z = 0) \qquad (2.54)$$

where ϕ and ϕ_0 are the same, and Snell's law can be used to find the relation between θ and θ_0.

2.5 Numerical Solution

The radiative transfer equation is again shown below:

$$\cos\theta \frac{d}{dz}\bar{I}(\theta,\phi,z) = -\bar{\bar{\kappa}}_e(\theta,\phi)\cdot\bar{I}(\theta,\phi,z) + \int_{4\pi} d\Omega' \quad \bar{\bar{P}}(\theta,\phi;\theta',\phi')\cdot\bar{I}(\theta',\phi',z) \quad (2.55)$$

There are two ways of solving this equation, the iterative and numerical methods. Generally, if the scattering is small compared to the absorption (small albedo), a closed form solution can be obtained through an iterative approach. This is carried out by transforming the radiative transfer equation and the boundary conditions into an integral equation form and then solving for the first and second order solutions. However, when the albedo is not small, a numerical method is preferred [45]. The illustration of this method will be presented in the following parts of this section.

2.5.1 Fouries Series Expansion

First of all, the radiative transfer equation can be expanded into Fourier series in the azimuthal direction (ϕ). Let

$$\begin{aligned}\bar{\bar{P}}(\theta,\phi;\theta',\phi') &= \sum_{m=0}^{\infty}\frac{1}{(1+\delta_{m0})\pi} \\ &\quad \left[\bar{\bar{P}}^{mc}(\theta,\theta')\cos m(\phi-\phi') + \bar{\bar{P}}^{ms}(\theta,\theta')\sin m(\phi-\phi')\right] \quad (2.56)\\ \bar{I}(\theta,\phi,z) &= \sum_{m=0}^{\infty}\left[\bar{I}^{mc}(\theta,z)\cos m(\phi-\phi') + \bar{I}^{ms}(\theta,z)\sin m(\phi-\phi')\right] (2.57)\end{aligned}$$

and for the incident Stokes vector:

$$\begin{aligned}\bar{I}_{0i}(\pi-\theta_0,\phi_0) &= \bar{I}_{0i}\,\delta(\cos\theta_0-\cos\theta_{0i})\,\delta(\phi_0-\phi_{0i}) \\ &= \bar{I}_{0i}\,\delta(\cos\theta_0-\cos\theta_{0i})\sum_{m=0}^{\infty}\frac{1}{(1+\delta_{m0})\pi}\cos m(\phi_0-\phi_{0i}) \quad (2.58)\end{aligned}$$

where $\bar{\bar{P}}^{mc}$ and $\bar{\bar{P}}^{ms}$ are respectively $m-th$ cosine and sine term of Fourier expansion of the phase matrix in the azimuthal direction, and δ_{ij},the Kronecker delta function, is defined as:

$$\delta_{ij}=\begin{cases}1 & \text{if } i=j\\ 0 & \text{if } i\neq j\end{cases} \quad (2.59)$$

Substituting (2.56) and (2.57) into (2.55), then carrying out the integration with respect to ϕ, and finally collecting terms with the same sine or cosine dependence, we obtain the following set of equations:

$$\begin{aligned}\cos\theta\frac{d}{dz}\bar{I}^{mc}(\theta,z) &= -\bar{\bar{\kappa}}_e(\theta)\cdot\bar{I}^{mc}(\theta,z)+\int_0^{\pi}d\theta'\sin\theta' \\ &\quad\left[\bar{\bar{P}}^{mc}(\theta,\theta')\cdot\bar{I}^{mc}(\theta',z)-\bar{\bar{P}}^{ms}(\theta,\theta')\cdot\bar{I}^{ms}(\theta',z)\right] \quad (2.60)\\ \cos\theta\frac{d}{dz}\bar{I}^{ms}(\theta,z) &= -\bar{\bar{\kappa}}_e(\theta)\cdot\bar{I}^{ms}(\theta,z)+\int_0^{\pi}d\theta'\sin\theta' \\ &\quad\left[\bar{\bar{P}}^{ms}(\theta,\theta')\cdot\bar{I}^{mc}(\theta',z)+\bar{\bar{P}}^{mc}(\theta,\theta')\cdot\bar{I}^{ms}(\theta',z)\right] \quad (2.61)\end{aligned}$$

These equations do not have a ϕ dependence, which will save a large amount of computation time.

For azimuthally isotropic media, it is shown that the phase matrices $\bar{\bar{P}}^{mc}(\theta,\theta')$

and $\overline{\overline{P}}^{ms}(\theta,\theta')$ can be written as [46]:

$$\overline{\overline{P}}^{mc}(\theta,\theta') = \begin{bmatrix} p_{11}^{mc} & p_{12}^{mc} & 0 & 0 \\ p_{21}^{mc} & p_{22}^{mc} & 0 & 0 \\ 0 & 0 & p_{33}^{mc} & p_{34}^{mc} \\ 0 & 0 & p_{43}^{mc} & p_{44}^{mc} \end{bmatrix} \tag{2.62}$$

$$\overline{\overline{P}}^{ms}(\theta,\theta') = \begin{bmatrix} 0 & 0 & p_{13}^{ms} & p_{14}^{ms} \\ 0 & 0 & p_{23}^{ms} & p_{24}^{ms} \\ p_{31}^{ms} & p_{32}^{ms} & 0 & 0 \\ p_{41}^{ms} & p_{42}^{ms} & 0 & 0 \end{bmatrix} \tag{2.63}$$

By taking advantage of the symmetry of (2.62,2.63), we can decouple equations (2.60,2.61) by first defining

$$\overline{I}^{me}(\theta,z) = \begin{bmatrix} I_v^{mc}(\theta,z) \\ I_h^{mc}(\theta,z) \\ U^{ms}(\theta,z) \\ V^{ms}(\theta,z) \end{bmatrix} \tag{2.64}$$

$$\overline{I}^{mo}(\theta,z) = \begin{bmatrix} I_v^{ms}(\theta,z) \\ I_h^{ms}(\theta,z) \\ U^{mc}(\theta,z) \\ V^{mc}(\theta,z) \end{bmatrix} \tag{2.65}$$

$$\tag{2.66}$$

where superscripts e and o represent the even and odd modes of the Stokes vector. Then, the decoupled equations can be written as

$$\begin{aligned} \cos\theta \frac{d}{dz}\overline{I}^{m\alpha}(\theta,z) &= -\overline{\overline{\kappa}}_e(\theta)\cdot\overline{I}^{m\alpha}(\theta,z) \\ &\quad + \int_0^{\pi} d\theta' \sin\theta' \overline{\overline{P}}^{m\alpha}(\theta,\theta')\cdot\overline{I}^{m\alpha}(\theta',z) \end{aligned} \tag{2.67}$$

where $\alpha = e$ or o (even and odd modes) and

$$\overline{\overline{P}}^{me}(\theta,\theta') = \begin{bmatrix} p_{11}^{mc} & p_{12}^{mc} & -p_{13}^{ms} & -p_{14}^{ms} \\ p_{21}^{mc} & p_{22}^{mc} & -p_{23}^{ms} & -p_{24}^{ms} \\ p_{31}^{ms} & p_{32}^{ms} & p_{33}^{mc} & p_{34}^{mc} \\ p_{41}^{ms} & p_{42}^{ms} & p_{43}^{mc} & p_{44}^{mc} \end{bmatrix} \tag{2.68}$$

$$\overline{\overline{P}}^{mo}(\theta,\theta') = \begin{bmatrix} p_{11}^{mc} & p_{12}^{mc} & p_{13}^{ms} & p_{14}^{ms} \\ p_{21}^{mc} & p_{22}^{mc} & p_{23}^{ms} & p_{24}^{ms} \\ -p_{31}^{ms} & -p_{32}^{ms} & p_{33}^{mc} & p_{34}^{mc} \\ -p_{41}^{ms} & -p_{42}^{ms} & p_{43}^{mc} & p_{44}^{mc} \end{bmatrix} \tag{2.69}$$

Following the same procedure, we can arrive at the new form of the boundary conditions as shown below ($0 < \theta < \pi/2$):

$$\overline{I}^{m\alpha}(\pi-\theta, z=0) = \overline{\overline{T}}_{01}(\theta_0)\cdot\overline{I}_{0i}(\pi-\theta_0) + \overline{\overline{R}}_{10}(\theta)\cdot\overline{I}^{m\alpha}(\theta, z=0) \tag{2.70}$$

$$\overline{I}^{m\alpha}(\theta, z=-d) = \overline{\overline{R}}_{12}(\theta)\cdot\overline{I}^{m\alpha}(\pi-\theta, z=-d) \tag{2.71}$$

where $\overline{\overline{R}}_{\beta\gamma}$ and $\overline{\overline{T}}_{\beta\gamma}$ are the coherent reflection and transmission matrices for planar surface. A more detailed description of $\overline{\overline{R}}_{\beta\gamma}$ and $\overline{\overline{T}}_{\beta\gamma}$ is given in the Appendix A.1.

The incident Stokes vectors for the even and odd modes are, respectively,

$$\overline{I}_{0i}^{me}(\pi-\theta_0) = \begin{bmatrix} I_{v0i} \\ I_{h0i} \\ 0 \\ 0 \end{bmatrix} \tag{2.72}$$

$$\overline{I}_{0i}^{mo}(\pi-\theta_0) = \begin{bmatrix} 0 \\ 0 \\ U_{0i} \\ V_{0i} \end{bmatrix} \tag{2.73}$$

Thus, the scattered Stokes vector in region 0 can be calculated using

$$\overline{I}_{0s}(\theta_0) = \overline{\overline{T}}_{10}(\theta) \cdot \overline{I}^{m\alpha}(\theta, z=0) + \overline{\overline{R}}_{01}(\theta_0) \cdot \overline{I}^{m\alpha}_{0i}(\pi - \theta_0) \tag{2.74}$$

where θ_0(incident angle in region 0) is related to θ by Snell's law.

For both the even and odd modes in (2.67), we can further divide the Stokes vector into $\overline{I}_1(\theta, z)$ and $\overline{I}_2(\theta, z)$ as follows:

$$\overline{I}_1(\theta, z) = \begin{bmatrix} I_v(\theta, z) \\ I_h(\theta, z) \end{bmatrix} \tag{2.75}$$

$$\overline{I}_2(\theta, z) = \begin{bmatrix} U(\theta, z) \\ V(\theta, z) \end{bmatrix} \tag{2.76}$$

Then, (2.67) can be rearranged to take the form shown below:

$$\cos\theta \frac{d}{dz}\overline{I}_1(\theta, z) = -\overline{\overline{\kappa}}_{e1}(\theta) \cdot \overline{I}_1(\theta, z) + \int_0^\pi d\theta' \sin\theta' \left[\overline{\overline{P}}_{11}(\theta, \theta') \cdot \overline{I}_1(\theta', z) + \overline{\overline{P}}_{12}(\theta, \theta') \cdot \overline{I}_2(\theta', z)\right] \tag{2.77}$$

$$\cos\theta \frac{d}{dz}\overline{I}_2(\theta, z) = -\overline{\overline{\kappa}}_{e2}(\theta) \cdot \overline{I}_2(\theta, z) + \int_0^\pi d\theta' \sin\theta' \left[\overline{\overline{P}}_{21}(\theta, \theta') \cdot \overline{I}_1(\theta', z) + \overline{\overline{P}}_{22}(\theta, \theta') \cdot \overline{I}_2(\theta', z)\right] \tag{2.78}$$

where

$$\overline{\overline{\kappa}}_{e1}(\theta) = \begin{bmatrix} \kappa_{e11}(\theta) & 0 \\ 0 & \kappa_{e22}(\theta) \end{bmatrix} \tag{2.79}$$

$$\overline{\overline{\kappa}}_{e2}(\theta) = \begin{bmatrix} \kappa_{e33}(\theta) & \kappa_{e34}(\theta) \\ \kappa_{e43}(\theta) & \kappa_{e44}(\theta) \end{bmatrix} \tag{2.80}$$

$$\overline{\overline{P}}_{11}(\theta,\theta') = \begin{bmatrix} p_{11}(\theta,\theta') & p_{12}(\theta,\theta') \\ p_{21}(\theta,\theta') & p_{22}(\theta,\theta') \end{bmatrix} \tag{2.81}$$

$$\overline{\overline{P}}_{12}(\theta,\theta') = \begin{bmatrix} p_{13}(\theta,\theta') & p_{14}(\theta,\theta') \\ p_{23}(\theta,\theta') & p_{24}(\theta,\theta') \end{bmatrix} \tag{2.82}$$

$$\overline{\overline{P}}_{21}(\theta,\theta') = \begin{bmatrix} p_{31}(\theta,\theta') & p_{32}(\theta,\theta') \\ p_{41}(\theta,\theta') & p_{42}(\theta,\theta') \end{bmatrix} \tag{2.83}$$

$$\overline{\overline{P}}_{22}(\theta,\theta') = \begin{bmatrix} p_{33}(\theta,\theta') & p_{34}(\theta,\theta') \\ p_{43}(\theta,\theta') & p_{44}(\theta,\theta') \end{bmatrix} \tag{2.84}$$

Breaking up $\overline{I}_\gamma$ ($\gamma = 1,2$) into upward ($I_\gamma(\theta,z)$) and downward ($I_\gamma(\pi-\theta,z)$) propagating intensities, we can rewrite (2.77 and 2.78) as:

$$\begin{aligned} \cos\theta \frac{d}{dz}\overline{I}_1(\theta,z) &= -\overline{\overline{\kappa}}_{e1}(\theta)\cdot\overline{I}_1(\theta,z) + \int_0^{\pi/2} d\theta' \sin\theta' \\ &\Big[\overline{\overline{P}}_{11}(\theta,\theta')\cdot\overline{I}_1(\theta',z) + \overline{\overline{P}}_{11}(\theta,\pi-\theta')\cdot\overline{I}_1(\pi-\theta',z) \\ &+ \overline{\overline{P}}_{12}(\theta,\theta')\cdot\overline{I}_2(\theta',z) + \overline{\overline{P}}_{12}(\theta,\pi-\theta')\cdot\overline{I}_2(\pi-\theta',z)\Big] \end{aligned} \tag{2.85}$$

$$\begin{aligned} -\cos\theta \frac{d}{dz}\overline{I}_1(\pi-\theta,z) &= -\overline{\overline{\kappa}}_{e1}(\theta)\cdot\overline{I}_1(\pi-\theta,z) + \int_0^{\pi/2} d\theta' \sin\theta' \\ &\Big[\overline{\overline{P}}_{11}(\theta,\pi-\theta')\cdot\overline{I}_1(\theta',z) + \overline{\overline{P}}_{11}(\theta,\theta')\cdot\overline{I}_1(\pi-\theta',z) \\ &- \overline{\overline{P}}_{12}(\theta,\pi-\theta')\cdot\overline{I}_2(\theta',z) - \overline{\overline{P}}_{12}(\theta,\theta')\cdot\overline{I}_2(\pi-\theta',z)\Big] \end{aligned} \tag{2.86}$$

$$\cos\theta \frac{d}{dz}\overline{I}_2(\theta,z) = -\overline{\overline{\kappa}}_{e2}(\theta)\cdot\overline{I}_2(\theta,z) + \int_0^{\pi/2} d\theta' \sin\theta'$$

$$\Big[\overline{\overline{P}}_{21}(\theta,\theta')\cdot\overline{I}_1(\theta',z)+\overline{\overline{P}}_{21}(\theta,\pi-\theta')\cdot\overline{I}_1(\pi-\theta',z)$$

$$+\overline{\overline{P}}_{22}(\theta,\theta')\cdot\overline{I}_2(\theta',z)+\overline{\overline{P}}_{22}(\theta,\pi-\theta')\cdot\overline{I}_2(\pi-\theta',z)\Big] \tag{2.87}$$

$$-\cos\theta\frac{d}{dz}\overline{I}_2(\pi-\theta,z) = -\overline{\overline{\kappa}}_{e2}(\theta)\cdot\overline{I}_2(\pi-\theta,z)+\int_0^{\pi/2}d\theta'\sin\theta'$$

$$\Big[-\overline{\overline{P}}_{21}(\theta,\pi-\theta')\cdot\overline{I}_1(\theta',z)-\overline{\overline{P}}_{21}(\theta,\theta')\cdot\overline{I}_1(\pi-\theta',z)$$

$$+\overline{\overline{P}}_{22}(\theta,\pi-\theta')\cdot\overline{I}_2(\theta',z)+\overline{\overline{P}}_{22}(\theta,\theta')\cdot\overline{I}_2(\pi-\theta',z)\Big] \tag{2.88}$$

2.5.2 Gaussian Quadrature Method

The integrals in the radiative transfer theory can be replaced with a weighted sum over n intervals between n zeroes of the even-order Legendre polynomial. Thus, the discretized elevation angles are chosen so that the cosine of the angles correspond to the zeroes (μ) of the Legendre polynomial. Letting $f(\cos\theta)$ be a function of $\cos\theta$, the Gaussian quadrature integration method is given by [46]:

$$\int_0^{\pi/2}d\theta\ \sin\theta\ f(\cos\theta)\approx\sum_{i=1}^{n}a_i f(\mu_i) \tag{2.89}$$

where a_i are known as the associated Christoffel weighting functions. The Gaussian quadrature method is used to discretize equations (2.85)-(2.88) into $4n$ first order ordinary differential equations where n is the number of discretized elevation angles.

The equations are shown below:

$$\overline{\overline{\mu}}' \cdot \frac{d}{dz}\overline{I}_1^+ = -\overline{\overline{\kappa}}_{e1} \cdot \overline{I}_1^+ + \overline{\overline{F}}_{11} \cdot \overline{\overline{a}}' \cdot \overline{I}_1^+ + \overline{\overline{B}}_{11} \cdot \overline{\overline{a}}' \cdot \overline{I}_1^- + \overline{\overline{F}}_{12} \cdot \overline{\overline{a}}' \cdot \overline{I}_2^+ + \overline{\overline{B}}_{12} \cdot \overline{\overline{a}}' \cdot \overline{I}_2^- \tag{2.90}$$

$$-\overline{\overline{\mu}}' \cdot \frac{d}{dz}\overline{I}_1^- = -\overline{\overline{\kappa}}_{e1} \cdot \overline{I}_1^- + \overline{\overline{B}}_{11} \cdot \overline{\overline{a}}' \cdot \overline{I}_1^+ + \overline{\overline{F}}_{11} \cdot \overline{\overline{a}}' \cdot \overline{I}_1^- - \overline{\overline{B}}_{12} \cdot \overline{\overline{a}}' \cdot \overline{I}_2^+ - \overline{\overline{F}}_{12} \cdot \overline{\overline{a}}' \cdot \overline{I}_2^- \tag{2.91}$$

$$\overline{\overline{\mu}}' \cdot \frac{d}{dz}\overline{I}_2^+ = -\overline{\overline{\kappa}}_{e2} \cdot \overline{I}_2^+ + \overline{\overline{F}}_{21} \cdot \overline{\overline{a}}' \cdot \overline{I}_1^+ + \overline{\overline{B}}_{21} \cdot \overline{\overline{a}}' \cdot \overline{I}_1^- + \overline{\overline{F}}_{22} \cdot \overline{\overline{a}}' \cdot \overline{I}_2^+ + \overline{\overline{B}}_{22} \cdot \overline{\overline{a}}' \cdot \overline{I}_2^- \tag{2.92}$$

$$-\overline{\overline{\mu}}' \cdot \frac{d}{dz}\overline{I}_2^- = -\overline{\overline{\kappa}}_{e2} \cdot \overline{I}_2^- - \overline{\overline{B}}_{21} \cdot \overline{\overline{a}}' \cdot \overline{I}_1^+ - \overline{\overline{F}}_{21} \cdot \overline{\overline{a}}' \cdot \overline{I}_1^- + \overline{\overline{B}}_{22} \cdot \overline{\overline{a}}' \cdot \overline{I}_2^+ + \overline{\overline{F}}_{22} \cdot \overline{\overline{a}}' \cdot \overline{I}_2^- \tag{2.93}$$

where $\overline{I}_1^{\pm}$ and $\overline{I}_2^{\pm}$ are $2n \times 1$ vectors

$$\overline{I}_1^{\pm} = \begin{bmatrix} I_v(\pm\mu_1, z) \\ \vdots \\ I_v(\pm\mu_n, z) \\ I_h(\pm\mu_1, z) \\ \vdots \\ I_h(\pm\mu_n, z) \end{bmatrix} \quad \overline{I}_2^{\pm} = \begin{bmatrix} U(\pm\mu_1, z) \\ \vdots \\ U(\pm\mu_n, z) \\ V(\pm\mu_1, z) \\ \vdots \\ V(\pm\mu_n, z) \end{bmatrix} \tag{2.94}$$

and $\overline{\overline{F}}_{\alpha\beta}$ and $\overline{\overline{B}}_{\alpha\beta}$ are $2n \times 2n$ matrices

$$\overline{\overline{F}}_{\alpha\beta} = \begin{bmatrix} P_{\alpha\beta_{11}}(\mu_1,\mu_1) & \cdots & P_{\alpha\beta_{11}}(\mu_1,\mu_n) & P_{\alpha\beta_{12}}(\mu_1,\mu_1) & \cdots & P_{\alpha\beta_{12}}(\mu_1,\mu_n) \\ \vdots & \vdots & \vdots & \vdots & \vdots & \vdots \\ P_{\alpha\beta_{11}}(\mu_n,\mu_1) & \cdots & P_{\alpha\beta_{11}}(\mu_n,\mu_n) & P_{\alpha\beta_{12}}(\mu_n,\mu_1) & \cdots & P_{\alpha\beta_{12}}(\mu_n,\mu_n) \\ P_{\alpha\beta_{21}}(\mu_1,\mu_1) & \cdots & P_{\alpha\beta_{21}}(\mu_1,\mu_n) & P_{\alpha\beta_{22}}(\mu_1,\mu_1) & \cdots & P_{\alpha\beta_{22}}(\mu_1,\mu_n) \\ \vdots & \vdots & \vdots & \vdots & \vdots & \vdots \\ P_{\alpha\beta_{21}}(\mu_n,\mu_1) & \cdots & P_{\alpha\beta_{21}}(\mu_n,\mu_n) & P_{\alpha\beta_{22}}(\mu_n,\mu_1) & \cdots & P_{\alpha\beta_{22}}(\mu_n,\mu_n) \end{bmatrix} \tag{2.95}$$

$$\overline{\overline{B}}_{\alpha\beta} = \begin{bmatrix} P_{\alpha\beta_{11}}(\mu_1,-\mu_1) & \cdots & P_{\alpha\beta_{11}}(\mu_1,-\mu_n) & P_{\alpha\beta_{12}}(\mu_1,-\mu_1) & \cdots & P_{\alpha\beta_{12}}(\mu_1,-\mu_n) \\ \vdots & \vdots & \vdots & \vdots & \vdots & \vdots \\ P_{\alpha\beta_{11}}(\mu_n,-\mu_1) & \cdots & P_{\alpha\beta_{11}}(\mu_n,-\mu_n) & P_{\alpha\beta_{12}}(\mu_n,-\mu_1) & \cdots & P_{\alpha\beta_{12}}(\mu_n,-\mu_n) \\ P_{\alpha\beta_{21}}(\mu_1,-\mu_1) & \cdots & P_{\alpha\beta_{21}}(\mu_1,-\mu_n) & P_{\alpha\beta_{22}}(\mu_1,-\mu_1) & \cdots & P_{\alpha\beta_{22}}(\mu_1,-\mu_n) \\ \vdots & \vdots & \vdots & \vdots & \vdots & \vdots \\ P_{\alpha\beta_{21}}(\mu_n,-\mu_1) & \cdots & P_{\alpha\beta_{21}}(\mu_n,-\mu_n) & P_{\alpha\beta_{22}}(\mu_n,-\mu_1) & \cdots & P_{\alpha\beta_{22}}(\mu_n,-\mu_n) \end{bmatrix} \tag{2.96}$$

and $\overline{\overline{\mu}}'$ and $\overline{\overline{a}}'$ are $2n \times 2n$ diagonal matrices

$$\overline{\overline{\mu}}' = \text{diag}\,[\mu_1,\cdots,\mu_n,\mu_1,\cdots,\mu_n] \tag{2.97}$$

$$\overline{\overline{a}}' = \text{diag}\,[a_1,\cdots,a_n,a_1,\cdots,a_n] \tag{2.98}$$

where $\pm\mu_i$ are the zeroes of the Legendre polynomial $P_{2n}(\mu)$ and a_i are the corresponding Christoffel weighting functions. Note that $a_i = a_{-i}$ and $\mu_i = -\mu_{-i}$.

The system of $8n$ first-order differential equations, (2.90)-(2.93), can be further simplified by defining

$$\overline{I}_a = \begin{bmatrix} \overline{I}_1^+ + \overline{I}_1^- \\ \overline{I}_2^+ - \overline{I}_2^- \end{bmatrix} \quad \overline{I}_s = \begin{bmatrix} \overline{I}_1^+ - \overline{I}_1^- \\ \overline{I}_2^+ + \overline{I}_2^- \end{bmatrix} \tag{2.99}$$

and rearranging the equations. The simplified equations are shown below:

$$\overline{\overline{\mu}} \cdot \frac{d}{dz}\overline{I}_a = \overline{\overline{W}} \cdot \overline{I}_s \tag{2.100}$$

$$\overline{\overline{\mu}} \cdot \frac{d}{dz}\overline{I}_s = \overline{\overline{A}} \cdot \overline{I}_a \tag{2.101}$$

where $\overline{\overline{W}}$ and $\overline{\overline{A}}$ are the $4n \times 4n$ matrices

$$\overline{\overline{W}} = -\begin{bmatrix} \overline{\overline{\kappa}}_{e1} & 0 \\ 0 & \overline{\overline{\kappa}}_{e2} \end{bmatrix} + \begin{bmatrix} (\overline{\overline{F}}_{11} - \overline{\overline{B}}_{11}) & (\overline{\overline{F}}_{12} + \overline{\overline{B}}_{12}) \\ (\overline{\overline{F}}_{21} - \overline{\overline{B}}_{21}) & (\overline{\overline{F}}_{22} + \overline{\overline{B}}_{22}) \end{bmatrix} \cdot \overline{\overline{a}} \tag{2.102}$$

$$\overline{\overline{A}} = -\begin{bmatrix} \overline{\overline{\kappa}}_{e1} & 0 \\ 0 & \overline{\overline{\kappa}}_{e2} \end{bmatrix} + \begin{bmatrix} (\overline{\overline{F}}_{11} + \overline{\overline{B}}_{11}) & (\overline{\overline{F}}_{12} - \overline{\overline{B}}_{12}) \\ (\overline{\overline{F}}_{21} + \overline{\overline{B}}_{21}) & (\overline{\overline{F}}_{22} - \overline{\overline{B}}_{22}) \end{bmatrix} \cdot \overline{\overline{a}} \tag{2.103}$$

and $\overline{\overline{\mu}}$ and $\overline{\overline{a}}$ are $4n \times 4n$ diagonal matrices

$$\overline{\overline{\mu}} = \text{diag}\,[\mu_1, \cdots, \mu_n, \mu_1, \cdots, \mu_n, \mu_1, \cdots, \mu_n, \mu_1, \cdots, \mu_n] \tag{2.104}$$

$$\overline{\overline{a}} = \text{diag}\,[a_1, \cdots, a_n, a_1, \cdots, a_n, a_1, \cdots, a_n, a_1, \cdots, a_n] \tag{2.105}$$

2.5.3 Eigenanalysis Solution

The homogeneous solution for equations (2.100) and (2.101) are of the form

$$\overline{I}_a = \overline{I}_{ao} e^{\alpha z} \tag{2.106}$$

$$\overline{I}_s = \overline{I}_{so} e^{\alpha z} \tag{2.107}$$

Substituting these two equations into (2.100) and (2.101), we have

$$\overline{\overline{\mu}} \cdot \alpha \overline{I}_{ao} e^{\alpha z} = \overline{\overline{W}} \cdot \overline{I}_{so} e^{\alpha z} \tag{2.108}$$

$$\overline{\overline{\mu}} \cdot \alpha \overline{I}_{so} e^{\alpha z} = \overline{\overline{A}} \cdot \overline{I}_{ao} e^{\alpha z} \tag{2.109}$$

The $4n$ eigenvalue equations can be obtained by rearranging the above two equations:

$$\left(\overline{\overline{\mu}}^{-1} \cdot \overline{\overline{W}} \cdot \overline{\overline{\mu}}^{-1} \cdot \overline{\overline{A}} - \alpha^2 \overline{\overline{I}}\right) \cdot \overline{I}_{ao} = 0 \tag{2.110}$$

$$\overline{I}_{so} = \alpha^{-1} \cdot \overline{\overline{\mu}}^{-1} \cdot \overline{\overline{A}} \cdot \overline{I}_{ao} \tag{2.111}$$

where $\overline{\overline{I}}$ is an identity matrix. This is an eigenvalue problem with eigenvalues $\pm\alpha_i$. The corresponding eigenvectors $\overline{I}_{ai}$ can be obtained to form the eigenmatrix $\overline{\overline{E}}$ ($4n \times 4n$ matrix). The solutions will be

$$\overline{I}_a = \overline{E} \cdot \overline{\overline{D}}(z) \cdot \frac{\overline{x}}{2} + \overline{E} \cdot \overline{\overline{U}}(z+d) \cdot \frac{\overline{y}}{2} \tag{2.112}$$

$$\overline{I}_s = \overline{\overline{Q}} \cdot \overline{\overline{D}}(z) \cdot \frac{\overline{x}}{2} - \overline{\overline{Q}} \cdot \overline{\overline{U}}(z+d) \cdot \frac{\overline{y}}{2} \tag{2.113}$$

where

$$\overline{\overline{D}}(z) = \text{diag}\left[e^{\alpha_1 z}, \cdots, e^{\alpha_{4n} z}\right] \tag{2.114}$$

$$\overline{\overline{U}}(z) = \text{diag}\left[e^{-\alpha_1 z}, \cdots, e^{-\alpha_{4n} z}\right] \tag{2.115}$$

$$\overline{\overline{Q}} = \overline{\overline{\mu}}^{-1} \cdot \overline{\overline{A}} \cdot \overline{E} \cdot \overline{\overline{\alpha}}^{-1} \tag{2.116}$$

$$\overline{\overline{\alpha}} = \text{diag}\,[\alpha_1, \cdots, \alpha_{4n}] \tag{2.117}$$

and $\overline{x}$ and $\overline{y}$ are $4n \times 1$ unknown vectors which can be solved by matching the boundary conditions.

We can write these equations in term of Stokes vector by using equation (2.99), and the final form of the solutions will be:

$$\overline{I}^{+}(z) = (\overline{E} + \overline{\overline{Q}}) \cdot \overline{\overline{D}}(z) \cdot \overline{x} + (\overline{E} - \overline{\overline{Q}}) \cdot \overline{\overline{U}}(z+d) \cdot \overline{y} \tag{2.118}$$

$$\overline{I}^{-}(z) = (\overline{E}' + \overline{\overline{Q}}') \cdot \overline{\overline{D}}(z) \cdot \overline{x} + (\overline{E}' - \overline{\overline{Q}}') \cdot \overline{\overline{U}}(z+d) \cdot \overline{y} \tag{2.119}$$

where

$$\overline{\overline{E}}' = \overline{\overline{\mu}}^{-1} \cdot \overline{\overline{W}}' \cdot \overline{\overline{Q}} \cdot \overline{\overline{\alpha}}^{-1} \tag{2.120}$$

$$\overline{\overline{Q}}' = \overline{\overline{\mu}}^{-1} \cdot \overline{\overline{A}}' \cdot \overline{E} \cdot \overline{\overline{\alpha}}^{-1} \tag{2.121}$$

and

$$\overline{\overline{W}}' = -\begin{bmatrix} \overline{\overline{\kappa}}_{e1} & 0 \\ 0 & -\overline{\overline{\kappa}}_{e2} \end{bmatrix} + \begin{bmatrix} (\overline{\overline{F}}_{11} - \overline{\overline{B}}_{11}) & (\overline{\overline{F}}_{12} + \overline{\overline{B}}_{12}) \\ -(\overline{\overline{F}}_{21} - \overline{\overline{B}}_{21}) & -(\overline{\overline{F}}_{22} + \overline{\overline{B}}_{22}) \end{bmatrix} \cdot \overline{\overline{a}} \tag{2.122}$$

$$\overline{\overline{A}}' = -\begin{bmatrix} -\overline{\overline{\kappa}}_{e1} & 0 \\ 0 & \overline{\overline{\kappa}}_{e2} \end{bmatrix} + \begin{bmatrix} -(\overline{\overline{F}}_{11} + \overline{\overline{B}}_{11}) & -(\overline{\overline{F}}_{12} - \overline{\overline{B}}_{12}) \\ (\overline{\overline{F}}_{21} + \overline{\overline{B}}_{21}) & (\overline{\overline{F}}_{22} - \overline{\overline{B}}_{22}) \end{bmatrix} \cdot \overline{\overline{a}} \tag{2.123}$$

The unknowns $\overline{x}$ and $\overline{y}$ of the upward and downward propagating intensities can be obtained by matching the solutions with the boundary conditions shown below:

$$\overline{I}^{+}(z=-d) = \overline{\overline{R}}_{12} \cdot \overline{I}^{-}(z=-d) \tag{2.124}$$

$$\overline{I}^{-}(z=0) = \overline{\overline{R}}_{10} \cdot \overline{I}^{+}(z=0) + \overline{\overline{T}}_{01} \cdot \overline{I}_{0i}^{-} \tag{2.125}$$

where $\overline{\overline{R}}_{12}$ and $\overline{\overline{R}}_{10}$ are the $4n \times 4n$ reflection matrices and $\overline{\overline{T}}_{01}$ is the $4n \times 4n$ transmission matrix at n discrete quadrature angles.

Since I_{0i}^{-} is a delta function, the discretization of it will be in the form of [55]

$$\left[\overline{I}_{0i}^{-}\right]_j = \left[\overline{I}_{0i}\right]_j \frac{\delta_{jk}\epsilon_0 \cos\theta_{0k}}{a_j \epsilon_1' \cos\theta_k} \tag{2.126}$$

Substituting equations (2.118),(2.119),(2.126) into the boundary conditions (2.124),(2.125), we obtain the following system of $8n \times 8n$ equations

$$\begin{bmatrix} (\overline{E}' + \overline{\overline{Q}}') - \overline{\overline{R}}_{10} \cdot (\overline{E} + \overline{\overline{Q}}) & \left\{(\overline{E}' - \overline{\overline{Q}}') - \overline{\overline{R}}_{10} \cdot (\overline{E} - \overline{\overline{Q}})\right\} \overline{\overline{D}}(-d) \\ \left\{(\overline{E} + \overline{\overline{Q}}) - \overline{\overline{R}}_{12} \cdot (\overline{E}' + \overline{\overline{Q}}')\right\} \overline{\overline{D}}(-d) & (\overline{E} - \overline{\overline{Q}}) - \overline{\overline{R}}_{12} \cdot (\overline{E}' - \overline{\overline{Q}}') \end{bmatrix} \cdot \begin{bmatrix} \overline{x} \\ \overline{y} \end{bmatrix} = \begin{bmatrix} \overline{\overline{T}}_{01} \cdot \overline{I}_{0i}^{-} \\ 0 \end{bmatrix} \tag{2.127}$$

$\overline{x}$ and $\overline{y}$ can be calculated by solving the linear algebra equation above and then substituted into (2.118) to obtain $\overline{I}^{+}(z=0)$. The scattered Stokes vector in region 0 is given by the equation below (from (2.74)):

$$\overline{I}_{0s} = \overline{\overline{T}}_{10} \cdot \overline{I}^{+}(z=0) + \overline{\overline{R}}_{01} \cdot \overline{I}_{0i}^{-} \tag{2.128}$$

The above calculation process is repeated for each harmonic, and the total scattered intensities in region 0 can be obtained by reconstructing the Fourier series for the even and odd modes as follows:

$$\begin{aligned}
\overline{I}_{os}(\phi_o) = & \left\{\overline{\overline{R}}_{01} + \overline{\overline{T}}_{10} \cdot \left[\overline{\overline{I}} - \overline{\overline{R}}_{10} \cdot \overline{\overline{R}}_{12} \cdot exp[-\overline{\overline{\mu}}^{-1} \cdot \overline{\overline{K}}_e d]\right]^{-1} \cdot \overline{\overline{T}}_{01}\right\} \\
& \cdot \overline{I}_{oi}\delta(\phi_o - \phi_{oi}) + \sum_{m=0}^{m_{max}} \left\{\overline{\overline{T}}_{10} \cdot \left[\overline{I}^{mc+}(z=0)\right.\right. \\
& \left. - \left[\overline{\overline{I}} - \overline{\overline{R}}_{10} \cdot \overline{\overline{R}}_{12} \cdot exp[-\overline{\overline{\mu}}^{-1} \cdot \overline{\overline{K}}_e d]\right]^{-1} \cdot \overline{\overline{T}}_{01} \cdot \overline{I}_{oi}^{mc}\right] \\
& \left. \cdot \cos m(\phi_o - \phi_{oi}) + \overline{\overline{T}}_{10} \cdot \overline{I}^{ms+}(z=0) \sin m(\phi_o - \phi_{oi})\right\}
\end{aligned} \tag{2.129}$$

2.6 Theoretical Results and Discussion

THe sensitivity of the theoretical results to the change in the model parameters is examined in this section. Figure 2.4 shows the numerical solution for a two layer medium with embedded spherical scatterers. The fractional volume of the randomly orientated scatterers is 5 % and the dimension is 0.05 cm for the a, b and c axes. The permittivity of the scatterers is $(40+i10.0)\epsilon_o$ and the permittivity of the background medium is $(3.15+i0.0017)\epsilon_o$. The frequency is 5 GHz and the thickness of region 1 is assumed to be infinite. For parts (a) and (b) of Figure 2.4, the bistatic coefficients for VV, HV, VH and HH are plotted against the incident angle (θ_i). The scattered angle (θ_s) is the same as the incident angle (θ_i) and the scattered direction is the same as the incident ϕ direction. For this case, the co-polarized scattering coefficients (VV and HH) are the same and the difference between the co-polarized returns (VV and HH) and cross-polarized returns (VH and HV) is about 20 dB. For comparison, the plots for scattered direction where $\phi = 180^o$ are also included in parts (c) and (d) of Figure 2.4. Generally, they show the same trend.

Parts (e) and (f) of Figure 2.4 are for ($\phi = 90^o$). The interesting part is that the co-polarized scattering coefficients (HH and VV) now behave differently. In order to better understand the theoretical results, we consider the scattering pattern from a single spherical scatterer. When the size of the scatterer (0.05 cm) is small compared to the wavelength (6 cm), the Rayleigh scattering can be used to describe the scattering mechanism involved. When an electromagnetic wave is incident upon a single spherical scatterer, it will induce surface current on the scatterer, and then the sphere will act as a dipole and re-radiate the scattered field. The pattern of the

radiated power is of a donut shape. For the HH case, the scattered electric field is always perpendicular to the dipole of a HH receiver at $\phi = 90^o$ for all θ. Thus, for a two layer medium with randomly distributed spherical scatterers, the scattered HH should be almost the same level for different θ. This can be shown in part (e) of Figure 2.4. On the other hand, for the VV case, the scattered electric field is perpendicular to the dipole of the VV receiver at $\theta = 0^o$ and gradually aligns to it as the looking angle (θ_s) increases. This explains why the bistatic coefficient for VV in the direction of $\phi = 90^O$ increases with the observing angle (θ_s). For a more complete derivation and explanation of the scattering from a single dipole, please refer to Appendix C.

Next, the calculated bistatic scattering coefficients for both co-polarized and cross-polarized returns (VV, HV, VH and HH) are plotted against the azimuthal angle (ϕ) for different scattered angles (θ_s). The incident angle (θ_i) is the same as the scattered angle (θ_s). When the observing angle (θ_s) is close to the surface normal, we expect the co-polarized returns (VV and HH) to be higher than the cross-polarized returns (VH and HV) at $\phi = 0^o$. This is because the scattered field for VV and HH will be parallel to the axis of the dipole of the respective receiving antenna. As we move the direction of observation from $\phi = 0^o$ to $\phi = 90^o$, the co-polarized receiver (VV and HH) will gradually lose its alignment with the scattered field of the induced dipole (See Appendix C). This will decrease the received level of co-polarized returns and increase the cross-polarized returns. The trend is clearly shown in parts (a) and (b) of Figure 2.5.

As we increase the observing angle (θ_s), we notice that the symmetry of the

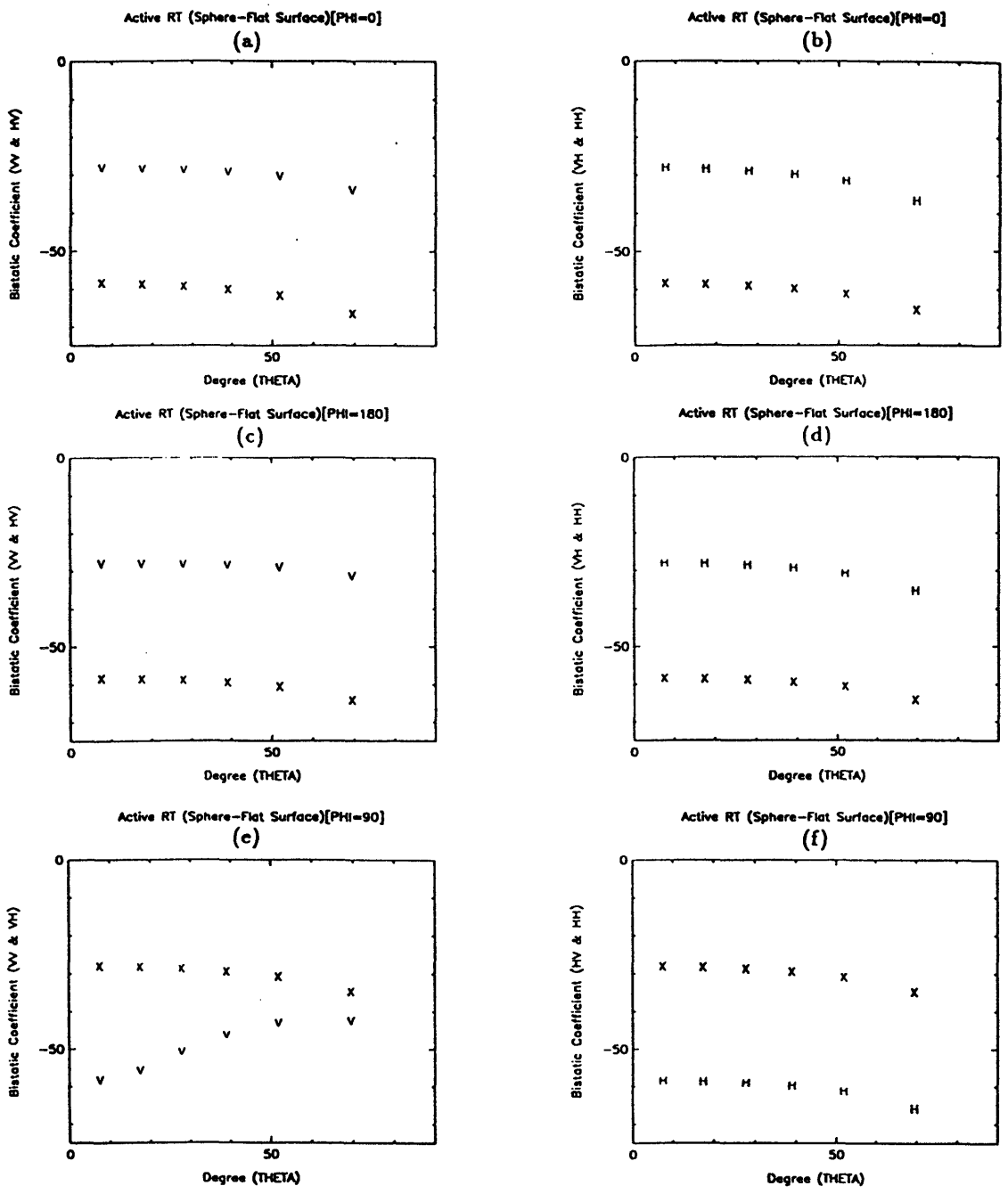

Figure 2.4: Bistatic scattering coefficients are plotted against scattered angle θ_s for different azimuthal angles. The incident angle θ_i is the same as the scattered angle θ_s.

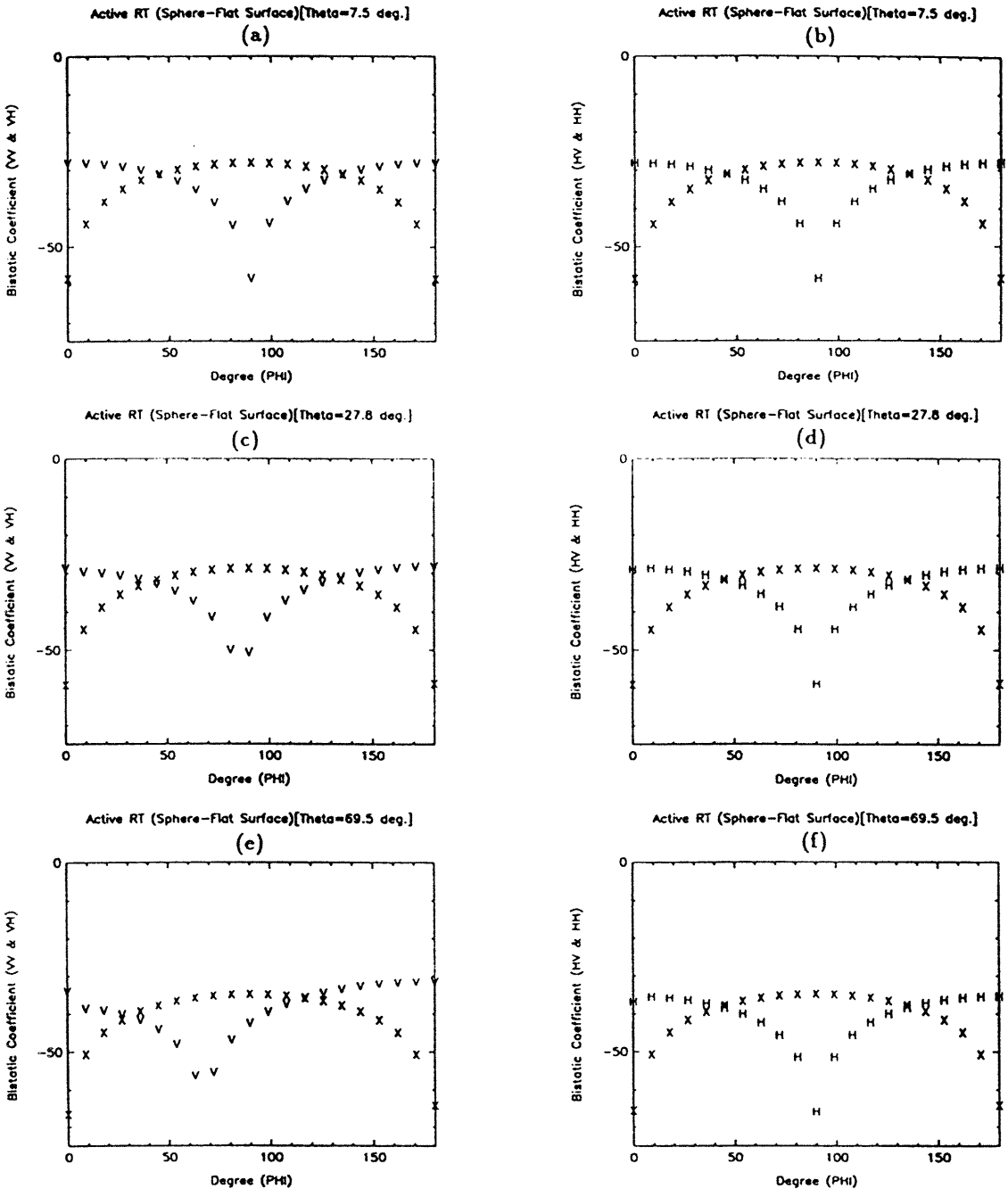

Figure 2.5: Bistatic scattering coefficients are plotted against scattered angle ϕ_s for different elevation angles (θ). The incident angle θ_i is the same as the scattered angle θ_s.

VV curve no longer exists but the HH curve continues to show symmetry about the center of the plot. Parts (c), (d), (e) and (f) of Figure 2.5 clearly demonstrate this trend. The minimum of VV apparently shifts to the left hand side of the graph (to smaller ϕ angle). Referring to Appendix C, it can be shown that because of the geometrical shape of the dipole radiation pattern, the scattered electric field pattern from a spherical scatterer will be perpendicular to the dipole axis of the VV receiver at different azimuthal angles (ϕ_s) for different incident angles (θ). However, this does not happen in the HH scattered returns as the axis of the induced dipole on the scatterer is always perpendicular to the plane of the incidence for different incident angles (θ_i) and the dipole axis of the HH receiver will always be perpendicular to the scattered $\overline{E}$ field at $\phi = 90°$. Thus, moving the HH receiver in the azimuthal direction to observe the horizontally polarized scattered field will give us the same curve form for different elevation angles.

The numerical calculations are repeated for different values of imaginary part of the permittivity of the scatterers (Case 1 to Case 4, ϵ''_{1s}=[0.0] ϵ_0, [10.0]ϵ_0, [20.0]ϵ_0 and [30.0]ϵ_0) as shown in Figures 2.6 and 2.7. This corresponds to the albedo (κ_s/κ_e) of 0.09021, 0.00758, 0.00474 and 0.00409. Generally, the bistatic coefficients for all angles (θ_s) increase as we decrease ϵ''_{1s}. From the definition of albedo, we know that high albedo means that the ratio of scattering extinction over the overall extinction is high and thus the higher scattered returns. Therefore, as we add an imaginary part (ϵ''_{1s}) to the permittivity of the scatters in region 1, they become lossy which decreases the bistatic coefficients as well as the albedo. However, as we increase ϵ''_{1s} further, the returns decrease only by a small amount. This is due to the fact that

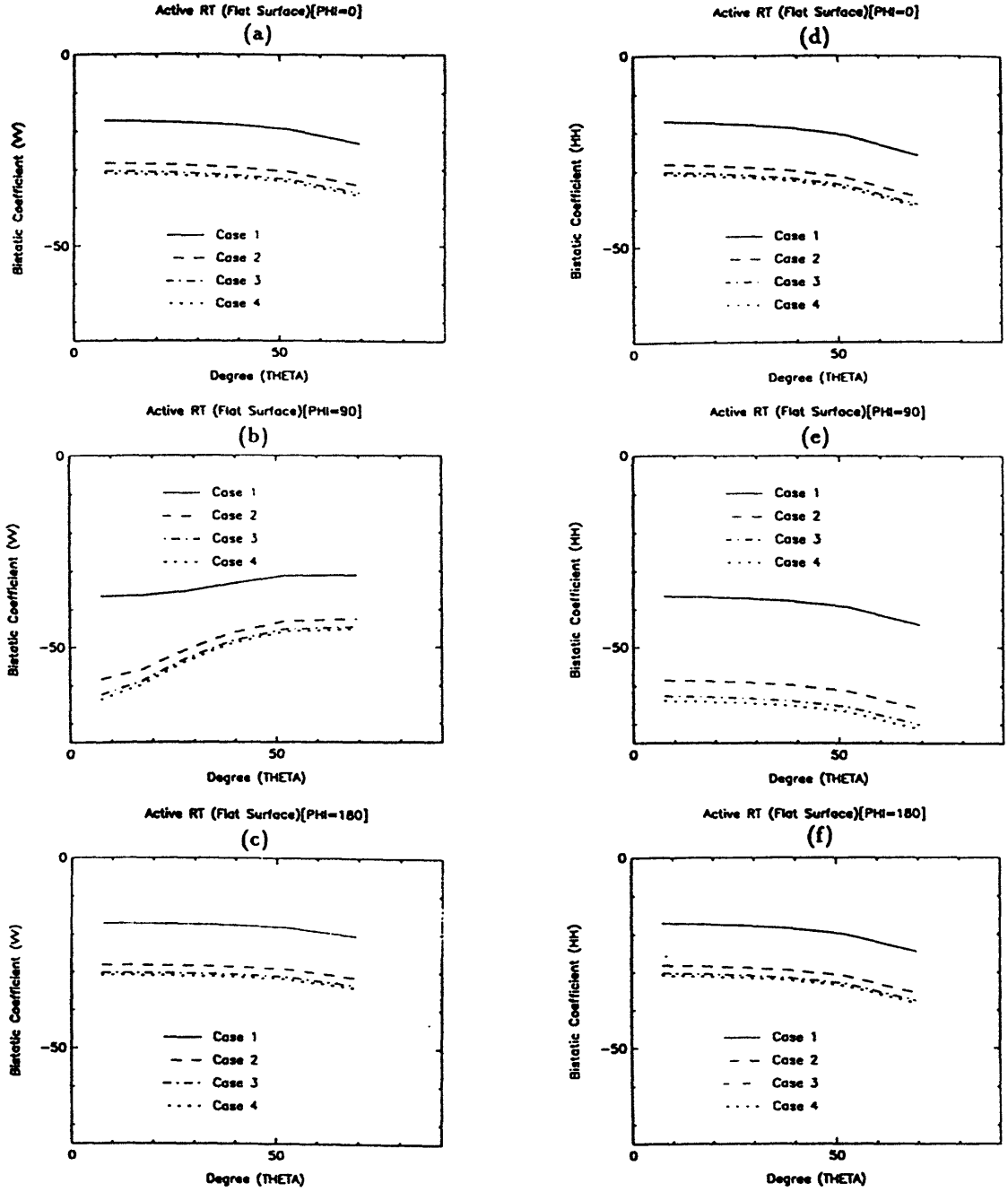

Figure 2.6: Bistatic scattering coefficients are plotted against scattered angle ϕ_s for different elevation angles (θ). Case 1 to 4: κ_s/κ_e= 0.09021, 0.00758, 0.00474 and 0.00409. (a), (b) and (c) are for VV and (d), (e) and (f) are for HH.

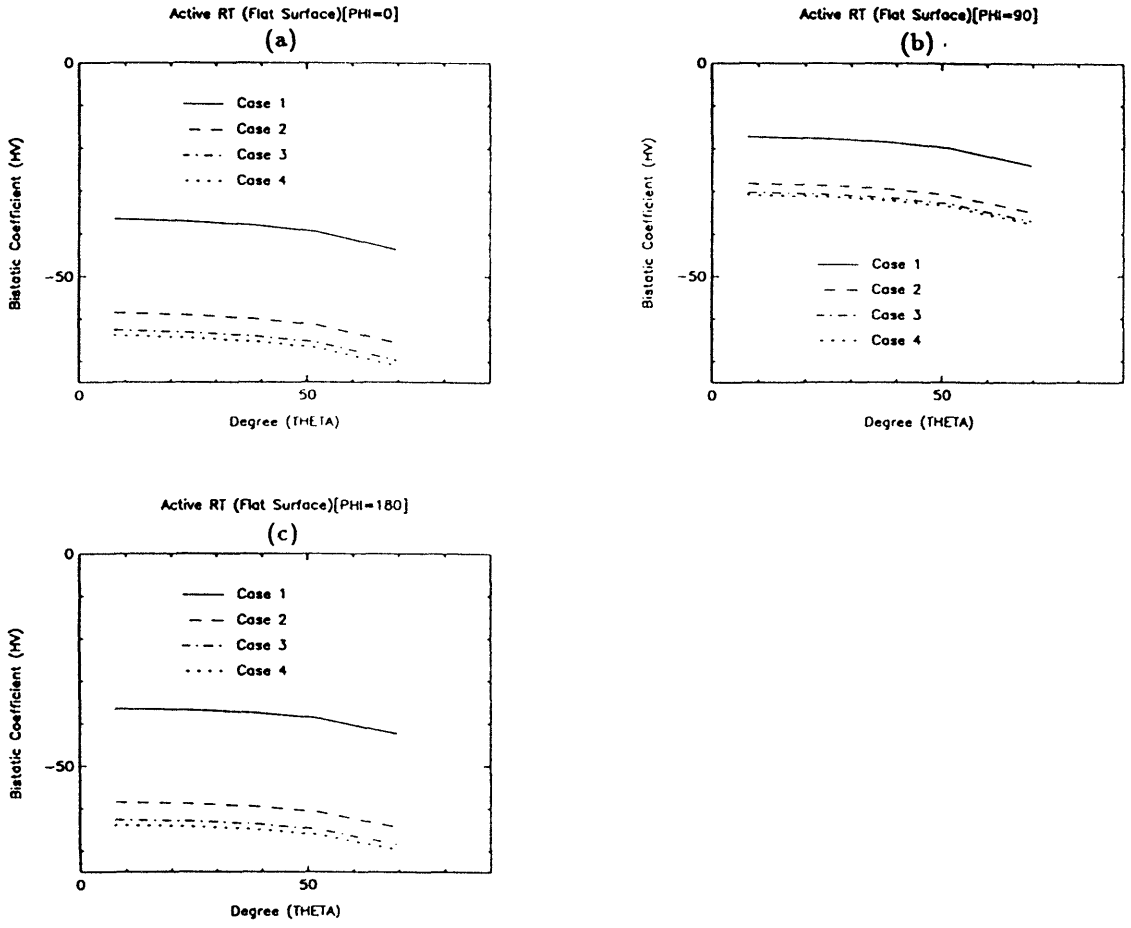

Figure 2.7: Bistatic scattering coefficients (HV) are plotted against scattered angle ϕ_s for different elevation angles (θ). Case 1 to 4: κ_s/κ_e= 0.09021, 0.00758, 0.00474 and 0.00409.

the scattering loss of the scatterers is also dependent on the difference between the background permittivity (ϵ_b) and the permittivity of the scatterers. The higher the difference is, the stronger the scattered field is. This effect can be shown in the local Fresnel reflection coefficient. As we increases ϵ''_{1b} further, the attenuation due to the absorption loss will be compensated by the increase of the scattering loss. This effect can be shown clearly by the leveling off of the albedo. Parts (a), (b) and (c) of Figure 2.6 show this trend for the VV case, whereas similar plots are drawn for the HH case in parts (d), (e) and (f) of Figure 2.6. The HV case is demonstrated in parts (a), (b) and (c) of Figure 2.7. For each case, the graphs for $\phi = 0^0$, $\phi = 90^0$ and $\phi = 180^0$ are plotted.

Next we investigate the effect of different scatterer shapes on the calculated bistatic coefficients. A halfspace medium is again considered. The frequency used is 5 GHz and the background medium has a permittivity of $[3.15 + i0.002]\epsilon_0$ and 5% fractional volume of vertically orientated scatterers. The various scatterer shapes selected are spheres (a = 0.02 cm, b = 0.02 cm, c= 0.02 cm), prolate spheroids (a = 0.01 cm, b = 0.01 cm, c = 0.08 cm), prolate ellipsoids (a = 0.02 cm, b = 0.005 cm, c = 0.08 cm), oblate spheroids (a = 0.04 cm , b = 0.04 cm, c = 0.005 cm) and oblate ellipsoids (a = 0.08cm, b = 0.02 cm, c = 0.005 cm). Figure 2.8 shows the different shapes of the scatterers chosen. The permittivity of the scatterers is $[40.0 + i30.0]\epsilon_0$. The dimensions of the scatterers are chosen so that the volume occupied by them is the same regardless of their different shapes. In each case, the numerical solution is calculated for each of the shape of the scatterers mentioned above.

A first glance at parts (a) and (b) of Figure 2.9 and parts (a) and (b) of

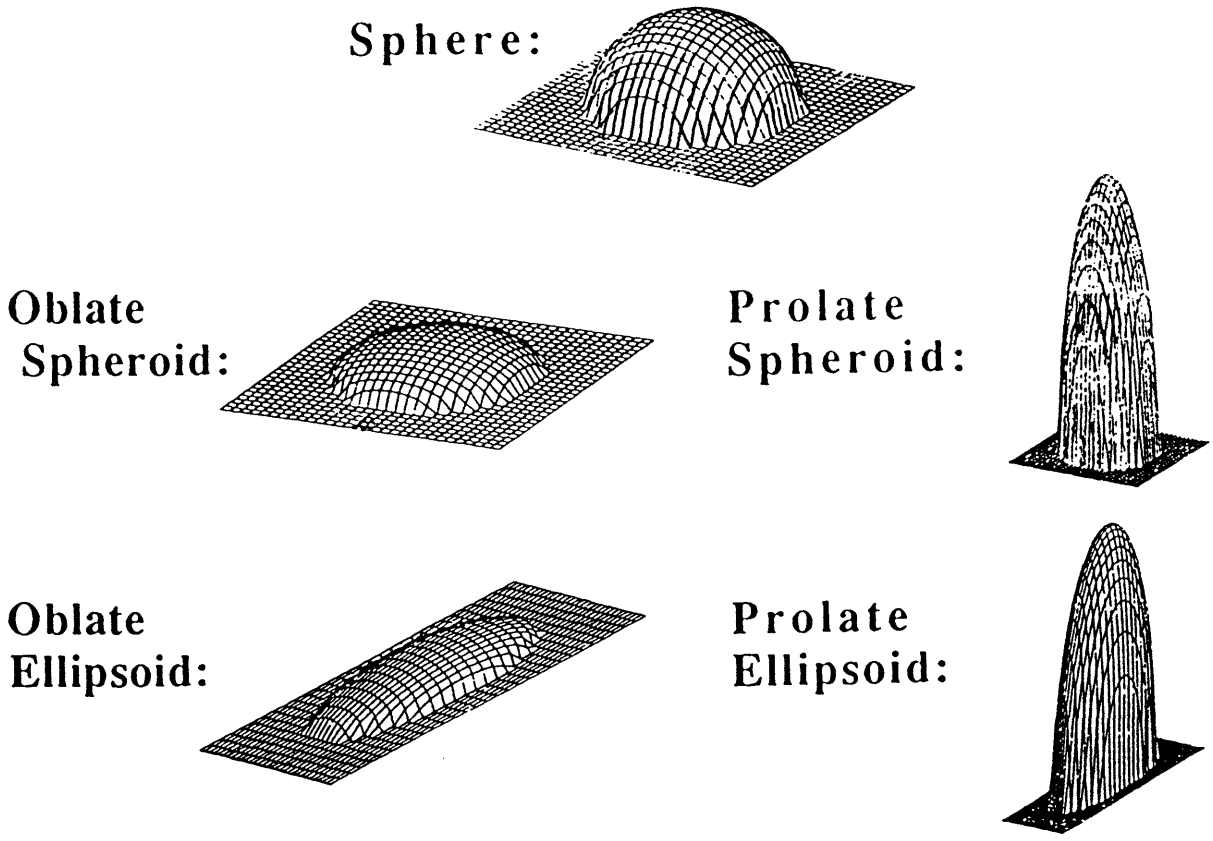

Figure 2.8: Different shapes of scatterers.

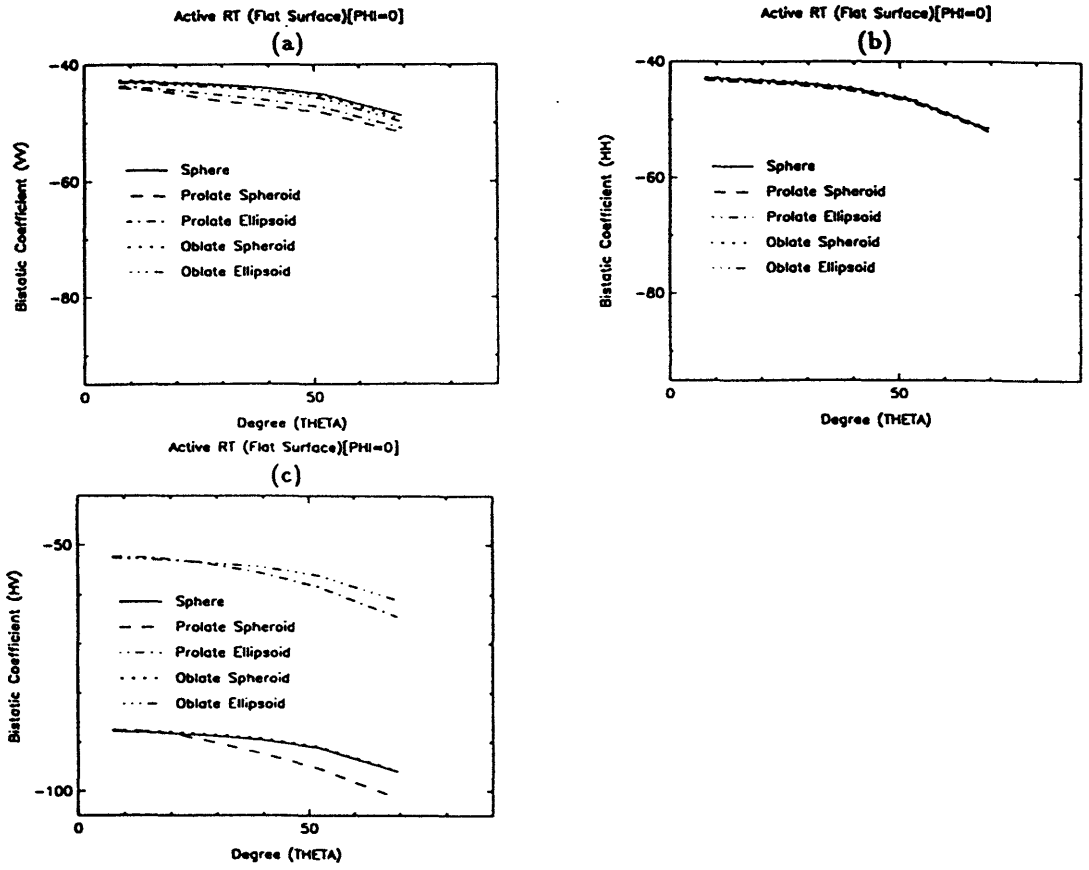

Figure 2.9: Bistatic scattering coefficients are plotted against scattered angle θ_s for different shapes of scatterers. The looking angle is at $\phi = 0^o$.

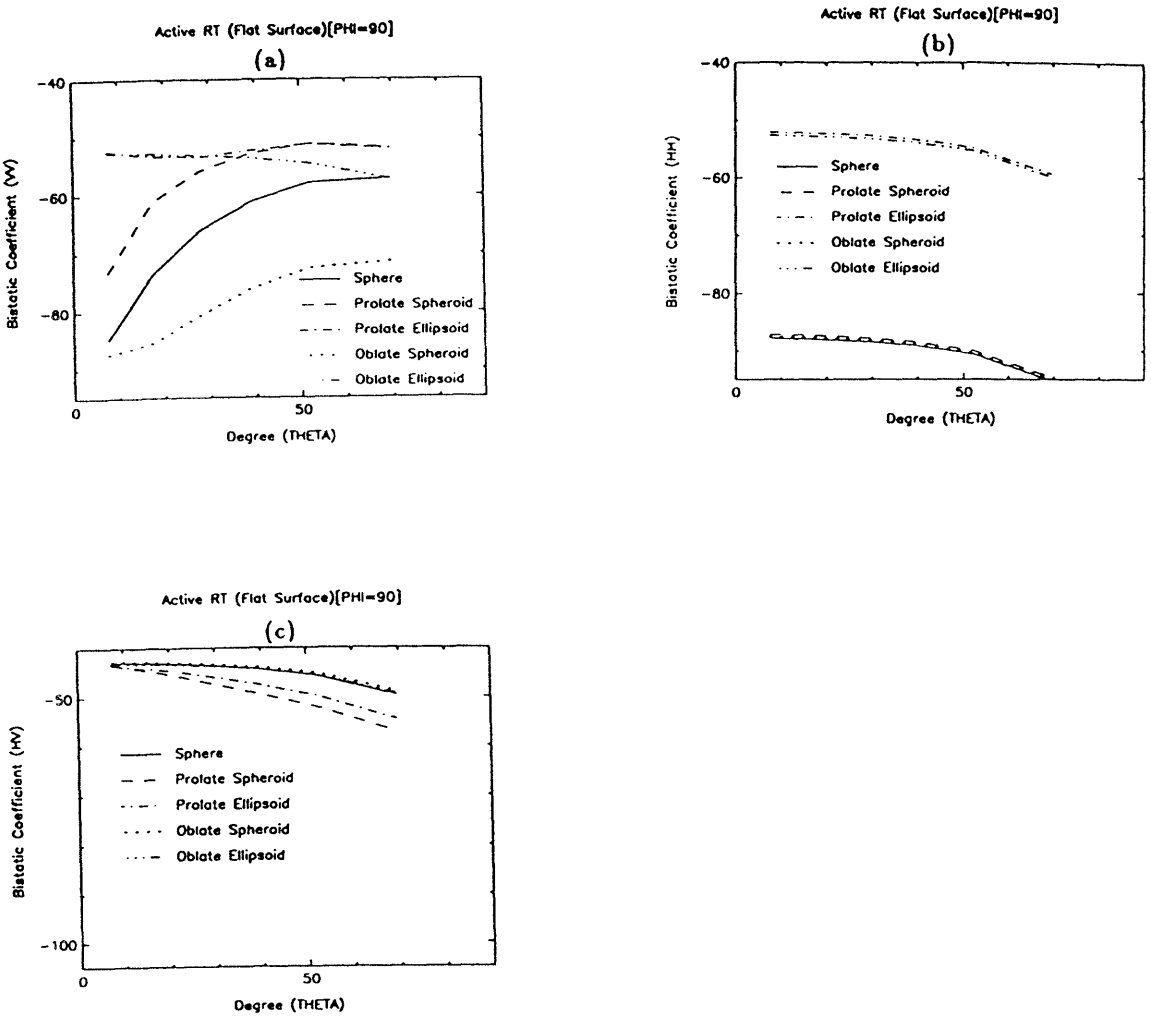

Figure 2.10: Bistatic scattering coefficients are plotted against scattered angle θ_s for different shapes of scatterers. The looking angle is at $\phi = 180°$.

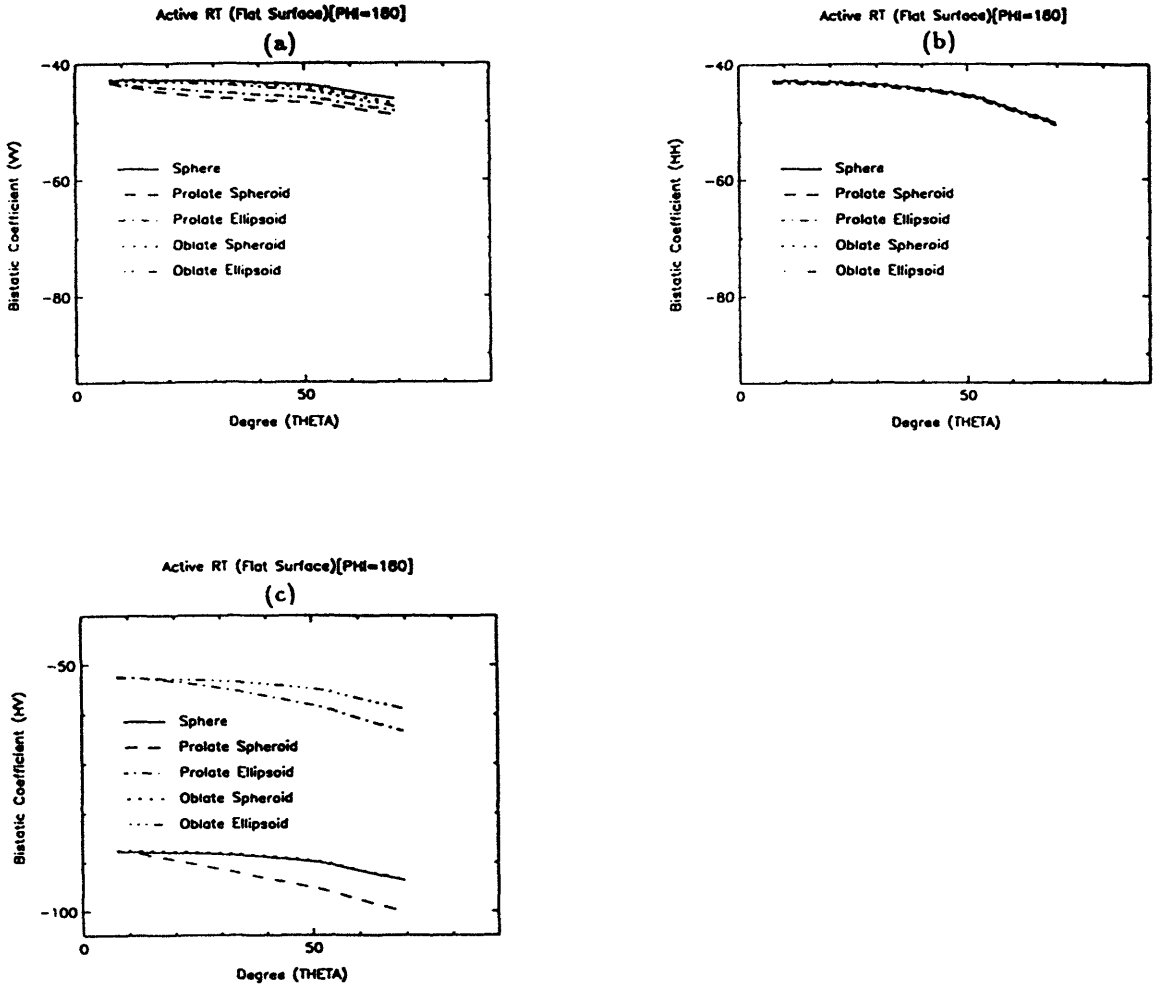

Figure 2.11: Bistatic scattering coefficients are plotted against scattered angle θ_s for different shapes of scatterers. The looking angle is at $\phi = 90^o$.

Figure 2.10 shows that the VV and HH returns at $\phi = 0^o$ (forward direction) and $\phi = 180^o$ (backscattering direction) do not depend greatly on the shape of the scatterers. For the HV case, because the returns for spheres and spheroidal scatterers only come from the multiple scattering effects, their returns are lower than those of ellipsoidal scatterers. Now, if we look at the plots (Figure 2.11) for the case when the incident wave comes in at $\phi = 0^o$ and the receiver is looking at $\phi = 90^o$, the VV and HH returns for ellipsoidal scatterers are higher than those of the spherical and spheroidal scatterers at low angle θ. For the VV case, because of the geometrical effect described in Figure 2.4, the bistatic coefficients for the spherical and spheroidal scatterers will gradually rise as shown in part (a) of Figure 2.11. Note that the effect is larger for prolate spheroids than for oblate spheroids due to their shapes. Also, as expected, at $\phi = 90^o$, the HV returns for all shapes of the scatterers are almost the same.

2.7 Summary

In this chapter, the configuration of the two layer medium with ellipsoid inclusions was presented. The formulation of the numerical method involved was explained in detail. laid out step by step. Definitions of the parameters used were properly inserted where they are necessary. The brief introduction to the radiative transfer theory, the extinction matrix and the phase matrix, was followed by the elaboration of the numerical techniques based on ice. Finally, the theoretical calculations were carried out for different sets of input parameters and the trends for each case were studied. It was found that generally the co-polarized bistatic scattering coefficients

are higher than the cross-polarized bistatic scattering coefficients when the observing angle is close to either $\phi = 0^o$ or $\phi = 180^O$, whereas the opposite is true when the receiver is looking at $\phi = 90^o$. It is shown that HH returns will always start high at $\phi = 0^o$ and reach a minimum point at $\phi = 90^o$ and then rise again to a maximum at $\phi = 180^o$ for different elevation angles. On the other hand, though the VV returns show a rather similar trend, the curve will reach its minimum sooner (smaller ϕ) as we increase the elevation angle θ_s. This can be easily explained by considering the scattering from a single scatterer. The multiple scattering effects are also important and account for the cross-polarized returns observed. Numerical solutions were then calculated for different values of the imaginary part of the permittivity of the scatterers. The results show that the actual scattering and absorption phenomena are more complicated. Increasing the imaginary part of the permittivity of the scatterers on one hand make the scatterers more lossy and on the other hand increase the scattering loss. Finally, a study of the effects of different shapes of the scatterers on the bistatic scattering coefficients was carried out. From the various plots presented, it is clear that the bistatic returns for different shapes of scatterers show a slightly different curve form from the spherical scatterers.

Chapter 3

Theoretical Model for a Two Layer Random Medium with Rough Interfaces

3.1 Configuration and Definition

The theoretical model for a two layer random medium discussed in Chapter 2 is modified to incorporate rough interfaces. In this case, two scattering mechanisms are involved: volume scattering and rough surface scattering. The effects of rough surface scattering is investigated in this chapter.

Rough surfaces can generally be classified by two surface parameters, the root mean square (RMS) height of the surface and the correlation length. Let $h(\overline{r})$ be the height of a point on the rough surface relative to a planar reference surface and $\overline{r}$ is the position vector for points on the reference surface. Then, the root mean square (RMS) height of the surface is given by

$$\sigma_{rms} = \sqrt{\langle (h(\overline{r}))^2 \rangle_s} \tag{3.1}$$

where $\langle \cdots \rangle_s$ means spatial average. The other important parameter is correlation length, which indicates the rate of change of surface height with distance along the surface. A surface correlation function can be defined by

$$C(\overline{R}) = \frac{\langle h(\overline{r})h(\overline{r}+\overline{R})\rangle_s}{\sigma^2} \tag{3.2}$$

and the correlation length is the distance over which the correlation function falls by 1/e.

Over the years, several methods have been developed to calculate scattering from rough surfaces. Depending on the surface parameters (roughness, correlation length), different methods are used, though so far no exact solution for a general case is available. When the radius of curvature of the surface is large, the Kirchhoff's approximation can be used [57]. In the case where the wavelength is small compared to the scale of roughness, the Geometrical Optics approximation (GO) is used. If the surface RMS height is much smaller than the wavelength, the Small Perturbation Method (SPM) is applied [57,58]. Scattering from randomly perturbed periodic and quasiperiodic surfaces has also been studied [59].

In this thesis, the small perturbation method (SPM) is used. The Extended Boundary Condition (EBC) formulation is applied to obtain the SPM solutions [57]. First, the scattered and transmitted fields are expressed as a function of the surface tangential fields using the extinction theorem and Huygens' principle. Since the surface height and derivatives are small, the tangential fields can then be expanded in a perturbation series and solved for each order, using the previous order solutions.

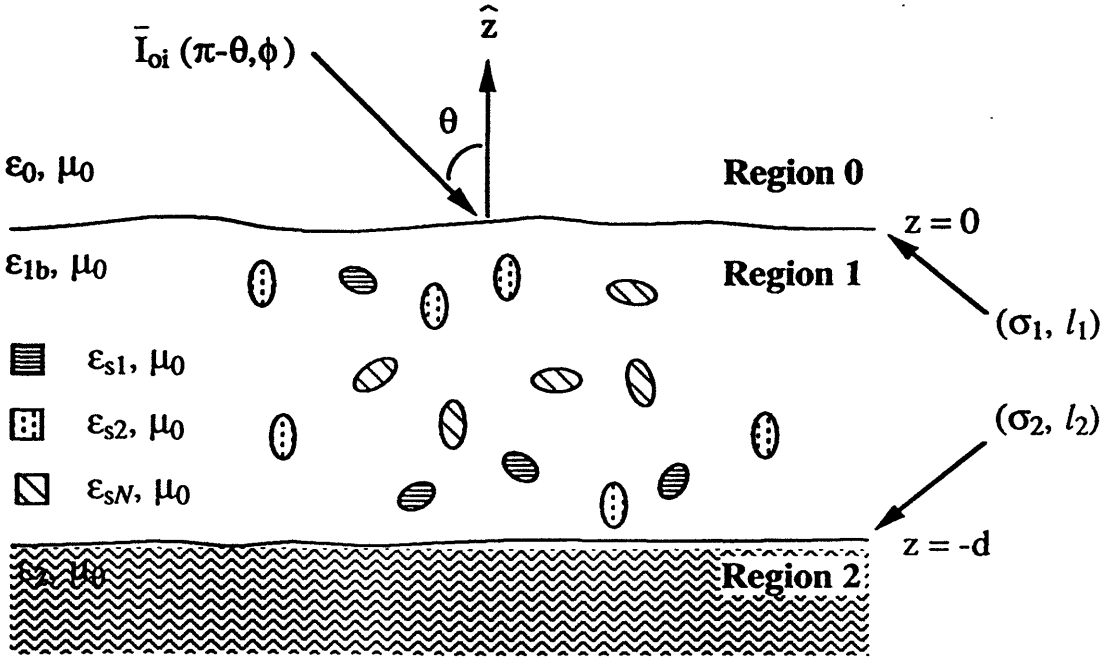

Figure 3.1: Configuration for two layer medium with rough interfaces with different types of scatterers.

The configuration for the two-layer random medium with rough interfaces is shown in Figure 3.1. The planar interfaces in two-layer model in Chapter 2 are replaced with rough interfaces. The surface profile function and the spatial correlation of this function are assumed to be Gaussian. As shown in the same figure, the top and bottom interfaces may have different roughness parameters. Scatterers with different sizes, shapes, orientations and dielectric constants are embedded in region 1 (thickness = d). The dielectric constant of the background medium in region 1 is denoted as ϵ_{1b} and those of region 0 and region 2 are respectively ϵ_0 and ϵ_2.

3.2 Boundary Condition

The reflection and transmission matrices for a rough surface consist of two parts: coherent and incoherent. The coherent part, which accounts for the specular term, obeys Snell's law of reflection and transmission, whereas the incoherent part includes the diffuse reflection and transmission due to rough surface scattering. Therefore, the boundary conditions in Chapter 2 must be modified to take care of this extra term. The boundary conditions at the top and bottom rough interfaces are shown below:

Interface 0:

$$\begin{aligned}\overline{I}(\pi-\theta,\phi,z=0) &= \overline{\overline{R}}^{c}_{10}(\theta,\phi)\cdot\overline{I}(\theta,\phi,z=0)\\ &+ \int_0^{2\pi}d\phi'\int_0^{\frac{\pi}{2}}d\theta'\sin\theta'\,\overline{\overline{R}}^{i}_{10}(\theta,\phi;\theta',\phi')\cdot\overline{I}(\theta',\phi',z=0)\\ &+ \overline{\overline{T}}^{c}_{01}(\theta_0,\phi_0)\cdot\overline{I}_{0i}(\pi-\theta_0,\phi_0)\\ &+ \overline{\overline{T}}^{i}_{01}(\theta,\phi;\theta_{0i},\phi_{0i})\cdot\overline{I}_{0i} \qquad (3.3)\end{aligned}$$

Interface 1:

$$\begin{aligned}\overline{I}(\theta,\phi,z=-d) &= \overline{\overline{R}}^{c}_{12}(\theta,\phi)\cdot\overline{I}(\pi-\theta,\phi,z=-d)\\ &+ \int_0^{2\pi}d\phi'\int_0^{\frac{\pi}{2}}d\theta'\sin\theta'\,\overline{\overline{R}}^{i}_{12}(\theta,\phi;\theta',\phi')\\ &\cdot\overline{I}(\pi-\theta',\phi',z=-d) \qquad (3.4)\end{aligned}$$

where

$$\overline{\overline{R}}_{\alpha\beta}(\theta,\phi;\theta',\phi') = \overline{\overline{R}}^{c}_{\alpha\beta}(\theta,\phi)\ \delta(\phi-\phi')\ \delta(\cos\theta - cos\theta') + \overline{\overline{R}}^{i}_{\alpha\beta}(\theta,\phi;\theta',\phi') \quad (3.5)$$

$$\overline{\overline{T}}_{\alpha\beta}(\theta,\phi;\theta',\phi') = \overline{\overline{T}}^{c}_{\alpha\beta}(\theta,\phi)\ \delta(\phi-\phi')\ \delta(\cos\theta - cos\theta') + \overline{\overline{T}}^{i}_{\alpha\beta}(\theta,\phi;\theta',\phi') \quad (3.6)$$

Thus, the scattered intensities in region 0 will be

$$\begin{aligned}\overline{I}_{0s}(\theta_0,\phi_0,z=0) &= \overline{\overline{R}}^{c}_{01}(\theta_0,\phi_0)\cdot\overline{I}_{0i}(\pi-\theta_0,\phi_0) \\ &+ \overline{\overline{R}}^{i}_{01}(\theta_0,\phi_0;\theta_{0i},\phi_{0i})\cdot\overline{I}_{0i} \\ &+ \overline{\overline{T}}^{c}_{10}(\theta,\phi)\cdot\overline{I}(\theta,\phi,z=0) \\ &+ \int_0^{2\pi}d\phi'\int_0^{\frac{\pi}{2}}d\theta'\sin\theta'\ \overline{\overline{T}}^{i}_{10}(\theta_0,\phi_0;\theta',\phi')\cdot\overline{I}(\theta',\phi',z=0) \quad (3.7)\end{aligned}$$

where the coherent components ($\overline{\overline{R}}^{c}$, $\overline{\overline{T}}^{c}$) couple the incident intensity into the specular reflection and transmission directions while the incoherent components ($\overline{\overline{R}}^{i}$, $\overline{\overline{T}}^{i}$) couple to all reflection and transmission directions.

The elements of the bistatic scattering matrix $\overline{\overline{\gamma}}$ can then be calculated by

$$\gamma_{\alpha\beta}(\theta_s,\phi_s;\theta_i,\phi_i) = 4\pi\frac{\cos\theta_s I_{\alpha 0s}(\theta_s,\phi_s)}{\cos\theta_i I_{\beta 0i}} \qquad \alpha,\beta = 1,2,3,4 \quad (3.8)$$

where I_1, I_2, I_3 and I_4 are respectively I_v, I_h, U and V of the Stokes vector.

3.3 Numerical Solution

3.3.1 Fourier Series Expansion and Even and Odd Modes

Following the same approach presented in Chapter 2, we apply the Fourier series expansion to the radiative transfer equation to eliminate the ϕ-dependence of the equation. We let

$$\bar{I}_{oi}(\pi-\theta_o;\phi_o) = \bar{I}_{oi}\delta(\cos\theta_o-\cos\theta_{oi})\sum_{m=0}^{\infty}\frac{1}{(1+\delta_m)\pi}\cos m(\phi_o-\phi_{oi}) \tag{3.9}$$

and, for α,β=0,1,2,

$$\bar{\bar{R}}^c_{\alpha\beta}(\theta,\phi;\theta',\phi') = \bar{\bar{R}}^c_{\alpha\beta}(\theta)\delta(\cos\theta-\cos\theta')\sum_{m=0}^{\infty}\frac{1}{(1+\delta_m)\pi}\cos m(\phi-\phi') \tag{3.10}$$

$$R^i_{\alpha\beta}(\theta,\phi;\theta',\phi') = \sum_{m=0}^{\infty}\frac{1}{(1+\delta_{m0})\pi}\left[R^{mc}_{\alpha\beta}(\theta,\theta')\cos m(\phi-\phi')+R^{ms}_{\alpha\beta}(\theta,\theta')\sin m(\phi-\phi')\right] \tag{3.11}$$

$$\bar{\bar{T}}^c_{01}(\theta,\phi;\theta'_o,\phi'_o) = \bar{\bar{T}}^c_{01}(\theta_o)\delta(\cos\theta_o-\cos\theta'_o)\sum_{m=0}^{\infty}\frac{1}{(1+\delta_m)\pi}\cos m(\phi-\phi') \tag{3.12}$$

$$T^i_{01}(\theta,\phi;\theta'_o,\phi'_o) = \sum_{m=0}^{\infty}\frac{1}{(1+\delta_{m0})\pi}\left[T^{mc}_{01}(\theta,\theta'_o)\cos m(\phi_o-\phi'_o)+T^{ms}_{01}(\theta,\theta'_o)\sin m(\phi_o-\phi'_o)\right] \tag{3.13}$$

where θ_o and θ are related by the Snell's law.

Equations (3.9)-(3.13) can then be substituted into equations (3.3),(3.4) and

(3.7). The $d\phi'$ and $d\phi'_o$ integrations are carried out. After that, the boundary conditions are restructured into the even and odd modes following the definitions in Chapter 2. The decoupled boundary conditions can be expressed as

$$\begin{aligned}
\overline{I}^{m\alpha}(\pi-\theta, z=0) &= \overline{\overline{R}}^{c}_{10}(\theta)\cdot\overline{I}^{m\alpha}(\theta, z=0) \\
&+ \int_0^{\frac{\pi}{2}} d\theta' \sin\theta' \, \overline{\overline{R}}^{m\alpha}_{10}(\theta,\theta')\cdot\overline{I}^{m\alpha}(\theta', z=0) \\
&+ \overline{\overline{T}}^{c}_{01}(\theta_0)\cdot\overline{I}^{m\alpha}_{0i}(\pi-\theta_0) \\
&+ \overline{\overline{T}}^{m\alpha}_{01}(\theta,\theta_{0i})\cdot\overline{I}_{0i} \qquad (3.14) \\
\overline{I}(\theta, z=-d) &= \overline{\overline{R}}^{c}_{12}(\theta)\cdot\overline{I}(\pi-\theta, z=-d) \\
&+ \int_0^{\frac{\pi}{2}} d\theta' \sin\theta' \, \overline{\overline{R}}^{m\alpha}_{12}(\theta,\theta')\cdot\overline{I}(\pi-\theta', z=-d) \qquad (3.15)
\end{aligned}$$

and the scattered field in region 0 is expressed as

$$\begin{aligned}
\overline{I}^{m\alpha}_{0s}(\theta_0, z=0) &= \overline{\overline{R}}^{c}_{01}(\theta_0)\cdot\overline{I}^{m\alpha}_{0i}(\pi-\theta_0) \\
&+ \overline{\overline{R}}^{m\alpha}_{01}(\theta_0,\theta_{0i})\cdot\overline{I}^{m\alpha}_{0i} \\
&+ \overline{\overline{T}}^{c}_{10}(\theta)\cdot\overline{I}^{m\alpha}(\theta, z=0) \\
&+ \int_0^{\frac{\pi}{2}} d\theta' \sin\theta' \, \overline{\overline{T}}^{m\alpha}_{10}(\theta_0,\theta')\cdot\overline{I}^{m\alpha}(\theta', z=0) \qquad (3.16)
\end{aligned}$$

where for $A = R$ or T, and $\alpha, \beta = 0, 1, 2,$

$$\overline{\overline{A}}_{\alpha\beta}^{me}(\theta,\theta') = \begin{bmatrix} A^{mc}_{\alpha\beta_{11}}(\theta,\theta') & A^{mc}_{\alpha\beta_{12}}(\theta,\theta') & -A^{ms}_{\alpha\beta_{13}}(\theta,\theta') & -A^{ms}_{\alpha\beta_{14}}(\theta,\theta') \\ A^{mc}_{\alpha\beta_{21}}(\theta,\theta') & A^{mc}_{\alpha\beta_{22}}(\theta,\theta') & -A^{ms}_{\alpha\beta_{23}}(\theta,\theta') & -A^{ms}_{\alpha\beta_{24}}(\theta,\theta') \\ A^{ms}_{\alpha\beta_{31}}(\theta,\theta') & A^{ms}_{\alpha\beta_{32}}(\theta,\theta') & A^{mc}_{\alpha\beta_{33}}(\theta,\theta') & A^{mc}_{\alpha\beta_{34}}(\theta,\theta') \\ A^{ms}_{\alpha\beta_{41}}(\theta,\theta') & A^{ms}_{\alpha\beta_{42}}(\theta,\theta') & A^{mc}_{\alpha\beta_{43}}(\theta,\theta') & A^{mc}_{\alpha\beta_{44}}(\theta,\theta') \end{bmatrix} \quad (3.17)$$

$$\overline{\overline{A}}_{\alpha\beta}^{mo}(\theta,\theta') = \begin{bmatrix} A^{mc}_{\alpha\beta_{11}}(\theta,\theta') & A^{mc}_{\alpha\beta_{12}}(\theta,\theta') & A^{ms}_{\alpha\beta_{13}}(\theta,\theta') & A^{ms}_{\alpha\beta_{14}}(\theta,\theta') \\ A^{mc}_{\alpha\beta_{21}}(\theta,\theta') & A^{mc}_{\alpha\beta_{22}}(\theta,\theta') & A^{ms}_{\alpha\beta_{23}}(\theta,\theta') & A^{ms}_{\alpha\beta_{24}}(\theta,\theta') \\ -A^{ms}_{\alpha\beta_{31}}(\theta,\theta') & -A^{ms}_{\alpha\beta_{32}}(\theta,\theta') & A^{mc}_{\alpha\beta_{33}}(\theta,\theta') & A^{mc}_{\alpha\beta_{34}}(\theta,\theta') \\ -A^{ms}_{\alpha\beta_{41}}(\theta,\theta') & -A^{ms}_{\alpha\beta_{42}}(\theta,\theta') & A^{mc}_{\alpha\beta_{43}}(\theta,\theta') & A^{mc}_{\alpha\beta_{44}}(\theta,\theta') \end{bmatrix} \quad (3.18)$$

The expression for the coherent and incoherent matrices for both reflection and transmission matrices can be found in Appendix A.2. The incident intensity in region 0 is then

$$\overline{I}^{m\alpha}_{0i}(\pi - \theta_0) = \overline{I}^{m\alpha}_{0i} \cdot \delta(\cos\theta_0 - \cos\theta_0') \quad (3.19)$$

3.3.2 Discretization and Eigenanalysis Solution

Breaking up the intensities into upward (+) and downward (-) propagating intensities, and applying the Gaussian quadrature method, the boundary conditions can now be expressed as

$$\overline{I}^{+}(z=-d) = \left(\overline{\overline{R}}^{c}_{12} + \overline{\overline{R}}^{m\alpha}_{12} \cdot \overline{\overline{a}}\right) \cdot \overline{I}^{-}(z=-d) \quad (3.20)$$

$$\overline{I}^{-}(z=0) = \left(\overline{\overline{R}}^{c}_{10} + \overline{\overline{R}}^{m\alpha}_{10} \cdot \overline{\overline{a}}\right) \cdot \overline{I}^{+}(z=0) + \left(\overline{\overline{T}}^{c}_{01} \cdot \overline{\overline{\delta}} + \overline{\overline{T}}^{m\alpha}_{01}\right) \cdot \overline{I}^{m\alpha}_{0i} \quad (3.21)$$

where $\overline{\overline{a}}$ is $4n \times 4n$ a diagonal matrix containing the Christoffel weighting functions a_i

$$\overline{\overline{a}} = \text{diag}\,[a_1, \ldots, a_n, a_1, \ldots, a_n, a_1, \ldots, a_n, a_1, \ldots, a_n] \tag{3.22}$$

and

$$\begin{aligned}\overline{\overline{\delta}} \;=\; \text{diag}\Bigg[&\frac{\epsilon_0 \cos\theta_{0_1}}{\epsilon_1' \cos\theta_1}, \ldots, \frac{\epsilon_0 \cos\theta_{0_n}}{\epsilon_1' \cos\theta_n}, \frac{\epsilon_0 \cos\theta_{0_1}}{\epsilon_1' \cos\theta_1}, \ldots, \frac{\epsilon_0 \cos\theta_{0_n}}{\epsilon_1' \cos\theta_n}, \\ &\frac{\epsilon_0 \cos\theta_{0_1}}{\epsilon_1' \cos\theta_1}, \ldots, \frac{\epsilon_0 \cos\theta_{0_n}}{\epsilon_1' \cos\theta_n}, \frac{\epsilon_0 \cos\theta_{0_1}}{\epsilon_1' \cos\theta_1}, \ldots, \frac{\epsilon_0 \cos\theta_{0_n}}{\epsilon_1' \cos\theta_n}\Bigg]\end{aligned} \tag{3.23}$$

which are the constants from the discretization of the delta function.

Following the same procedure in the previous chapter, we come to a system of $8n \times 8n$ equations:

$$\begin{aligned}&\begin{bmatrix} (\overline{\overline{E}}' + \overline{\overline{Q}}') - (\overline{\overline{R}}_{10}^{\,c} + \overline{\overline{R}}_{10}^{\,m\alpha} \cdot \overline{a}) \cdot (\overline{\overline{E}} + \overline{\overline{Q}}) \\ \left\{(\overline{\overline{E}} + \overline{\overline{Q}}) - (\overline{\overline{R}}_{12}^{\,c} + \overline{\overline{R}}_{12}^{\,m\alpha} \cdot \overline{a}) \cdot (\overline{\overline{E}}' + \overline{\overline{Q}}')\right\} \overline{\overline{D}}(-d) \end{bmatrix} \\ &\qquad \begin{bmatrix} \left\{(\overline{\overline{E}}' - \overline{\overline{Q}}') - (\overline{\overline{R}}_{10}^{\,c} + \overline{\overline{R}}_{10}^{\,m\alpha} \cdot \overline{a}) \cdot (\overline{\overline{E}} - \overline{\overline{Q}})\right\} \overline{\overline{D}}(-d) \\ (\overline{\overline{E}} - \overline{\overline{Q}}) - (\overline{\overline{R}}_{12}^{\,c} + \overline{\overline{R}}_{12}^{\,m\alpha} \cdot \overline{a}) \cdot (\overline{\overline{E}}' - \overline{\overline{Q}}') \end{bmatrix} \cdot \begin{bmatrix} \overline{x} \\ \overline{y} \end{bmatrix} \\ &\qquad\qquad = \begin{bmatrix} (\overline{\overline{T}}_{01}^{\,c} \cdot \overline{\delta} + \overline{\overline{T}}_{01}^{\,m\alpha}) \cdot \overline{I}_{0i}^{m\alpha} \\ 0 \end{bmatrix}\end{aligned} \tag{3.24}$$

Once these equations are solved, we can insert the obtained $\overline{x}$ and $\overline{y}$ into

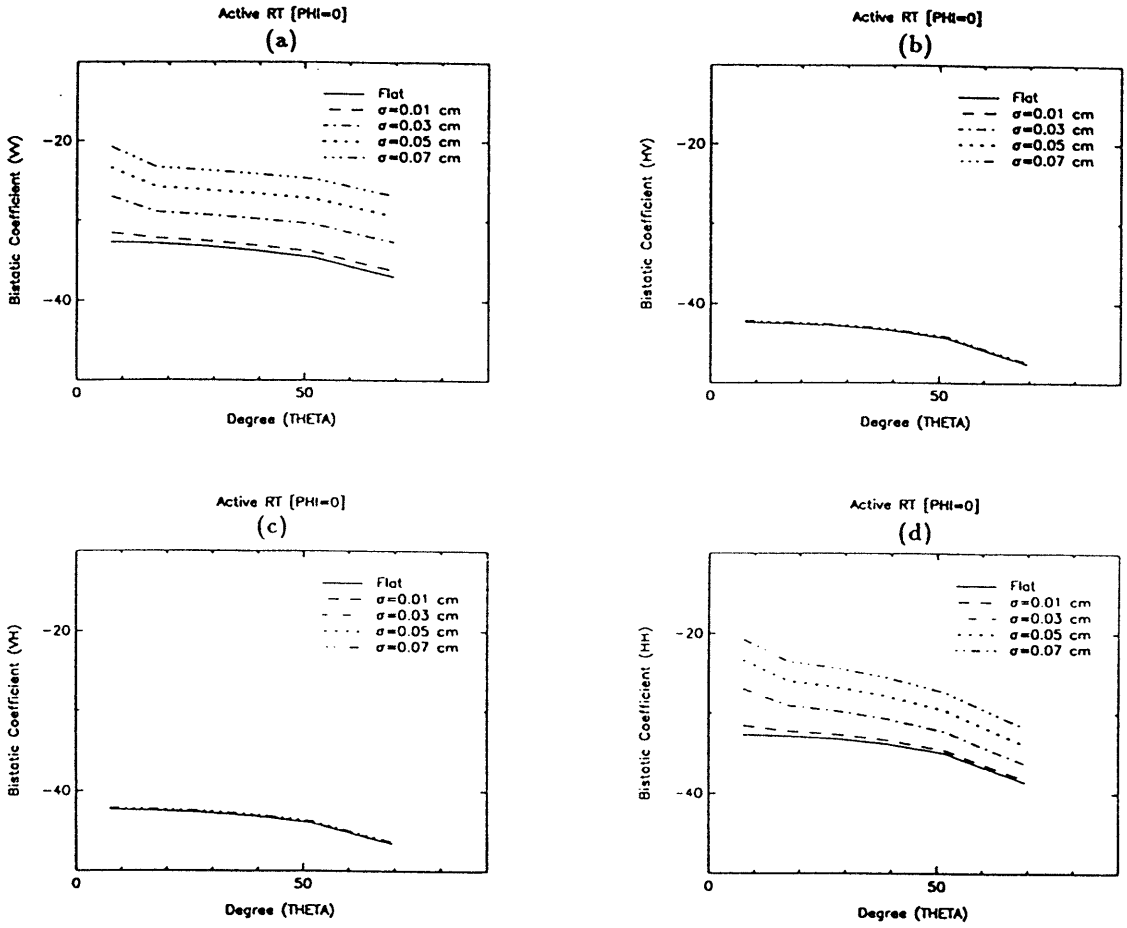

Figure 3.2: Bistatic scattering coefficients are plotted against scattered angle ϕ_s for different elevation angles (θ). The incident angle θ_i is the same as the scattered angle θ_s.

(2.118). The scattered Stokes vector in region 0 is then

$$\overline{I}_{0s} = (\overline{\overline{T}}^{c}_{10} + \overline{\overline{T}}^{m\alpha}_{10} \cdot \overline{\overline{a}}) \cdot \overline{I}^{+}(z=0) + (\overline{\overline{R}}^{c}_{01} \cdot \overline{\overline{\delta}} + \overline{\overline{R}}^{m\alpha}_{01}) \cdot \overline{I}_{0i} \qquad (3.25)$$

The final solution can be obtained by reconstructing the Fourier series for the odd and even modes.

3.4 Theoretical Results and Discussion

The contribution of rough surface scattering effects to the total bistatic scattering returns is examined in this section. Numerical calculations are carried out for a two layer medium with varying scales of roughness. The background permittivity is again chosen to be $(3.15 + i0.0017)\epsilon_0$ and the permittivity in region 2 is $(63.4 + i39.1)\epsilon_0$. Randomly orientated ellipsoid scatterers with dimensions a=0.1 cm, b=0.015 cm, c=0.05 cm are embedded in region 1. The permittivity of the scatterers is $(46.4 + i45.5)\epsilon_0$ and their fractional volume is 4.5%. The thickness of region 1 is 7.5 cm and the frequency is 5.0 GHz. Interfaces with different scales of roughness (σ= 0.01 cm, 0.03 cm, 0.05 cm and 0.07 cm, l=0.8 cm) are chosen and the numerical results of these cases are then compared with that of the planar interface.

The co-polarized (VV and HH) and cross-polarized (HV) returns are plotted as a function of the elevation angle (θ) in Figures 3.2, 3.3 and 3.4 for $\phi = 0^o, 90^o, 180^o$. The incident elevation angle (θ_s) is kept the same as the scattered elevation angle (θ_s). Generally, as we can see from parts (a) and (d) of Figures 3.2 and 3.4, the co-polarized returns (VV and HH) are higher for the rough surface case due to the rough surface scattering. On the other hand, the cross-polarized returns are not affected by the change in the roughness of the surface. This is partly due to the fact that only the first-order SPM solution is implemented and the second-order SPM solution which gives cross-polarized returns in the backscattering direction is not implemented. This is clearly shown in parts (c) of Figures 3.2 and 3.4.

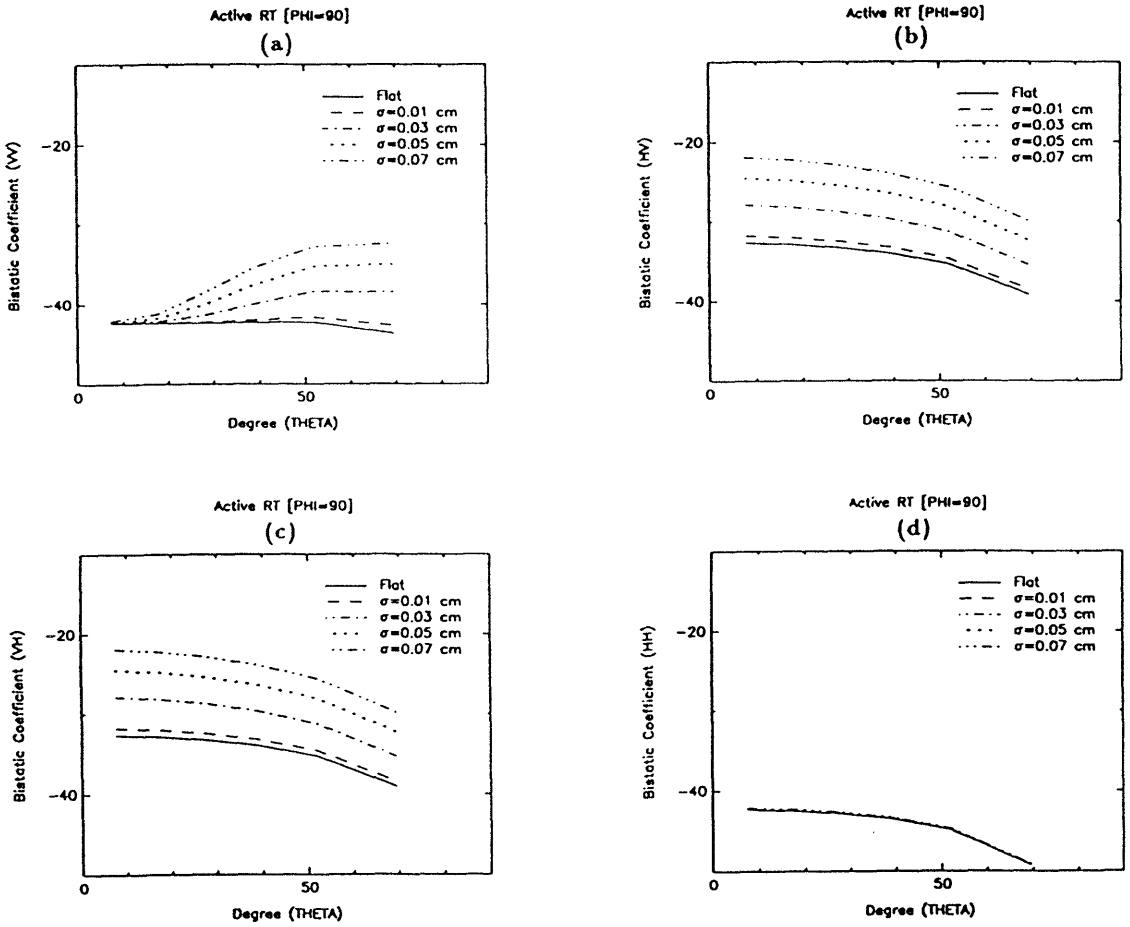

Figure 3.3: Bistatic scattering coefficients are plotted against scattered angle ϕ_s for different elevation angles (θ). The looking azimuthal angle is 90°.

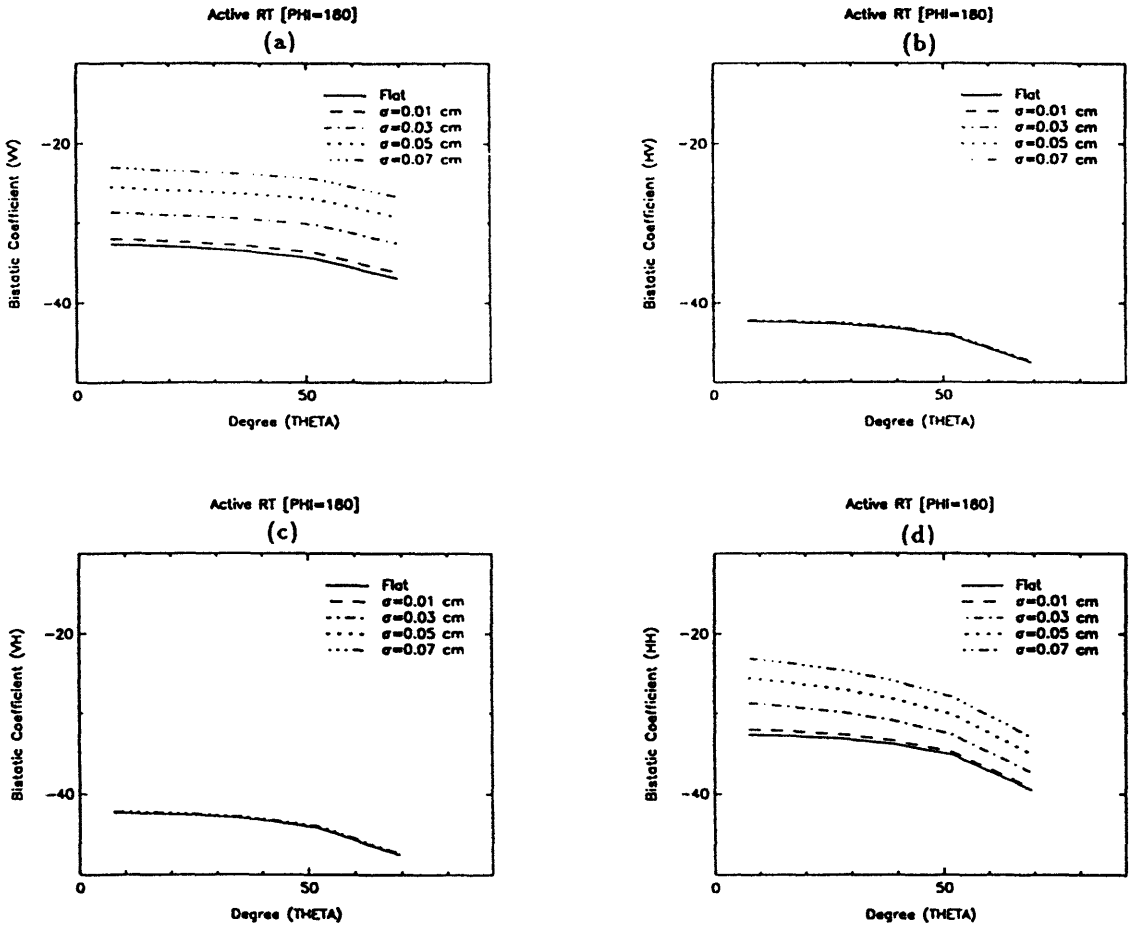

Figure 3.4: Bistatic scattering coefficients are plotted against scattered angle ϕ_s for different elevation angles (θ). The looking azimuthal angle is 180°.

If the observing angle is changed to $\phi = 90^o$, the curve forms for co-polarized and cross-polarized returns are interchanged (Figure 3.3). For the VV and HH case, when θ is large, the effective propagation path for returns in region 1 is longer. Therefore, the attenuation is higher for large θ, which means that the scattered return is lower for large θ. The curves for HH with different roughness are almost the same because the rough surface effects are not seen when the dipole axis of the receiver is perpendicular to the scattered field at all θ. However, for the VV case, as we increase the angle θ, the dipole axis of the receiver becomes more aligned with the scattered $\overline{E}$ field, and brings the returns up. For the flat surface case, this effect will bring up the curve at large θ and thus show a rather flat line. At the same time, we see the effect of rough surface scattering because the increase in the roughness of the interfaces will make the transmitted incoherent part of the intensity dominant and thus enhance the multiple scattering effects. This will increase the scattered returns proportional to the scale of the roughness.

The effects of rough surface scattering are also demonstrated in Figure 3.5 where the bistatic coefficient is plotted against the azimuthal angle ϕ for $\theta = 7.5^o$. It is clear that when the receiver dipole is perpendicular to the scattered field (for VV, HH, $\phi = 90^o$; for HV, VH, $\phi = 0^o, 180^o$), the returns are not affected by the scale of the roughness of the interfaces. However, when there is an alignment between the receiver dipole and the scattered field (for VV, HH, $\phi = 0^o, 180^o$; for HV, VH, $\phi = 90^o$), the rough surface scattering effects are not to be neglected.

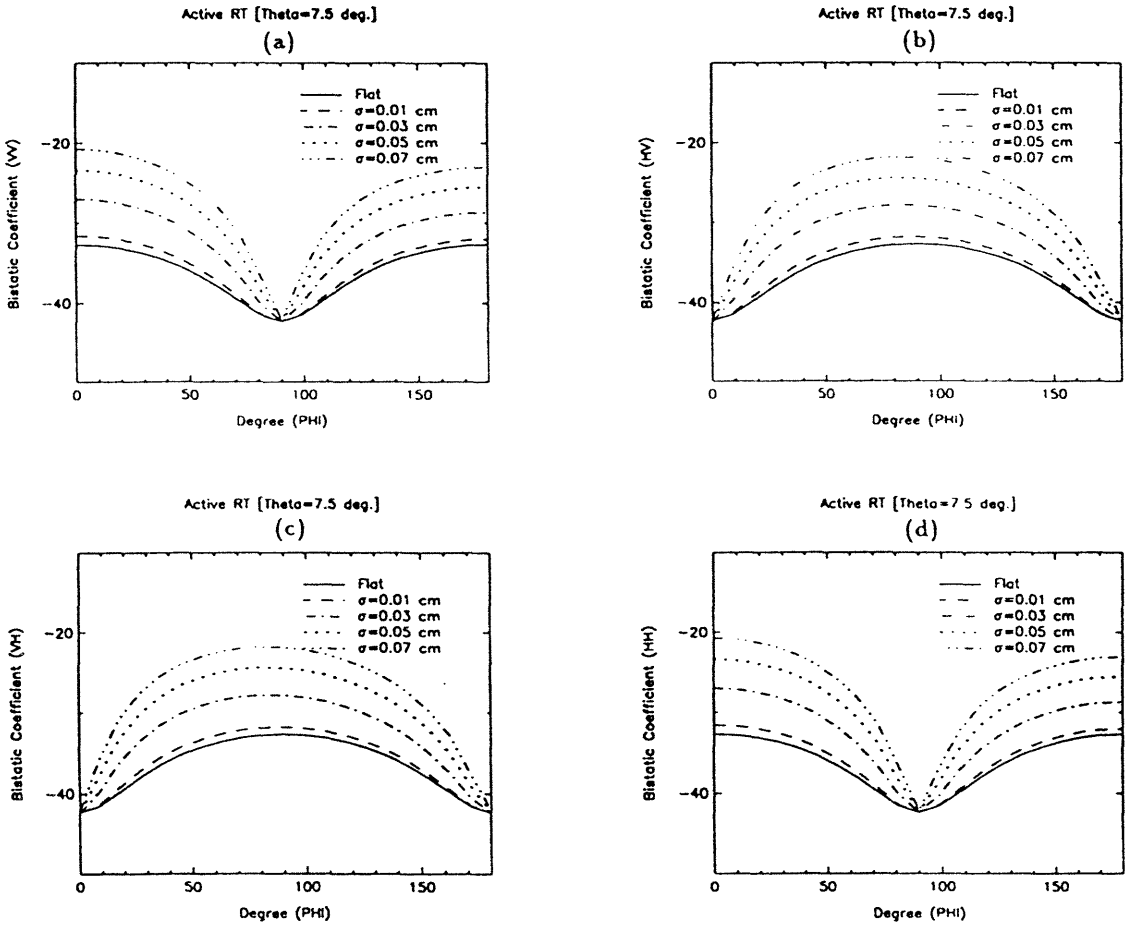

Figure 3.5: Bistatic scattering coefficients are plotted against the azimuthal angles. $\theta_i = \theta_s = 7.5°$.

3.5 Summary

In this chapter, rough interfaces were incorporated into the two layer random medium model. The rough surface scattering effects were taken into account by modifying the boundary conditions. The small perturbation method (SPM) was used to calculate the rough surface reflection and transmission matrices. The same numerical procedures presented in Chapter 2 were applied with slight differences as elaborated in the formulation section of this chapter. Basically, adding the rough interfaces into the model will makes it more similar to the actual physical sea ice layer. The study of this new configuration of the model enables us to examine the scattering effects that the rough surfaces add to the bistatic scattered returns. The numerical results presented showed that the additional scattered returns due to the rough surface scattering are generally proportional to the scale of roughness of the interfaces. This demonstrates the fact that for a real physical sea ice layer, the actual scattered polarimetric returns are dependent on a large number of factors.

Chapter 4

Theoretical Model for a Multilayer Random Medium

4.1 Configuration

In this chapter, the theoretical model in Chapter 3 is extended to a multilayer structure with rough interfaces. The background permittivity for each region is assumed to be the same and each region contains ellipsoidal scatterers with different sizes, shapes, orientations, permittivities and fractional volume. This configuration can be used to model sea ice more accurately since real sea ice has a layered structure and the fractional volume and orientation of the brine inclusions and air bubbles depends greatly on the type of ice and their distance from the air-ice interface. Figure 4.1 shows the configuration for the multilayer random medium.

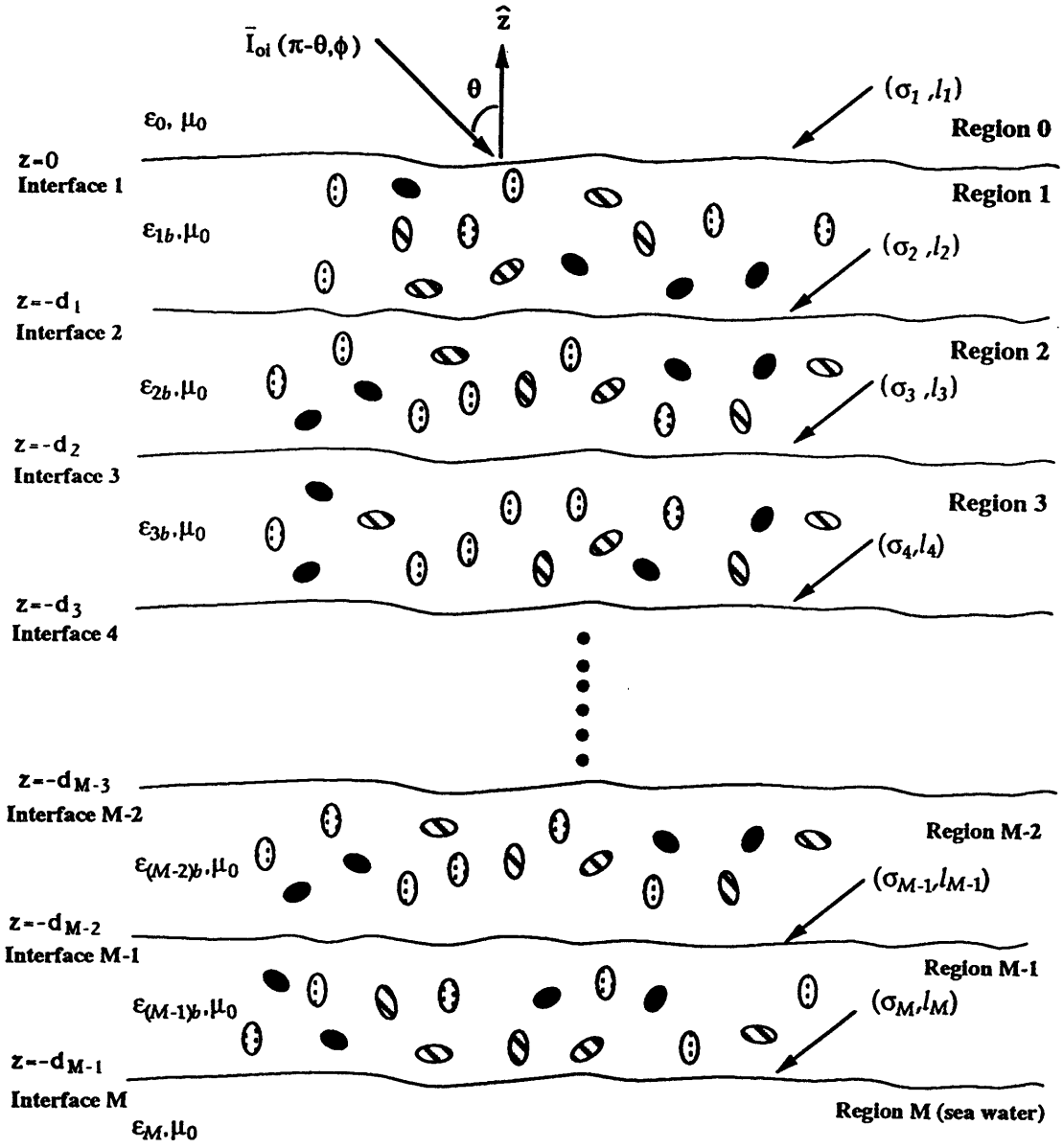

Figure 4.1: Configuration for the multilayer random medium with random rough interfaces and discrete ellipsoidal scatterers.

4.2 Radiative Transfer Equations and Boundary Conditions

Radiative transfer equations are again used and the generalized form for multilayer model (region 1 to M-1) is:

$$\begin{aligned}\cos\theta \frac{d}{dz}\bar{I}_n(\theta,\phi,z) &= -\bar{\bar{\kappa}}_{en}(\theta,\phi)\cdot\bar{I}_n(\theta,\phi,z) \\ &\quad + \int_{4\pi} d\Omega' \bar{\bar{P}}_n(\theta,\phi;\theta',\phi')\cdot\bar{I}_n(\theta',\phi',z) \qquad (4.1)\end{aligned}$$

where $\bar{I}_n$, $\bar{\bar{P}}_n$ and $\bar{\bar{\kappa}}_{en}$ are the Stokes vector, phase matrix and extinction matrix inside layer n, respectively.

The boundary conditions are also generalized and have the following form

Interface n:

$$\begin{aligned}\bar{I}_n(\pi-\theta,\phi,z=-d_{n-1}) &= \bar{\bar{R}}^{\,c}_{n,n-1}(\theta,\phi)\cdot\bar{I}_n(\theta,\phi,z=-d_{n-1}) \\ &+ \int_0^{2\pi} d\phi' \int_0^{\frac{\pi}{2}} d\theta' \sin\theta' \,\bar{\bar{R}}^{\,i}_{n,n-1}(\theta,\phi;\theta',\phi') \\ &\quad \cdot\bar{I}_n(\theta',\phi',z=-d_{n-1}) \\ &+ \bar{\bar{T}}^{\,c}_{n-1,n}(\theta_{n-1},\phi_{n-1})\cdot\bar{I}_{n-1}(\pi-\theta_{n-1},\phi_{n-1},z=-d_{n-1}) \\ &+ \int_0^{2\pi} d\phi'_{n-1} \int_0^{\frac{\pi}{2}} d\theta'_{n-1} \sin\theta'_{n-1} \,\bar{\bar{T}}^{\,i}_{n-1,n}(\theta,\phi;\theta'_{n-1},\phi'_{n-1}) \\ &\quad \cdot\bar{I}_{n-1}(\pi-\theta'_{n-1},\phi'_{n-1},z=-d_{n-1}) \qquad (4.2)\end{aligned}$$

Interface n+1 :

$$\begin{aligned}
\overline{I}_n(\theta,\phi,z=-d_n) &= \overline{\overline{R}}^{\,c}_{n,n+1}(\theta,\phi)\cdot\overline{I}_n(\pi-\theta,\phi,z=-d_n) \\
&+ \int_0^{2\pi} d\phi' \int_0^{\frac{\pi}{2}} d\theta' \sin\theta' \; \overline{\overline{R}}^{\,i}_{n,n+1}(\theta,\phi;\theta',\phi') \\
&\cdot\overline{I}_n(\pi-\theta',\phi',z=-d_n) \\
&+ \overline{\overline{T}}^{\,c}_{n+1,n}(\theta_{n+1},\phi_{n+1})\cdot\overline{I}_{n+1}(\theta_{n+1},\phi_{n+1},z=-d_n) \\
&+ \int_0^{2\pi} d\phi'_{n+1} \int_0^{\frac{\pi}{2}} d\theta'_{n+1} \sin\theta'_{n+1} \; \overline{\overline{T}}^{\,i}_{n+1,n}(\theta,\phi;\theta'_{n+1},\phi'_{n+1}) \\
&\cdot\overline{I}_{n+1}(\theta'_{n+1},\phi'_{n+1},z=-d_n) \qquad (4.3)
\end{aligned}$$

where $n = 2,3,\ldots,M$-2 and θ_{n-1} and θ_{n+1} are the elevation angles in the local coordinate system of layers n-1 and n+1, respectively, and are related to θ by Snell's law.

If the background permittivities of regions 1 to $M-1$ are the same, then we can simplify the above boundary conditions to

Interface n:

$$\overline{I}_n(\pi-\theta,\phi,z=-d_{n-1}) = \overline{I}_{n-1}(\pi-\theta_{n-1},\phi_{n-1},z=-d_{n-1}) \qquad (4.4)$$

Interface n+1 :

$$\overline{I}_n(\theta,\phi,z=-d_n) = \overline{I}_{n+1}(\theta_{n+1},\phi_{n+1},z=-d_n) \qquad (4.5)$$

For interface 1, we have to take into account the incident wave $\overline{I}_{oi}$. Thus, the boundary condition has the form:

$$\begin{aligned}\overline{I}_1(\pi-\theta,\phi,z=0) &= \overline{\overline{R}}^{\,c}_{10}(\theta,\phi)\cdot\overline{I}_1(\theta,\phi,z=0)\\ &+ \int_0^{2\pi}d\phi'\int_0^{\frac{\pi}{2}}d\theta'\sin\theta'\;\overline{\overline{R}}^{\,i}_{10}(\theta,\phi;\theta',\phi')\\ &\cdot\overline{I}_1(\theta',\phi',z=0)\\ &+ \overline{\overline{T}}^{\,c}_{01}(\theta_0,\phi_0)\cdot\overline{I}_{0i}(\pi-\theta_0,\phi_0)\\ &+ \overline{\overline{T}}^{\,i}_{01}(\theta,\phi;\theta_{0i},\phi_{0i})\cdot\overline{I}_{0i} \qquad (4.6)\end{aligned}$$

and for interface M, the boundary condition is:

$$\begin{aligned}\overline{I}_{M-1}(\theta,\phi,z=-d_{M-1}) &= \overline{\overline{R}}^{\,c}_{M-1,M}(\theta,\phi)\cdot\overline{I}_{M-1}(\pi-\theta,\phi,z=-d_{M-1})\\ &+ \int_0^{2\pi}d\phi'\int_0^{\frac{\pi}{2}}d\theta'\sin\theta'\;\overline{\overline{R}}^{\,i}_{M-1,M}(\theta,\phi;\theta',\phi')\\ &\cdot\overline{I}_{M-1}(\pi-\theta',\phi',z=-d_{M-1}) \qquad (4.7)\end{aligned}$$

where again θ_0 is related to θ by Snell's law.

The incident wave in region 0 is

$$\overline{I}_{0i}(\pi-\theta_0,\phi_0)=\overline{I}_{0i}\cdot\delta(\cos\theta_0-\cos\theta_{0i})\cdot\delta(\phi_0-\phi_{0i}) \qquad (4.8)$$

Finally, the following boundary condition can be applied to solve for the scat-

tered waves in region 0:

$$\begin{aligned}
\bar{I}_{0s}(\theta_0,\phi_0) &= \bar{\bar{R}}^{c}_{01}(\theta_0,\phi_0)\cdot\bar{I}_{0i}(\pi-\theta_0,\phi_0) \\
&+ \bar{\bar{R}}^{i}_{01}(\theta_0,\phi_0;\theta_{0i},\phi_{0i})\cdot\bar{I}_{0i} \\
&+ \bar{\bar{T}}^{c}_{10}(\theta,\phi)\cdot\bar{I}_1(\theta,\phi,z=0) \\
&+ \int_0^{2\pi}d\phi'\int_0^{\frac{\pi}{2}}d\theta'\sin\theta'\,\bar{\bar{T}}^{i}_{10}(\theta_0,\phi_0 q;\theta',\phi')\cdot\bar{I}_1(\theta',\phi',z=0) \quad (4.9)
\end{aligned}$$

4.3 Numerical Solution

Using the same numerical method described in Chapters 2 and 3, we can solve for the upgoing and downgoing intensities for each bounded layer by matching the boundary conditions at M interfaces simultaneously. However, this involves too many unknowns, and a large memory size is required for numerical calculations. However, the concept of effective boundary conditions can be used to simplify the whole computation process. Consider only regions M, $M-1$ and $M-2$, we can apply the numerical techniques for two-layer medium case to calculate for the upgoing intensities in region $M-2$. Then the effective boundary condition at interface $M-1$ can be expressed as

$$\bar{I}^{+}_{M-2} = \bar{\bar{R}}^{eff}_{M-2(M-1)}\cdot\bar{I}^{-}_{M-2} \quad (4.10)$$

where the effective reflection matrix $\bar{\bar{R}}^{eff}_{M-2(M-1)}$ contains all the information for regions $M-1$ and M. Next, we will consider regions $M-1$, $M-2$ and $M-3$ as

the new two layer medium problem and $\overline{\overline{R}}^{eff}_{M-2(M-1)}$ will be the reflection matrix at interface $M-1$. A new effective reflection matrix can then be computed, and the whole process can be repeated until we reach the top two layers. This procedure is carried out for each harmonic (m=0,1,2,...) and each mode (even e and odd o). The final scattered Stokes vector can be found from equation (4.9). This approach simplifies the computation process by enabling us to deal with two layer problem at a time. Note that, at interface M, $\overline{\overline{R}}^{eff}_{M-1(M)} = \overline{\overline{R}}_{M-1(M)}$.

4.4 Theoretical Results and Discussion

Numerical calculations are carried out for a multilayer structure in this section. The parameters were chosen to represent a real physical ice layer. The temperature profile of a grown ice sheet was from the measurement data taken during CRRELEX93 [72]. Since the permittivity of brine inclusions is temperature dependent, we can obtain the corresponding permittivity of brine inclusions for each layer using the Debye type relaxation equation [27],[28]:

$$\epsilon_{brine} = \epsilon_\infty + \frac{\epsilon_s - \epsilon_\infty}{1 - i2\pi f\tau} + i\frac{\sigma}{2\pi\epsilon_0 f} \tag{4.11}$$

where ϵ_s and ϵ_∞ are the limiting static and high frequency values of the real part of ϵ_{brine}, f is the frequency, τ the relaxation time, σ the ionic conductivity of the dissolved salts and ϵ_0 the permittivity of free space. ϵ_s, ϵ_∞, τ and σ are all related to the temperature [27]. A five layer medium is constructed with different thickness and permittivity of brine inclusions. From top to bottom, the parameters

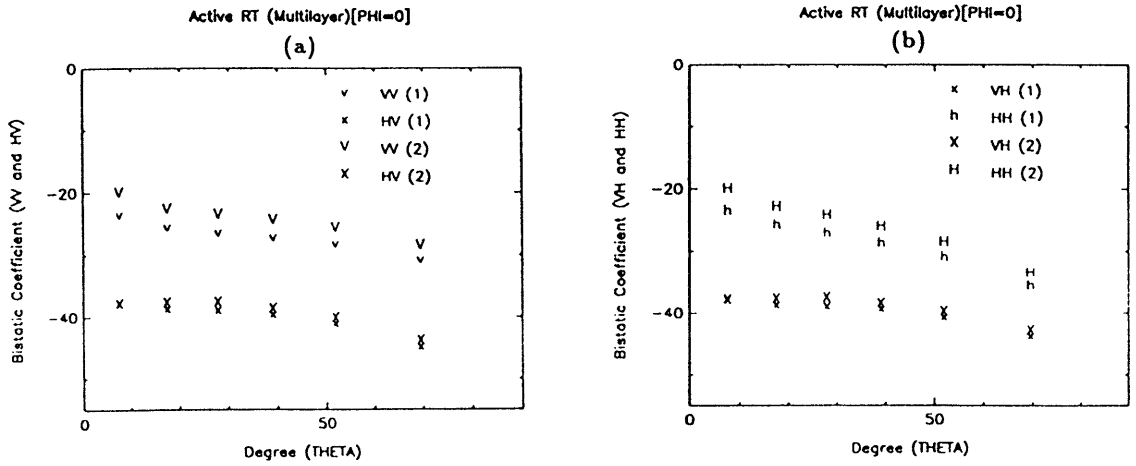

Figure 4.2: Bistatic scattering coefficients are plotted against different angle θ ($\theta_i = \theta_s$) for ϕ= 0°.

are (thickness = 1 cm, ϵ_{brine} = 50.28 + i44.80), (2 cm, 52.52 + i44.04), (2 cm, 54.98 + i42.98), (3 cm, 57.70 + i41.57), (7 cm, 60.76 + i39.79). The background permittivity for each layer is kept the same (ϵ_b = 3.15+i0.0017) and the permittivity of sea water is (63.4 + i39.1). The dimensions of the ellipsoids embedded in the background medium are a=0.1 cm, b=0.015 cm and c=0.050 cm. Fractional volume of scatterers for each layer is 4.5%. For the top layer, the ellipsoidal scatterers are chosen to be randomly oriented, whereas for all the other layers, the scatterers are vertically oriented. This is to model the orientation of the scatterers correctly as described in Chapter 2. A slightly rough air-ice interface (σ=0.048 cm, l=0.669 cm) and ice-seawater interface (σ=0.048 cm, l=1.600 cm) are chosen. The frequency used is 5 GHz. This case will be referred as Case 1.

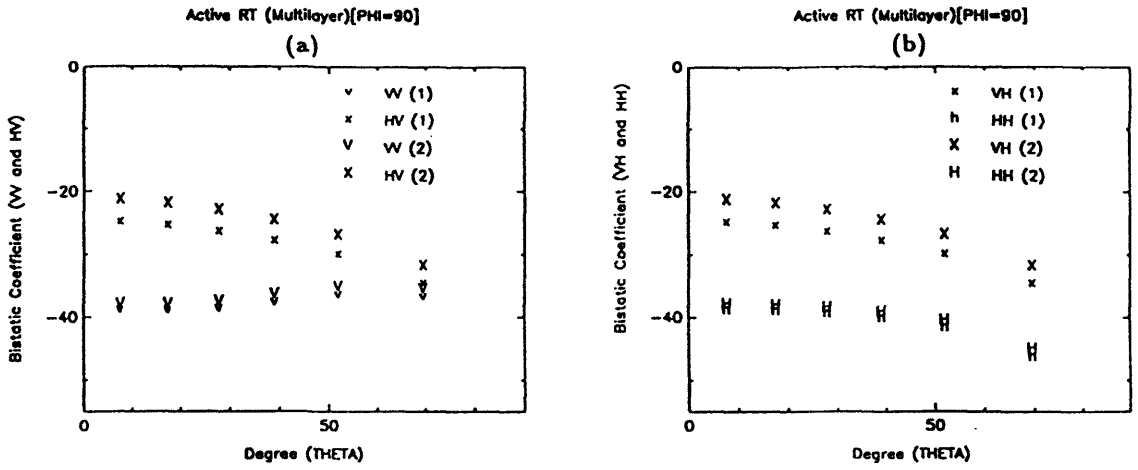

Figure 4.3: Bistatic scattering coefficients are plotted against different angle θ ($\theta_i = \theta_s$) for ϕ= 90°.

As mentioned in Chapter 1, brine drainage occurs in multiyear sea ice, which leaves air bubbles where the brine inclusions were. Normally, close to the ice-seawater interface, there are still brine inclusions left. Therefore, for Case 2, instead of having brine inclusions for the top three layers, we substitute them with air bubbles of the same size, dimension, orientation and fractional volume. The purpose is to investigate the difference in the bistatic scattering coefficients for Case 1 and Case 2.

Figures 4.2, 4.3 and 4.4 show the comparison of the numerical results for both cases. Generally, for all ϕ, scattering returns for Case 2 (air bubbles) are higher than those of Case 1 (brine inclusions). This is because brine inclusions are very lossy due to their large imaginary part of permittivity, whereas the air bubbles

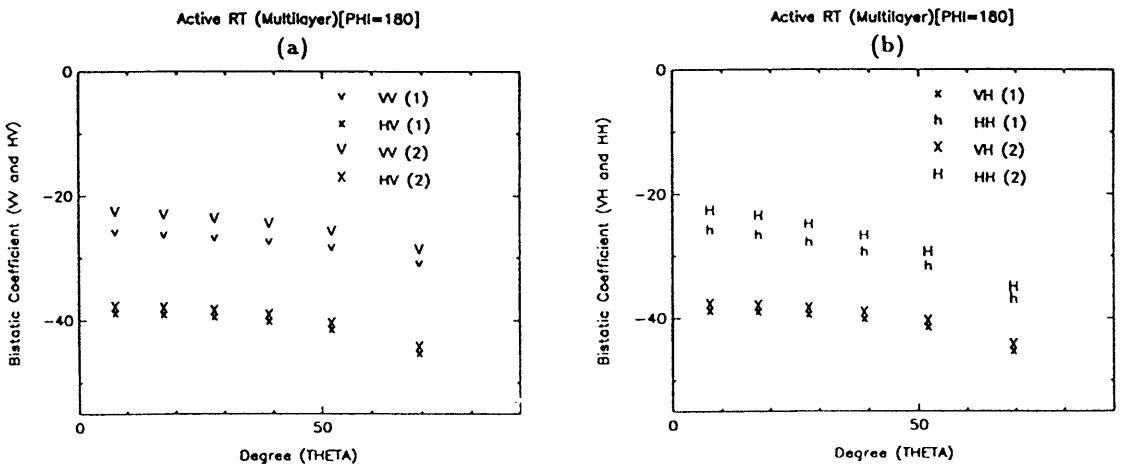

Figure 4.4: Bistatic scattering coefficients are plotted against different angle θ ($\theta_i = \theta_s$) for ϕ= 180°.

merely act as scatterers without any energy absorption. As a result, waves scatter more in Case 2 than Case 1.

4.5 Summary

In this chapter, the theoretical model for a two layer medium with rough interfaces in Chapter 3 has been extended to a multilayer structure. The discrete eigenanalysis method was again used to perform the computation. The effective boundary condition concept was introduced and implemented, thus enabling us to solve the linear algebra equations one layer at a time. Two cases of multilayer structure have been constructed. The comparison of the numerical results reveals that the model which has mostly air bubbles embedded within the layers generally shows higher

bistatic scattering coefficients than the one which has brine inclusions instead.

Chapter 5

Passive Microwave Remote Sensing of Sea Ice

5.1 Introduction

Passive remote sensing of sea ice has been investigated for more than two decades and a great amount of measurement data has been collected. By carefully studying the radiometric signatures, researchers have been able to identify the three dominant surfaces in the Arctic, which are open water, first-year ice and multiyear ice [68]. Although the collection of measured scattering data from sea ice provides great information about the scattering mechanisms and physical properties of sea ice, this knowledge can be further enhanced by studying the passive radiometric signatures of sea ice.

In general, the sensors can be characterized into three classes. For small spatial scales, surface-based sensors are used. This enables the study of local variability of electromagnetic returns. The advantages of this method are that ground truth can be easily collected on the spot and measurements can be repeated for different

looking angles and different weather conditions. Measuring on a small spatial scale will also reduce the heterogeneity of the electromagnetic returns. As a result, correct interpretation of the measured data is much easier.

Features such as ridges, hummocks, melt ponds and floes can be captured by using the aircraft-based sensors which provides images with resolution of 10 to 100 m. Regional variability in the electromagnetic returns can be applied to the classification of wide areas of sea ice. Different frequencies are also used to reveal more of the texture of various surfaces.

The capability to monitor the entire polar ice region on a daily basis makes the satellite-based sensors popular. Measurements can be carried out regardless of the time or the cloudiness. A spatial resolution of 15 to 30 km gives a good estimate of the change and total size of ice extent. The measured data can also be fed into global climate prediction models.

5.2 Configuration and Formulation

The theoretical model shown in Figure 2.1 is used to calculate the emissivity. Subsequently, rough interfaces is added and followed by extension of this model to a multilayer sea ice model. There are generally two approaches to solve the passive problem. The first one is by directly solving the radiative transfer equation shown below:

$$\cos\theta \frac{d}{dz}\overline{I}(\theta,\phi,z) = -\overline{\overline{\kappa}}_e(\theta,\phi)\cdot\overline{I}(\theta,\phi,z)+\overline{\overline{\kappa}}_a C_1 T_1 + \int_{4\pi} d\Omega' \quad \overline{\overline{P}}(\theta,\phi;\theta',\phi')\cdot\overline{I}(\theta',\phi',z) \tag{5.1}$$

where κ_a denotes the emission coefficient, $C_1 = K\epsilon_1'/\epsilon_0\lambda^2$, K is the Boltzmann's constant and T_1 is the physical temperature in Region 1. The second term on the right hand side of equation (5.1) is not omitted as in the case for active calculations because the contribution of this term in the absence of incident waves is no longer negligible.

On the other hand, a second approach is to make use of the solution to the active calculations done in the previous chapters. The bistatic scattering coefficients $\gamma_{\beta\alpha}(\theta_{os}, \phi_{os}; \theta_{oi}, \phi_{oi})$ for different scattered angles and polarizations are first calculated and then added up for a particular incident polarized wave (α) at an incident angle (θ_{oi}), and the emissivity is given by [57]

$$e_\alpha(\theta_{oi}) = 1 - r_{01}^c(\theta_{oi}) - \Sigma_\beta \frac{1}{4\pi} \int_0^{\frac{\pi}{2}} d\theta_{os} \sin\theta_{os} \int_0^{2\pi} d\phi_{os}\ \gamma_{\beta\alpha}(\theta_{os}, \phi_{os}; \theta_{oi}, \phi_{oi}) \quad (5.2)$$

where $r_{01}^c(\theta_{oi})$ is the coherent reflected term in the specular direction. The computed emissivity is further related to the brightness temperature $T_{\alpha B}(\theta, \phi)$ by:

$$T_{\alpha B}(\theta, \phi) = e_\alpha(\theta_{oi})T \quad (5.3)$$

where T is the physical temperature of the medium, and it is assumed that there is no radiation from the sky.

5.3 Theoretical Results and Discussion

Figure 5.1 (a) shows the numerical results for two layer medium with flat interfaces. The brightness temperature is plotted as a function of looking angle θ.

The background permittivity of the bounded region is $(1.5 + i0.0015)\epsilon_0$ and the bottom half space has a permittivity of $(6.0)\epsilon_0$. The dimensions of the vertically distributed spherical scatterers are $a = b = c = 0.05$ cm and their permittivity is $(3.2 + i0.0005)\epsilon_0$. A fractional volume of 5% is chosen for the scatterers. The thickness of the bounded layer is 20.0 cm and frequency used is 5 GHz. The medium has a uniform physical temperature of 265.0 K. At normal incidence, the brightness temperatures for both V and H polarized waves are the same. As we increase the angle, brightness temperature for H will fall whereas that of V will first increase before falling at angle θ_1. In fact, the pattern of these two curves are very similar to a up side down of the plot for reflectivity for TE and TM waves, with the Brewster angle effect for the TM case. The contribution of volume scattering by the scatterers to the brightness temperature can be demonstrated by comparing Figure 5.1 (a) and Figure 5.1 (b) where Figure 5.1 (b) is the same plot for two layer medium without the volume scattering effect (no scatterers).

The following section investigates the effect of the change in the permittivity of the scatterers on the brightness temperature. The background permittivity is $(3.15 + i0.0030)\epsilon_0$ and the permittivity of the bottom halfspace is $(40.0 + i30.0)\epsilon_0$. The vertically aligned scatterers have dimensions of $a = b = c = 0.05$ cm and occupy 5% of unit volume.The imaginary part of the scatterers (ϵ_s'') is kept constant at $20.0\epsilon_0$ for all the six cases and the real part (ϵ_s') is varied from $5.0\epsilon_0$ to $50.0\epsilon_0$. The thickness of the bounded layer is 5 cm. The frequency is chosen as 5 GHz and the uniform physical temperature is 265.0 K. Figure 5.2 shows the numerical results. This figure shows that increasing the real part of the permittivity of the

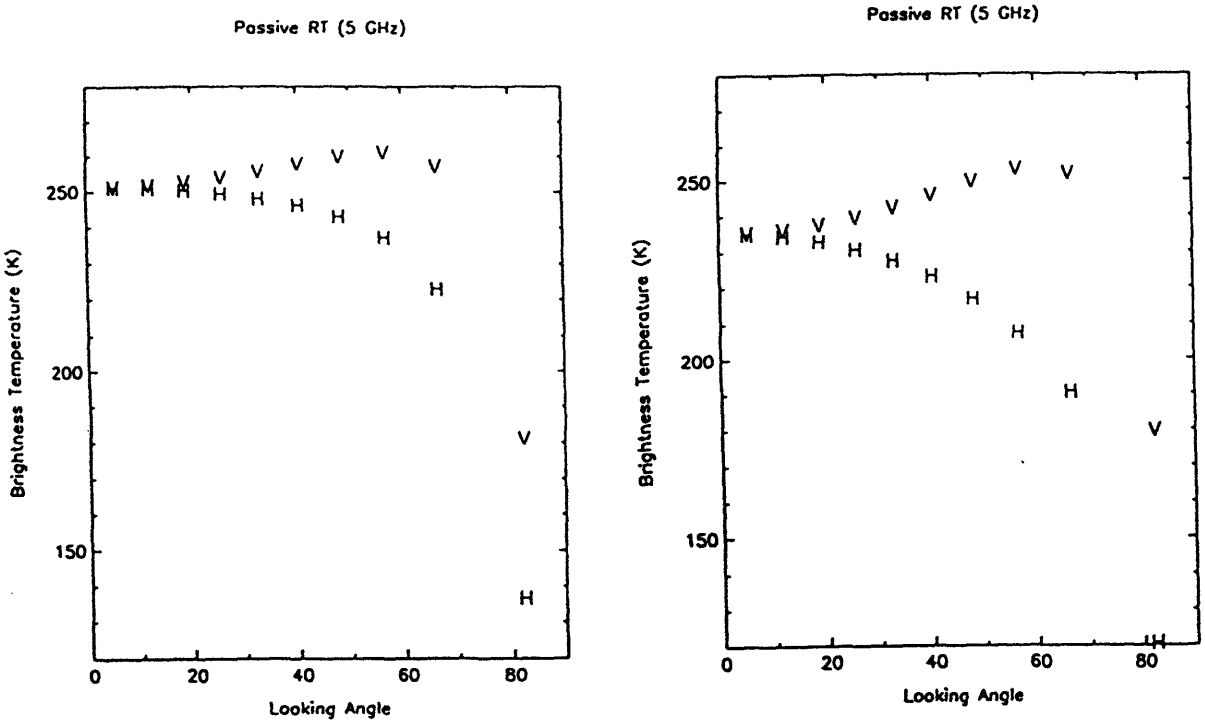

(a) (b)

Figure 5.1: Brightness temperatures are plotted as a function of looking angle θ. (a) is with scatterers. (b) is without scatterers.

scatterers lowers the brightness temperature. Higher real part of permittivity of the scatterers results in more scattering and less penetration of waves into the medium. This means less power will be absorbed. As a result, we have a higher albedo and thus a lower brightness temperature. This is true for both the V and H polarization cases.

The above calculations are repeated with the same set of parameters except for the permittivity of the scatterers. This time, the real part of ϵ_s is kept constant at $10.0\epsilon_0$ and ϵ_s'' is varied from $5.0\epsilon_0$ to $50.0\epsilon_0$. The numerical results are shown in Figure 5.3. As we increase the imaginary part of the permittivity of the scatterers, more power will be absorbed and thus the ratio of the scattering loss to the total extinction loss (low albedo) decreases. This results in the increase of brightness temperature. However, as we increase ϵ_s'' further, the brightness temperature starts to drop. This is due to the fact that scattering coefficients of Rayleigh scattering for small particles (compared to the wavelength) are proportional to the dielectric constant of the scatterers, both the real and imaginary part. Therefore, as we increase ϵ_s'' to a value comparable to ϵ_s', the scattering effect contributed by ϵ_s'' dominates over its absorption effect and the albedo increases. This then lowers the brightness temperature. Again, this is true for both the V and H polarization cases.

The effects of rough interfaces on the brightness temperature are examined by calculating the following cases for a two layer medium sea ice structure. A 4.5% fractional volume of vertically aligned ellipsoidal scatterers with dimension a=0.1 cm, b=0.015 cm and c=0.050 cm are embedded within the pure ice background ($\epsilon_b = [3.15 + i0.0017]\epsilon_0$) with the thickness of 5.0 cm. The scatterers are brine

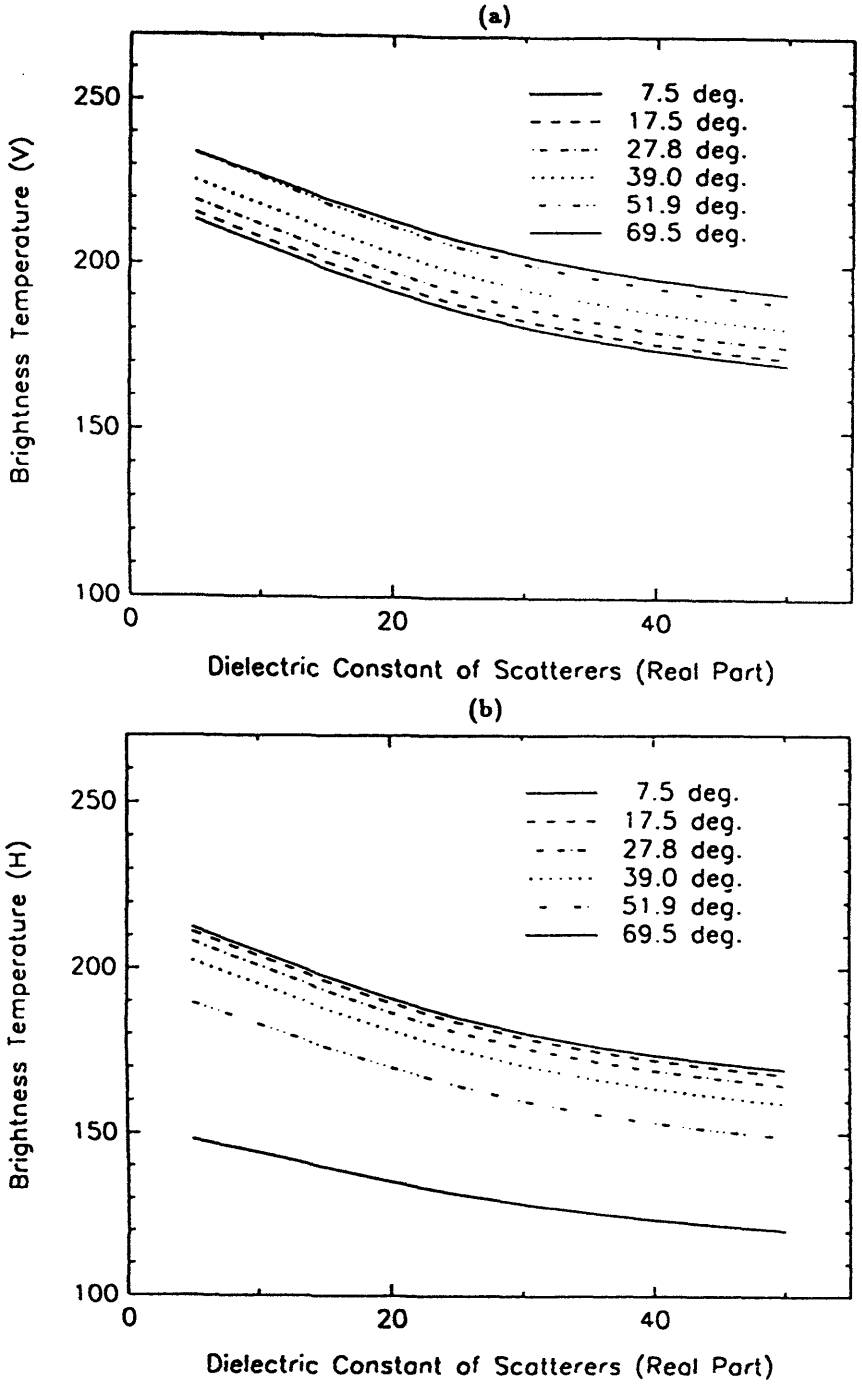

Figure 5.2: Brightness temperatures are plotted against the real part of dielectric constant of the scatterers for different looking angles. (a) is for V polarization and (b) is for H polarization.

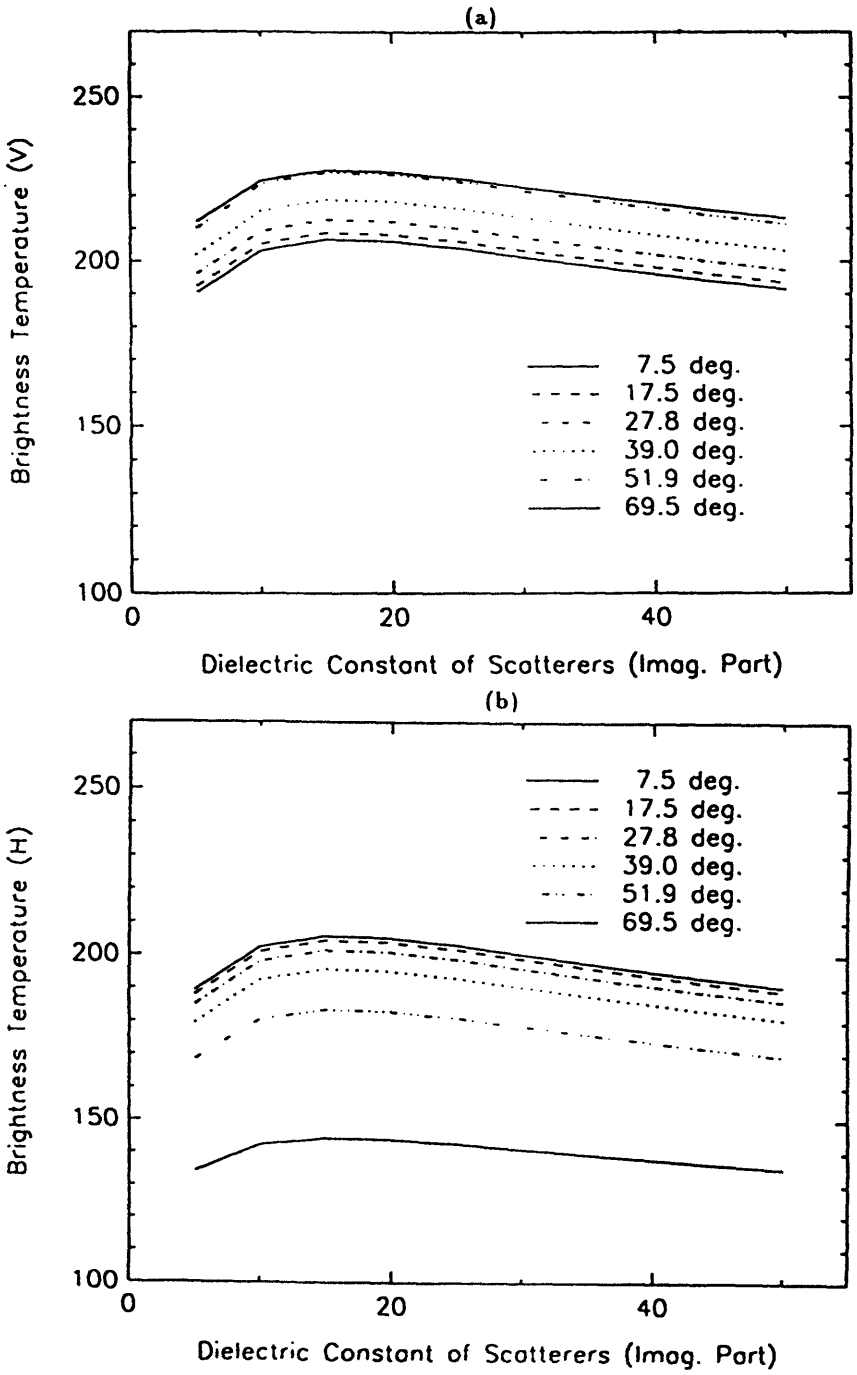

Figure 5.3: Brightness temperatures are plotted against the imaginary part of dielectric constant of the scatterers for different looking angles. (a) is for V polarization and (b) is for H polarization.

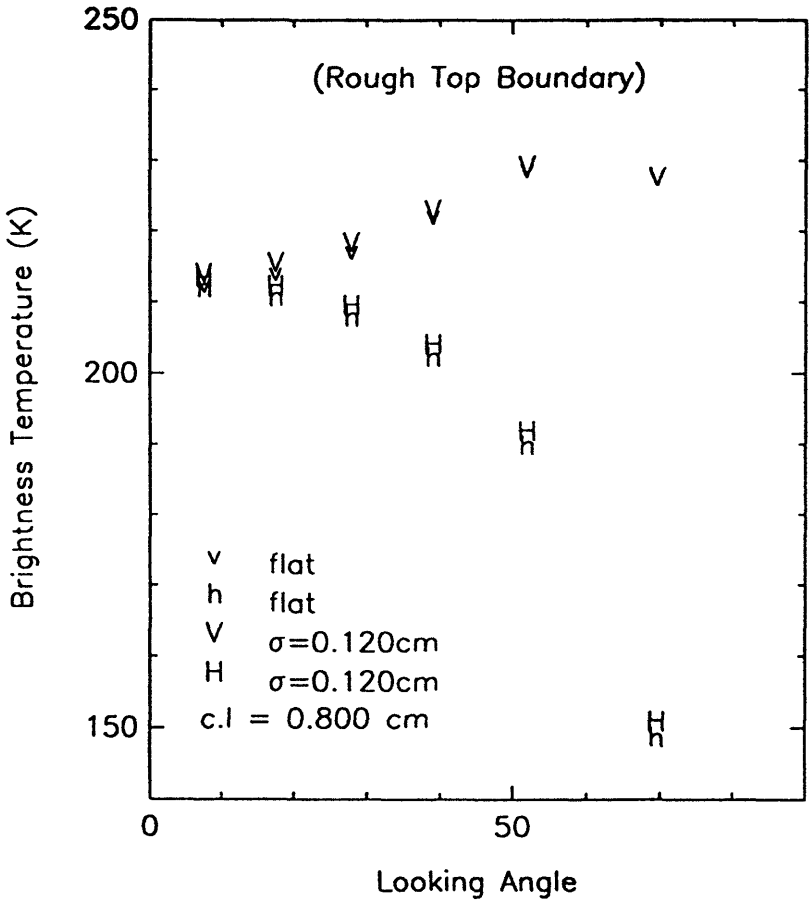

Figure 5.4: Brightness temperature as a function of looking angle for rough surface at top boundary.

inclusions with permittivity $\epsilon_s = [46.4 + i45.5]\epsilon_0$. The frequency is 5 GHz and the physical temperature is assumed to be uniform (265 K). The permittivity of the sea water in the bottom half space is $[63.4 + i39.1]\epsilon_0$ at this frequency. The three cases run are (1) only the top boundary is rough, (2) only the bottom boundary is rough and (3) both the top and bottom boundaries are rough. The roughness parameters chosen are $\sigma = 0.120$ cm and correlation length = 0.800 cm.

Figures 5.4, 5.5 and 5.6 present the numerical results computed for the three cases compared with those of the flat boundary case. The effect of the rough bound-

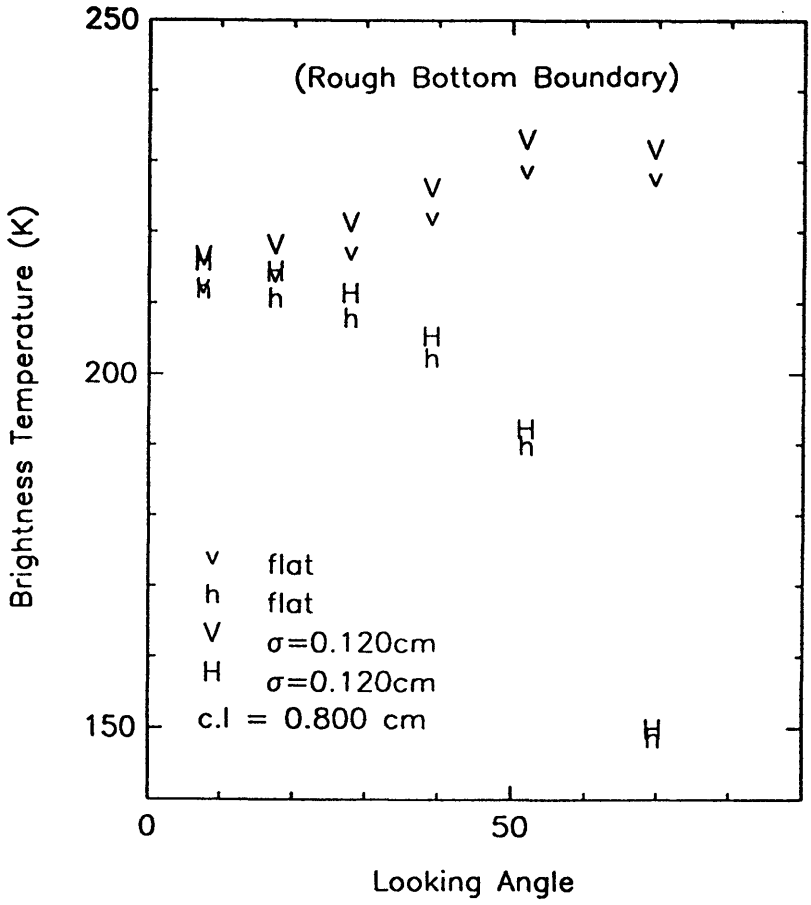

Figure 5.5: Brightness temperature as a function of looking angle for rough surface at bottom boundary.

aries is shown by plotting the brightness temperature as a function of observation angle for the vertical and horizontal polarizations. Figures 5.4 (a), (b) and (c) corresponds to Cases 1, 2 and 3 mentioned above where (v,V) representing the vertical polarization and (h,H) representing the horizontal polarization. Generally, there is an increase of brightness temperature due to the rough surface effects. Comparison of results show that the increase in the brightness temperature (T_v, T_h) is mostly due to the reflection of the bottom rough boundary which enhances the absorption effects of the scatterers and background medium.

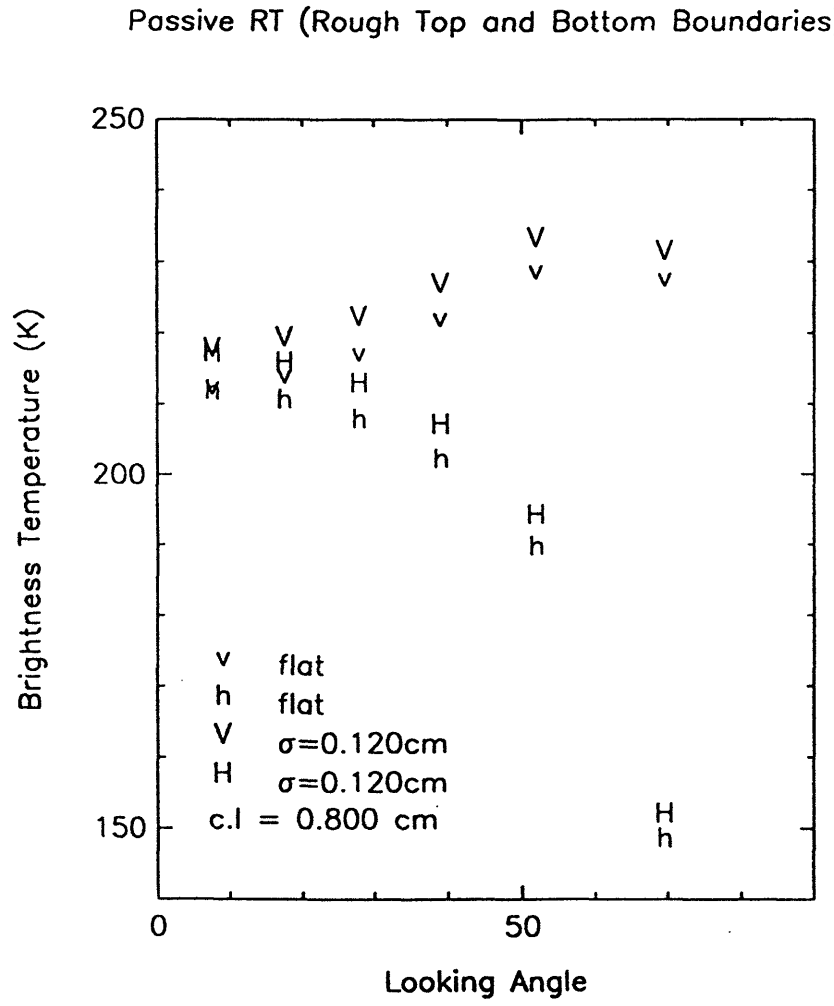

Figure 5.6: Brightness temperature as a function of looking angle for rough surfaces at top and bottom boundary.

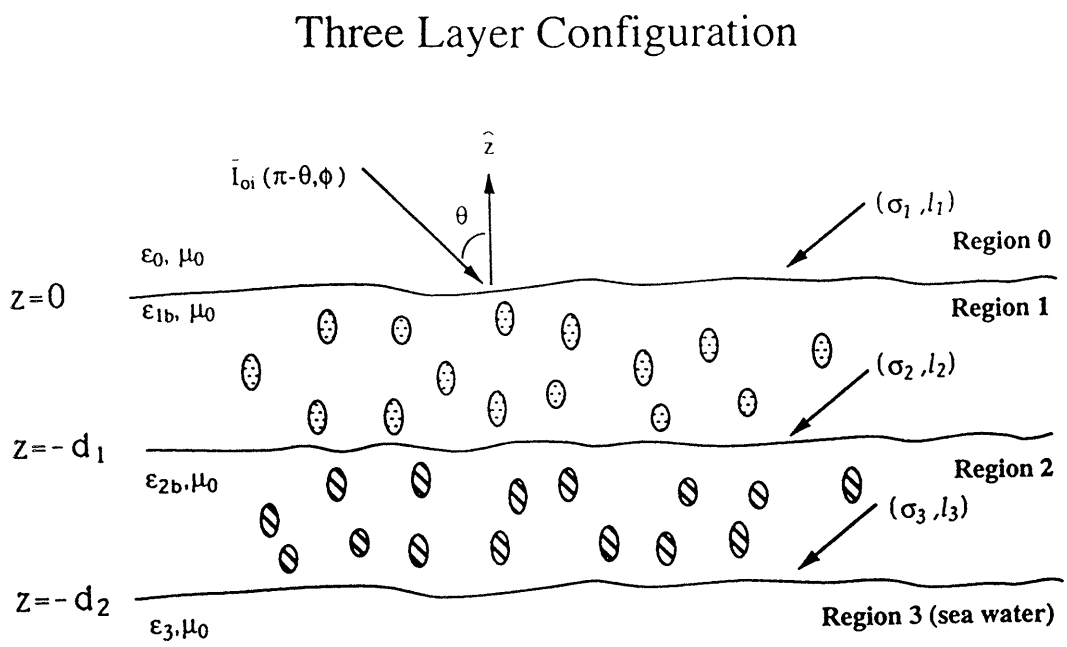

Figure 5.7: A Three Layer Configuration.

A three layer configuration is shown in Figure 5.7. The orientation, shape, dimension and fractional volume of the scatterers for regions 1 and 2 are the same as those in the previous case. The rough surface parameters are σ_1=0.048 cm, l_1=0.669 cm, σ_3=0.048 cm, l_3=1.600 cm. Since the background media in regions 1 and 2 are the same, σ_2 and l_2 can be left out as there will be total transmission and no reflection across the region 1 - region 2 interface. For Case 1, brine inclusions are assumed to be embedded in regions 1 and 2, whereas for Case 2, air bubbles will replace brine inclusions in region 1. Case 1 is modelled to represent the first year sea ice, and Case 2 represents multiyear ice. The dielectric constant of the air bubbles is the same as that of the free space and $\epsilon_s = [46.4 + i45.5]\epsilon_0$ is assumed for the brine inclusions at 5 GHz. The thickness of regions 1 and 2 is chosen as 10 cm. The results are illustrated in Figures 5.8 and 5.9. Since the air bubbles in Case 2 are not lossy and contribute only to the volume scattering effect, albedo for Case 2 should be higher than that of Case 1. Thus, brightness temperatures calculated for Case 2 should be lower than those of Case 1. This trend is clearly shown in Figures 5.8 and 5.9.

Numerical calculations for a multilayer sea ice structure were carried out to simulate the change in the brightness temperature as a function of the sea ice thickness for the frequency of 1 GHz. The fractional volume of the vertically aligned brine inclusions for each layer is obtained by assuming a parabolic salinity profile and a linear temperature profile [71]. The size of the ellipsoidal brine inclusions was kept the same for each layer. The permittivity of the brine inclusions for each layer was calculated from Debye equations [27]. The number of the layers was chosen

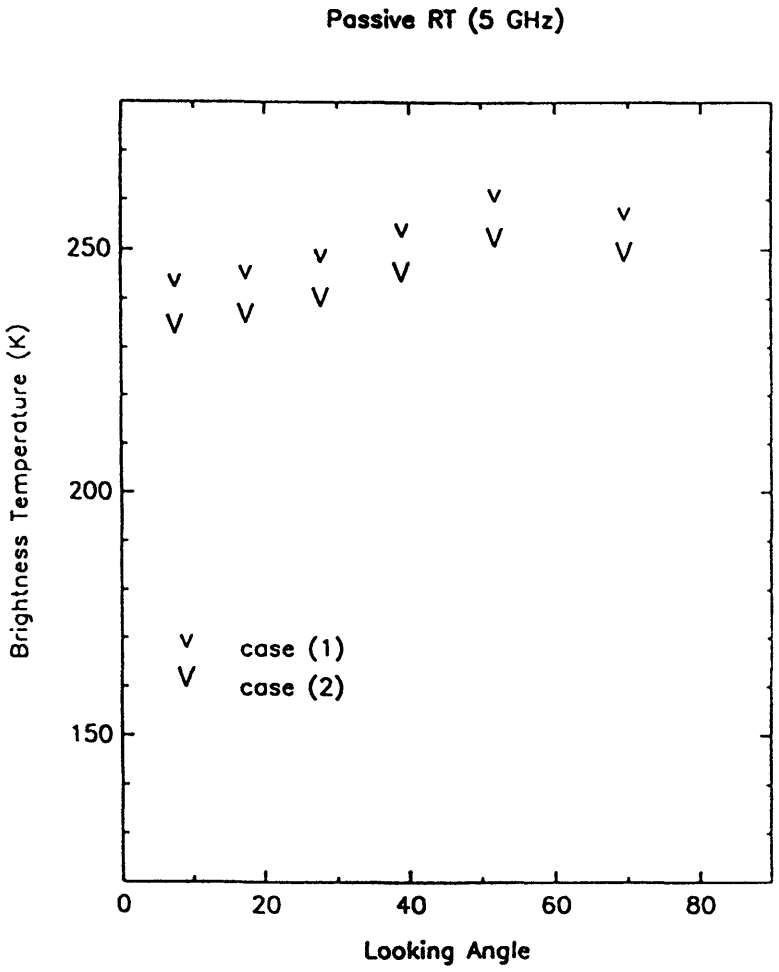

Figure 5.8: Brightness temperature as a function of looking angle for vertical polarization. Case 1: regions 1 and 2 contain brine inclusions, Case 2: region 1: air bubbles; region 2: brine inclusions

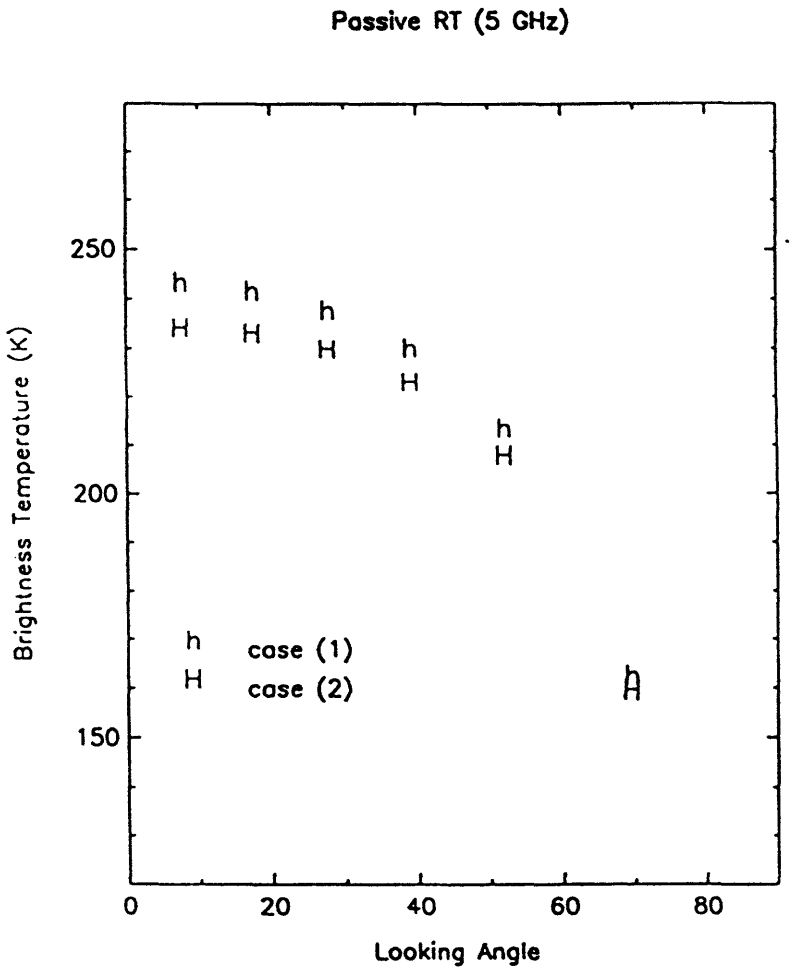

Figure 5.9: Brightness temperature as a function of looking angle for horizontal polarization. Case 1: regions 1 and 2 contain brine inclusions, Case 2: region 1: air bubbles; region 2: brine inclusions

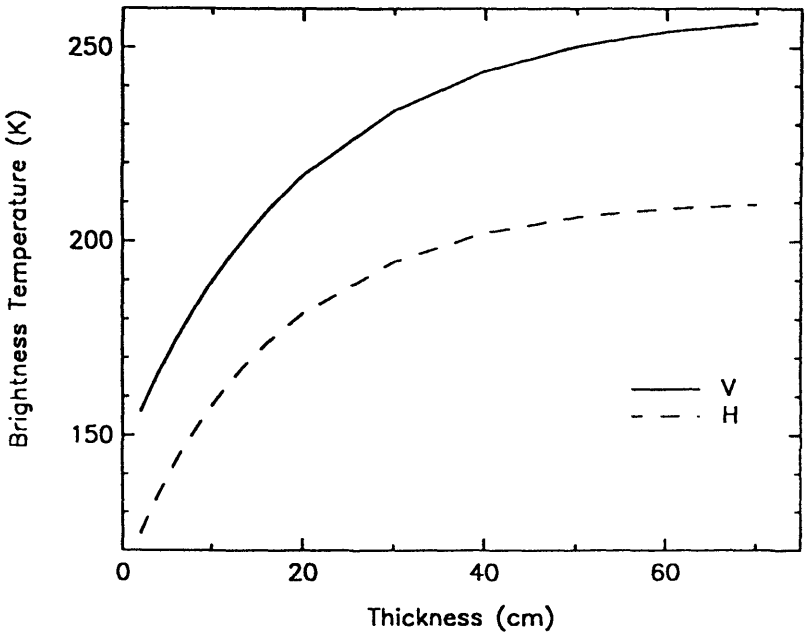

Figure 5.10: Brightness temperature as a function of sea ice thickness.

to be 20. The brightness temperatures for the vertical and horizontal polarizations are plotted in Figure 5.10 for $\theta = 52°$. The results illustrate the increase in the brightness temperature with the increase in the sea ice thickness. The rate of increase depends on the thickness of sea ice as well as the absorption and scattering characteristics of sea ice.

5.4 Summary

This chapter focused on the modeling for passive remote sensing of sea ice. A brief introduction to different passive sensor systems was followed by a discussion on the solution methods available to compute numerical results for brightness tem-

peratures of a sea ice structure. The bistatic scattering coefficients calculated in previous chapters are related to the emissivity through the principles of conservation of energy (e = 1 - r, where e is emissivity and r is reflectivity) and reciprocity. The theoretical results for different configurations were presented and the effects of different sea ice physical parameters on the brightness temperature were investigated. For a two layer sea ice structure with planar interfaces, the contribution of volume scattering for lossy scatterers to the brightness temperature was illustrated. The effects of different permittivity of scatterers on brightness temperature were also presented. The increase of the real part of the permittivity of the scatterers led to the decrease in the brightness temperature, whereas the trend of brightness temperature for increasing ϵ_s'' is dependent on the ratio of $(\epsilon_s''/\epsilon_s')$. The effects of bottom rough interface on brightness temperature were larger than that of the top rough interface. The two layer configuration was later extended to a multilayer structure when the effect of different types of scatterers on the brightness temperature was examined. Generally, bounded regions with air pockets embedded within showed lower brightness temperature than the regions which contained brine inclusions. Therefore, multiyear sea ice which has more air pockets than first year sea ice should give lower brightness temperatures.

Chapter 6

Summary

In this chapter, material covered in the previous chapters are briefly reviewed, and the results which are important will be pointed out. This is then followed by some suggestions for future works.

In Chapter 1, a brief discussion of the background research for this thesis was presented. A survey of the available theoretical methods to solve the problem was also included. This was then followed by a study of sea ice physical structure. A multilayer sea ice configuration was later proposed to imitate real sea ice structure. A concise description of the thesis was also included.

Chapter 2 started with the definition of Stokes vector, Mueller matrix, bistatic scattering coefficients and brightness temperatures. The configuration of a two layer sea ice model with flat interfaces was also included. The chapter then proceeded to the elaboration of the radiative transfer theory. The phase matrix and extinction matrix were defined and briefly discussed. The boundary condition issue was then highlighted before a step by step derivation of the numerical method used was presented. The calculated bistatic scattering coefficients for different cases were shown.

It was found that generally, the co-polarized scattering returns are higher than the cross-polarized ones in the forward and backward direction. However, due to the orientation of scattering pattern of the scatterers in the medium, cross-polarized terms become dominant over the co-polarized returns at $\phi = 90^o$. Later in the chapter, several cases were run for different ϵ_s'' (imaginary part of the permittivity of the scatterers). It was shown that though there is an inverse relation between the lossy property of the scatterers and the bistatic returns, a more appropriate indicator is the albedo which is the ratio of scattering loss over the total extinction loss. A study on the effects of different shape of the scatterer was also performed. In the forward and backward directions, generally, there is little difference in co-polarized scattering returns for different shapes. For cross-polarized returns, the returns of spherical scatterers and spheroids are only due to multiple scattering, and thus are lower than those of ellipsoids.

The theoretical model in Chapter 2 was then extended to a two layer random medium with rough interfaces in Chapter 3. The surface profile function and the spatial correlation of this function were assumed to be Gaussian distributed and the rough surface could be characterized by the surface rms height and correlation length. The rough surface effect was incorporated by modifying the boundary conditions which were elaborated in the chapter. For rough interfaces, the reflection and transmission matrices have both the coherent and incoherent components. The appropriate modification in the numerical calculation process was also presented. The theoretical results showed that the rough surface effect will add on to the co-polarized scattering returns in both forward and backward directions and the

increase in the returns is proportional to the scale of roughness. Since the SPM method applied takes into account only the zeroth and first order solution, there is no change in the cross-polarized returns for different scale of roughness of the interfaces.

Chapter 4 focused on the further extension of the two layer model to multilayer model. A generalized configuration for the multilayer random medium was illustrated. The effective boundary condition concept was implemented. This approach not only simplifies the computation process but also reduces the complexity of the problem by dealing with two layer problem at a time. For theoretical results, a comparison between two cases which imitate the first year and multilayer sea ice was carried out. It was found out that the case which has air bubbles embedded within the background medium (first year sea ice) has higher scattering returns than the other case which contains only brine inclusions. This was due to the fact that air bubbles are not lossy and mainly contribute to the scattering effect.

In Chapter 5, a general introduction to passive remote sensing was presented. This was followed by the description of different passive measurement methods. Numerical methods available to solve radiative transfer equations for passive case were examined, and the active approach one was selected because numerical procedures and data structure implemented in previous chapters can be applied too. The plots for brightness temperature for the vertical polarization (TM) and the horizontal polarization (TE) resemble the up side down plots of the reflectivity for both polarizations. The contribution of volume scattering by the scatterers was shown to be important. The analysis on the effects of permittivity of the scatterers

on brightness temperature showed that lossless scatterers which have higher permittivity generally scatter more and thus give lower brightness temperature. On the other hand, for lossy scatterers, scattering effects will be dominant over the attenuation effects when the imaginary part of the permittivity is comparable or larger than the real part. It was also shown that the brightness temperature for a rough interface will be higher than that of planar interface. Lastly, a three layer case was run to show that for a layered medium with air pockets, the brightness temperature will be lower than the one which has brine inclusions embedded within it. This means that for thermal radiation, multilayer sea ice will be colder than first year sea ice.

In this thesis, a multilayer theoretical model has been developed to enhance our understanding of the sea ice scattering problem for both the active and passive cases. This model can be further improved to represent more accurately the real sea ice physical structure. One of the modifications which can be implemented is the combination of the multilayer sea ice structure and a top layer of snow using the dense medium radiative transfer equations. The addition of the second-order SPM solution to the rough surface scattering effects is also suggested. This forward model can also be applied to the sea ice inversion problem to reconstruct sea ice physical parameters. The bistatic scattering coefficients and brightness temperatures calculated are particularly important in the attempt to solve for the inversion problem. More detailed ground truth such as the scatterer type, orientation, shape, permittivity and the distribution as a function of depth and a more accurate surface profile should be obtained. This will eventually make full use of the multilayer model

developed and the results from data comparison can further suggest improvements to the existing model.

Appendix A

Reflection and Transmission Matrices

A.1 Planar Surface

For a planar surface, the coherent reflection matrix at the interface $\alpha - \beta$ is given below [57]:

$$\overline{\overline{R}}^{\,c}_{\alpha\beta}(\theta_\alpha) = \begin{bmatrix} |S_{\alpha\beta}|^2 & 0 & 0 & 0 \\ 0 & |R_{\alpha\beta}|^2 & 0 & 0 \\ 0 & 0 & \mathrm{Re}\,(S_{\alpha\beta}R^*_{\alpha\beta}) & -\mathrm{Im}\,(S_{\alpha\beta}R^*_{\alpha\beta}) \\ 0 & 0 & \mathrm{Im}\,(S_{\alpha\beta}R^*_{\alpha\beta}) & \mathrm{Re}\,(S_{\alpha\beta}R^*_{\alpha\beta}) \end{bmatrix} \tag{A.1}$$

The coherent transmission matrix is

$$\overline{\overline{T}}^{\,c}_{\alpha\beta}(\theta_\alpha) = \frac{\epsilon'_\beta}{\epsilon'_\alpha} \begin{bmatrix} |Y_{\alpha\beta}|^2 & 0 & 0 & 0 \\ 0 & |X_{\alpha\beta}|^2 & 0 & 0 \\ 0 & 0 & \frac{\cos\theta_\beta}{\cos\theta_\alpha}\,\mathrm{Re}\,(Y_{\alpha\beta}X^*_{\alpha\beta}) & -\frac{\cos\theta_\beta}{\cos\theta_\alpha}\,\mathrm{Im}\,(Y_{\alpha\beta}X^*_{\alpha\beta}) \\ 0 & 0 & \frac{\cos\theta_\beta}{\cos\theta_\alpha}\,\mathrm{Im}\,(Y_{\alpha\beta}X^*_{\alpha\beta}) & \frac{\cos\theta_\beta}{\cos\theta_\alpha}\,\mathrm{Re}\,(Y_{\alpha\beta}X^*_{\alpha\beta}) \end{bmatrix} \tag{A.2}$$

where

$$R_{\alpha\beta} = \frac{k_{\alpha zi} - k_{\beta zi}}{k_{\alpha zi} + k_{\beta zi}} = X_{\alpha\beta} - 1 \tag{A.3}$$

$$S_{\alpha\beta} = \frac{k_\beta^2 k_{\alpha zi} - k_\alpha^2 k_{\beta zi}}{k_\beta^2 k_{\alpha zi} + k_\alpha^2 k_{\beta zi}} = Y_{\alpha\beta} - 1 \tag{A.4}$$

$S_{\alpha\beta}$ and $Y_{\alpha\beta}$ are reflection and transmission coefficients for vertically polarized waves respectively and $R_{\alpha\beta}$ and $X_{\alpha\beta}$ are reflection and transmission coefficients for horizontally polarized waves respectively. For planar surface, the incoherent reflection and transmission matrices are zero.

A.2 Slightly Rough Surface

A.2.1 Coherent Reflection and Transmission Matrices

This section is adapted from [45]. The coherent matrix is again given by equation (A.1) and (A.2) where $R_{\alpha\beta}$, $S_{\alpha\beta}$, $X_{\alpha\beta}$ and $Y_{\alpha\beta}$ are [57]:

$$\begin{aligned} R_{\alpha\beta} &= R_{ho} + k_{\alpha zi}\frac{(k_\beta^2 - k_\alpha^2)}{(k_{\alpha zi} + k_{\beta zi})^2}\sigma^2 l^2 \int_0^\infty k_\rho \, dk_\rho \exp\left[-\frac{1}{4}(k_\rho^2 + k_{\rho i}^2)l^2\right] \\ &\quad \cdot \left\{ \left[-\frac{(k_\beta^2 - k_\alpha^2)}{(k_{\alpha z} + k_{\beta z})}\frac{k_{\alpha z}k_{\beta z}}{k_{\alpha z}k_{\beta z} + k_\rho^2} + k_{\beta zi} \right] I_0(x) \right. \\ &\quad \left. - \frac{k_\beta^2 - k_\alpha^2}{k_{\alpha z} + k_{\beta z}}\frac{k_\rho^2}{k_{\alpha z}k_{\beta z} + k_\rho^2}\left(I_0(x) - \frac{I_1(x)}{x}\right) \right\} \end{aligned} \tag{A.5}$$

$$\begin{aligned} S_{\alpha\beta} &= R_{vo} - k_{\alpha zi}\frac{(k_\beta^2 - k_\alpha^2)}{(k_\alpha^2 k_{\beta zi} + k_\beta^2 k_{\alpha zi})^2}k_\alpha^2 k_\beta^2 \sigma^2 l^2 \int_0^\infty k_\rho \, dk_\rho \exp\left[-\frac{1}{4}(k_\rho^2 + k_{\rho i}^2)l^2\right] \\ &\quad \cdot \left\{ k_{\beta zi}\left(I_0(x) - 2\frac{k_\rho k_{\rho i}}{k_{\alpha z}k_{\beta z} + k_\rho^2}I_1(x)\right) - \frac{k_\beta^2 - k_\alpha^2}{k_{\alpha z} + k_{\beta z}}\frac{k_{\beta zi}^2}{k_\beta^2}I_0(x) \right. \end{aligned}$$

$$+\frac{k_\beta^2-k_\alpha^2}{k_{\alpha z}+k_{\beta z}}\frac{k_{\beta zi}^2}{k_\beta^2}\frac{k_\rho^2}{k_{\alpha z}k_{\beta z}+k_\rho^2}\cdot\left(I_0(x)-\frac{I_1(x)}{x}\right)$$

$$+\frac{k_\beta^2-k_\alpha^2}{k_{\alpha z}+k_{\beta z}}\frac{k_\rho^2k_{\rho i}^2}{k_{\alpha z}k_{\beta z}+k_\rho^2}\frac{1}{k_\alpha^2}\,I_0(x)\Bigg\} \tag{A.6}$$

$$X_{\alpha\beta} = 1+R_{ho}+k_{\alpha zi}\frac{(k_\beta^2-k_\alpha^2)}{(k_{\alpha zi}+k_{\beta zi})^2}\sigma^2l^2\int_0^\infty k_\rho\,dk_\rho\,\exp\left[-\frac{1}{4}(k_\rho^2+k_{\rho i}^2)l^2\right]$$

$$\cdot\left\{(k_{\alpha z}-k_{\beta z})\left(I_0(x)-\frac{k_\rho^2}{k_{\alpha z}k_{\beta z}+k_\rho^2}\frac{I_1(x)}{x}\right)-\frac{1}{2}(k_{\alpha zi}-k_{\beta zi})\,I_0(x)\right\} \tag{A.7}$$

$$Y_{\alpha\beta} = 1+R_{vo}+k_{\alpha zi}\frac{(k_\beta^2-k_{alp}^2)}{(k_\alpha^2k_{\beta zi}+k_\beta^2k_{\alpha zi})^2}k_\beta^2\sigma^2l^2\int_0^\infty k_\rho\,dk_\rho\,\exp\left[-\frac{1}{4}(k_\rho^2+k_{\rho i}^2)l^2\right]$$

$$\Bigg\{-\frac{1}{2}(k_\alpha^2k_{\beta zi}-k_\beta^2k_{\alpha zi})I_0(x)-(k_\beta^2-k_\alpha^2)\frac{k_\rho^2k_{\rho i}^2}{(k_\alpha^2k_{\beta z}+k_\beta^2k_{\alpha z})}I_0(x)$$

$$-\frac{(k_\beta^2-k_\alpha^2)}{(k_{\alpha z}+k_{\beta z})}k_{\alpha zi}k_{\beta zi}I_0(x)+(k_\beta^2-k_\alpha^2)\frac{k_\rho^2k_{\alpha zi}k_{\beta zi}}{(k_\alpha^2k_{\beta z}+k_\beta^2k_{\alpha z})}\left(I_0(x)-\frac{I_1(x)}{x}\right)$$

$$+\frac{k_{\alpha z}+k_{\beta z}}{k_\alpha^2k_{\beta z}+k_\beta^2k_{\alpha z}}k_\rho k_{\rho i}(k_\alpha^2k_{\beta zi}-k_\beta^2k_{\alpha zi})I_1(x)\Bigg\} \tag{A.8}$$

where $x=\frac{1}{2}k_\rho k_{\rho_i}l^2$, and I_0 and I_1 are the zeroth- and first-order modified Bessel functions, respectively. RMS height of the surface is denoted as σ and l is the correlation length for a Gaussian correlation function

A.2.2 Incoherent Reflection and Transmission Matrices

The incoherent matrices for the first order SPM solution [45,57] are given by:

$$\overline{\overline{R}}_{\alpha\beta}^{\,i} = \begin{bmatrix} \langle|f_{vv}^r|^2\rangle & \langle|f_{vh}^r|^2\rangle \\ \langle|f_{hv}^r|^2\rangle & \langle|f_{hh}^r|^2\rangle \\ 2\ \mathrm{Re}(\langle f_{vv}^r f_{hv}^{r\,*}\rangle) & 2\ \mathrm{Re}(\langle f_{vh}^r f_{hh}^{r\,*}\rangle) \\ 2\ \mathrm{Im}(\langle f_{vv}^r f_{hv}^{r\,*}\rangle) & 2\ \mathrm{Im}(\langle f_{vh}^r f_{hh}^{r\,*}\rangle) \end{bmatrix}$$

$$\begin{bmatrix} \mathrm{Re}(\langle f^r_{vv} f^{r\,*}_{vh}\rangle) & -\mathrm{Im}(\langle f^r_{vv} f^{r\,*}_{vh}\rangle) \\ \mathrm{Re}(\langle f^r_{hv} f^{r\,*}_{hh}\rangle) & -\mathrm{Im}(\langle f^r_{hv} f^{r\,*}_{hh}\rangle) \\ \mathrm{Re}(\langle f^r_{vv} f^{r\,*}_{hh} + f^r_{vh} f^{r\,*}_{hv}\rangle) & -\mathrm{Im}(\langle f^r_{vv} f^{r\,*}_{hh} - f^r_{vh} f^{r\,*}_{hv}\rangle) \\ \mathrm{Im}(\langle f^r_{vv} f^{r\,*}_{hh} + f^r_{vh} f^{r\,*}_{hv}\rangle) & \mathrm{Re}(\langle f^r_{vv} f^{r\,*}_{hh} - f^r_{vh} f^{r\,*}_{hv}\rangle) \end{bmatrix} \tag{A.9}$$

$$\overline{\overline{T}}^{\,i}_{\alpha\beta} = \begin{bmatrix} \langle |f^t_{vv}|^2\rangle & \langle |f^t_{vh}|^2\rangle \\ \langle |f^t_{hv}|^2\rangle & \langle |f^t_{hh}|^2\rangle \\ 2\ \mathrm{Re}(\langle f^t_{vv} f^{t\,*}_{hv}\rangle) & 2\ \mathrm{Re}(\langle f^t_{vh} f^{t\,*}_{hh}\rangle) \\ 2\ \mathrm{Im}(\langle f^t_{vv} f^{t\,*}_{hv}\rangle) & 2\ \mathrm{Im}(\langle f^t_{vh} f^{t\,*}_{hh}\rangle) \end{bmatrix}$$

$$\begin{bmatrix} \mathrm{Re}(\langle f^t_{vv} f^{t\,*}_{vh}\rangle) & -\mathrm{Im}(\langle f^t_{vv} f^{t\,*}_{vh}\rangle) \\ \mathrm{Re}(\langle f^t_{hv} f^{t\,*}_{hh}\rangle) & -\mathrm{Im}(\langle f^t_{hv} f^{t\,*}_{hh}\rangle) \\ \mathrm{Re}(\langle f^t_{vv} f^{t\,*}_{hh} + f^t_{vh} f^{t\,*}_{hv}\rangle) & -\mathrm{Im}(\langle f^t_{vv} f^{t\,*}_{hh} - f^t_{vh} f^{t\,*}_{hv}\rangle) \\ \mathrm{Im}(\langle f^t_{vv} f^{t\,*}_{hh} + f^t_{vh} f^{t\,*}_{hv}\rangle) & \mathrm{Re}(\langle f^t_{vv} f^{t\,*}_{hh} - f^t_{vh} f^{t\,*}_{hv}\rangle) \end{bmatrix} \tag{A.10}$$

where

$$\langle f^\gamma_{pq} f^{\gamma\,*}_{uw}\rangle = (g^\gamma_{pq})\cdot(g^\gamma_{uw})^* \qquad \gamma = r,t \ \text{ and } \ p,q,u,w = h,v \tag{A.11}$$

and

$$g^r_{vv} = m^r(\theta_t,\theta_i)\left\{\frac{(k_\beta^2-k_\alpha^2)}{(k_\alpha^2 k_{\beta z}+k_\beta^2 k_{\alpha z})(k_\alpha^2 k_{\beta zi}+k_\beta^2 k_{\alpha zi})}\left[k_\alpha^2 k_\beta^2 \sin\theta_s \sin\theta_i - k_\alpha^2 k_{\beta z} k_{\beta zi}\cos(\phi_s-\phi_i)\right]\right\} \tag{A.12}$$

$$g^r_{vh} = \zeta\cdot m^r(\theta_t,\theta_i)\left\{\frac{(k_\beta^2-k_\alpha^2)k_\alpha k_{\beta z}}{(k_\alpha^2 k_{\beta z}+k_\beta^2 k_{\alpha z})(k_{\alpha zi}+k_{\beta zi})}\right\}\sin(\phi_s-\phi_i) \tag{A.13}$$

$$g^r_{hv} = \zeta\cdot m^r(\theta_t,\theta_i)\left\{\frac{(k_\beta^2-k_\alpha^2)k_\alpha k_{\beta zi}}{(k_\alpha^2 k_{\beta zi}+k_\beta^2 k_{\alpha zi})(k_{\alpha z}+k_{\beta z})}\right\}\sin(\phi_s-\phi_i) \tag{A.14}$$

$$g^r_{hh} = m^r(\theta_t,\theta_i)\left\{\frac{(k_\beta^2-k_\alpha^2)}{(k_{\alpha z}+k_{\beta z})(k_{\alpha zi}+k_{\beta zi})}\right\}\cos(\phi_s-\phi_i) \tag{A.15}$$

and

$$g_{vv}^t = m^t(\theta_t,\theta_i)\left\{\frac{(k_\beta^2-k_\alpha^2)k_\alpha k_\beta}{(k_\alpha^2 k_{\beta z}+k_\beta^2 k_{\alpha z})(k_\alpha^2 k_{\beta zi}+k_\beta^2 k_{\alpha zi})}[k_\alpha k_\beta \sin\theta_t \sin\theta_i - k_{\alpha z}k_{\beta zi}\cos(\phi_t-\phi_i)]\right\} \quad (A.16)$$

$$g_{vh}^t = -\zeta\cdot m^t(\theta_t,\theta_i)\left\{\frac{(k_\beta^2-k_\alpha^2)k_\beta k_{\alpha z}}{(k_\alpha^2 k_{\beta z}+k_\beta^2 k_{\alpha z})(k_{\alpha zi}+k_{\beta zi})}\right\}\sin(\phi_t-\phi_i) \quad (A.17)$$

$$g_{hv}^t = \zeta\cdot m^t(\theta_t,\theta_i)\left\{\frac{(k_\beta^2-k_\alpha^2)k_\alpha k_{\beta zi}}{(k_\alpha^2 k_{\beta zi}+k_\beta^2 k_{\alpha zi})(k_{\alpha z}+k_{\beta z})}\right\}\sin(\phi_t-\phi_i) \quad (A.18)$$

$$g_{hh}^t = m^t(\theta_t,\theta_i)\left\{\frac{(k_\beta^2-k_\alpha^2)}{(k_{\alpha z}+k_{\beta z})(k_{\alpha zi}+k_{\beta zi})}\right\}\cos(\phi_t-\phi_i) \quad (A.19)$$

with

$$|m^r(\theta_s,\theta_i)|^2 = \frac{k_\alpha^4\sigma^2 l^2\cos\theta_s\cos^2\theta_i}{\pi}e^{-1/4(\sin^2\theta_s+\sin^2\theta_i)k_\alpha^2 l^2} \cdot e^{1/2(\sin\theta_s\cdot\sin\theta_i)k_\alpha^2 l^2\cos(\phi_s-\phi_i)} \quad (A.20)$$

$$|m^t(\theta_t,\theta_i)|^2 = \frac{\eta_\alpha k_\alpha^2 k_\beta^2\sigma^2 l^2\cos\theta_t\cos^2\theta_i}{\eta_\beta\ \pi}e^{-1/4(k_\beta^2\sin^2\theta_t+k_\alpha^2\sin^2\theta_i)l^2} \cdot e^{1/2(\sin\theta_t\cdot\sin\theta_i)k_\alpha k_\beta\ l^2\cos(\phi_t-\phi_i)} \quad (A.21)$$

where η is the medium impedance and $\zeta = 1$ when the incident wave propagates in the downward direction ($\overline{\overline{R}}_{01}$, $\overline{\overline{T}}_{01}$, $\overline{\overline{R}}_{12}$, $\cdots$) and $\zeta = -1$ when the incident wave propagates in the upward direction ($\overline{\overline{R}}_{10}$, $\overline{\overline{T}}_{10}$, $\cdots$).

Finally, the Fourier series for these expressions can easily be obtained by using

the following relations:

$$\cos(mx)\cdot e^{R\cos x} = \sum_{n=0}^{\infty}\frac{1}{1+\delta_{n0}}\cdot[I_{m-n}(R)+I_{m+n}(R)]\cdot\cos(nx) \quad (A.22)$$

$$\sin(mx)\cdot e^{R\cos x} = \sum_{n=0}^{\infty}[I_{m-n}(R)-I_{m+n}(R)]\cdot\sin(nx) \quad (A.23)$$

where $I_{m\pm n}(R)$ is the $(m\pm n)$-th order modified Bessel function of argument R.

Appendix B

Phase and Extinction Matrices

B.1 Scattering Matrix for a Single Ellipsoid

Appendix B is adapted from [45]. The scattering matrix for a single ellipsoidal scatterer with prescribed orientation α, β, γ and characterized by a permittivity ϵ_s and semi-major axis lengths a, b and c, is given by [45,57]: The scattering matrix for a single ellipsoidal scatterer can be described as [45,57]

$$\overline{\overline{F}} = \begin{bmatrix} f_{vv} & f_{vh} \\ f_{hv} & f_{hh} \end{bmatrix} \tag{B.1}$$

where

$$f_{pq} = \frac{k^2}{4\pi} v_o \frac{\epsilon_s - \epsilon}{\epsilon} \cdot \left(\frac{(\hat{p}_s \cdot \hat{x}_b)(\hat{x}_b \cdot \hat{q}_i)}{1 + v_d A_a} + \frac{(\hat{p}_s \cdot \hat{y}_b)(\hat{y}_b \cdot \hat{q}_i)}{1 + v_d A_b} + \frac{(\hat{p}_s \cdot \hat{z}_b)(\hat{z}_b \cdot \hat{q}_i)}{1 + v_d A_c} \right) \tag{B.2}$$

with p, $q = h$ or v, ϵ_s is the permittivity of the scatterer, α, β and γ are the Eulerian angles of the scatterer and a, b and c are the semi-major axis lengths of an ellipsoid.

The propagation (k) and polarization (v, h) vectors are shown below:

$$\hat{k}_s = \sin\theta_s \cos\phi_s \hat{x} + \sin\theta_s \sin\phi_s \hat{y} + \cos\theta_s \hat{z} \tag{B.3}$$

$$\hat{v}_s = \cos\theta_s \cos\phi_s \hat{x} + \cos\theta_s \sin\phi_s \hat{y} - \sin\theta_s \hat{z} \tag{B.4}$$

$$\hat{h}_s = -\sin\phi_s \hat{x} + \cos\phi_s \hat{y} \tag{B.5}$$

$$\hat{k}_i = \sin\theta_i \cos\phi_i \hat{x} + \sin\theta_i \sin\phi_i \hat{y} + \cos\theta_i \hat{z} \tag{B.6}$$

$$\hat{v}_i = \cos\theta_i \cos\phi_i \hat{x} + \cos\theta_i \sin\phi_i \hat{y} - \sin\theta_i \hat{z} \tag{B.7}$$

$$\hat{h}_i = -\sin\phi_i \hat{x} + \cos\phi_i \hat{y} \tag{B.8}$$

$$v_o = \frac{4\pi}{3} abc \tag{B.9}$$

$$v_d = \frac{abc}{2} \frac{\epsilon_s - \epsilon}{\epsilon} \tag{B.10}$$

$$A_t = \int_0^\infty \frac{ds}{(s+t^2)\sqrt{(s+a^2)(s+b^2)(s+c^2)}} \tag{B.11}$$

with $t = a$, b or c.

The coordinate system of the ellipsoid ($\hat{x}_b$, $\hat{y}_b$, $\hat{z}_b$) can be related to the global coordinate system ($\hat{x}$, $\hat{y}$, $\hat{z}$) in the following way [45,57]:

$$\begin{bmatrix} \hat{x} \\ \hat{y} \\ \hat{z} \end{bmatrix} = \begin{bmatrix} a_{11} & a_{12} & a_{13} \\ a_{21} & a_{22} & a_{23} \\ a_{31} & a_{32} & a_{33} \end{bmatrix} \cdot \begin{bmatrix} \hat{x}_b \\ \hat{y}_b \\ \hat{z}_b \end{bmatrix} \tag{B.12}$$

with

$$a_{11} = \cos\gamma\cos\beta\cos\alpha - \sin\gamma\sin\alpha \quad \text{(B.13)}$$

$$a_{12} = \cos\gamma\cos\beta\sin\alpha + \sin\gamma\cos\alpha \quad \text{(B.14)}$$

$$a_{13} = -\cos\gamma\sin\beta \quad \text{(B.15)}$$

$$a_{21} = -\sin\gamma\cos\beta\cos\alpha - \cos\gamma\sin\alpha \quad \text{(B.16)}$$

$$a_{22} = -\sin\gamma\cos\beta\sin\alpha + \cos\gamma\cos\alpha \quad \text{(B.17)}$$

$$a_{23} = \sin\gamma\sin\beta \quad \text{(B.18)}$$

$$a_{31} = \sin\beta\cos\alpha \quad \text{(B.19)}$$

$$a_{32} = \sin\beta\sin\alpha \quad \text{(B.20)}$$

$$a_{33} = \cos\beta \quad \text{(B.21)}$$

B.2 Phase Matrix

B.2.1 Vertically Aligned Ellipsoids

In this subsection the phase matrix for a set of ellipsoids of dimension $a = a_o$, $b = b_o$ and $c = c_o$, with their semi-major axis c_o parallel to the $\hat{z}$-axis and uniformly distributed in the azimuthal direction, is given. The joint probability density function

is given by

$$\mathrm{p}(a,b,c,\alpha,\beta,\gamma) = \delta(a-a_o)\delta(b-b_o)\delta(c-c_o)\delta(\beta)\delta(\gamma)\frac{1}{2\pi} \tag{B.22}$$

Then the phase matrix can be calculated from (B.2) and is given by

$$\overline{\overline{P}}(\theta_s,\phi_s;\theta_i,\phi_i) = \frac{1}{1+\delta_m}\sum_{m=0}^{\infty}\left(\overline{\overline{P}}^{mc}\cos(m(\phi_s-\phi_i)) + \overline{\overline{P}}^{ms}\sin(m(\phi_s-\phi_i))\right) \tag{B.23}$$

and

$$\overline{\overline{P}}^{0c} = \begin{bmatrix} p_{11}^{0c} & p_{12}^{0c} & 0 & 0 \\ p_{21}^{0c} & p_{22}^{0c} & 0 & 0 \\ 0 & 0 & 0 & 0 \\ 0 & 0 & 0 & p_{44}^{0c} \end{bmatrix} \tag{B.24}$$

$$\overline{\overline{P}}^{1c} = \begin{bmatrix} p_{11}^{1c} & 0 & 0 & 0 \\ 0 & 0 & 0 & 0 \\ 0 & 0 & p_{33}^{1c} & p_{34}^{1c} \\ 0 & 0 & p_{43}^{1c} & p_{44}^{1c} \end{bmatrix} \tag{B.25}$$

$$\overline{\overline{P}}^{2c} = \begin{bmatrix} p_{11}^{2c} & p_{12}^{2c} & 0 & 0 \\ p_{21}^{2c} & p_{22}^{2c} & 0 & 0 \\ 0 & 0 & p_{33}^{2c} & 0 \\ 0 & 0 & 0 & 0 \end{bmatrix} \tag{B.26}$$

$$\overline{\overline{P}}^{1s} = \begin{bmatrix} 0 & 0 & p_{13}^{1s} & p_{14}^{1s} \\ 0 & 0 & 0 & 0 \\ p_{31}^{1s} & 0 & 0 & 0 \\ p_{41}^{1s} & 0 & 0 & 0 \end{bmatrix} \tag{B.27}$$

$$\overline{\overline{P}}^{2s} = \begin{bmatrix} 0 & 0 & p_{13}^{2s} & 0 \\ 0 & 0 & p_{23}^{2s} & 0 \\ p_{31}^{2s} & p_{32}^{2s} & 0 & 0 \\ 0 & 0 & 0 & 0 \end{bmatrix} \tag{B.28}$$

where

$$p_{11}^{0c} = |q|^2 n_o \pi \left[\frac{1}{2}(T_{A2} + T_{B2}) \cos^2\theta_s \cos^2\theta_i + 2\, T_{C2} \sin^2\theta_s \sin^2\theta_i\right] \tag{B.29}$$

$$p_{12}^{0c} = |q|^2 n_o \pi \left[\frac{1}{2}(T_{A2} + T_{B2}) \cos^2\theta_s\right] \tag{B.30}$$

$$p_{21}^{0c} = |q|^2 n_o \pi \left[\frac{1}{2}(T_{A2} + T_{B2}) \cos^2\theta_i\right] \tag{B.31}$$

$$p_{22}^{0c} = |q|^2 n_o \pi \left[\frac{1}{2}(T_{A2} + T_{B2})\right] \tag{B.32}$$

$$p_{44}^{0c} = |q|^2 n_o \pi \left[T_{ABBA} \cos\theta_s \cos\theta_i\right] \tag{B.33}$$

$$p_{11}^{1c} = |q|^2 n_o \pi \left[\frac{1}{2}(T_{BCCB} + T_{CAAC}) \cos\theta_s \sin\theta_s \cos\theta_i \sin\theta_i\right] \tag{B.34}$$

$$p_{33}^{1c} = |q|^2 n_o \pi \left[\frac{1}{2} \mathrm{Re}\,(T_{CA} + T_{CB}) \sin\theta_s \sin\theta_i\right] \tag{B.35}$$

$$p_{34}^{1c} = -|q|^2 n_o \pi \left[\frac{1}{2} \mathrm{Im}\,(T_{CA} + T_{CB}) \sin\theta_s \sin\theta_i\right] \tag{B.36}$$

$$p_{43}^{1c} = |q|^2 n_o \pi \left[\frac{1}{2} \mathrm{Im}\,(T_{CA} + T_{CB}) \sin\theta_s \sin\theta_i\right] \tag{B.37}$$

$$p_{44}^{1c} = |q|^2 n_o \pi \left[\frac{1}{2} \mathrm{Re}\,(T_{CA} + T_{CB}) \sin\theta_s \sin\theta_i\right] \tag{B.38}$$

$$p_{11}^{2c} = |q|^2 n_o \pi \left[\frac{1}{8}(T_{A2} + T_{B2} + T_{ABBA}) \cos^2\theta_s \cos^2\theta_i\right] \tag{B.39}$$

$$p_{12}^{2c} = -|q|^2 n_o \pi \left[\frac{1}{8}(T_{A2} + T_{B2} + T_{ABBA}) \cos^2 \theta_s\right] \quad \text{(B.40)}$$

$$p_{21}^{2c} = -|q|^2 n_o \pi \left[\frac{1}{8}(T_{A2} + T_{B2} + T_{ABBA}) \cos^2 \theta_i\right] \quad \text{(B.41)}$$

$$p_{22}^{2c} = |q|^2 n_o \pi \left[\frac{1}{8}(T_{A2} + T_{B2} + T_{ABBA})\right] \quad \text{(B.42)}$$

$$p_{33}^{2c} = |q|^2 n_o \pi \left[\frac{1}{4}(T_{A2} + T_{B2} + T_{ABBA}) \cos\theta_s \cos\theta_i\right] \quad \text{(B.43)}$$

$$p_{13}^{1s} = |q|^2 n_o \pi \left[\frac{1}{2} \mathrm{Re}\,(T_{CA} + T_{CB}) \cos\theta_s \sin\theta_s \sin\theta_i\right] \quad \text{(B.44)}$$

$$p_{14}^{1s} = -|q|^2 n_o \pi \left[\frac{1}{2} \mathrm{Im}\,(T_{CA} + T_{CB}) \cos\theta_s \sin\theta_s \sin\theta_i\right] \quad \text{(B.45)}$$

$$p_{31}^{1s} = -|q|^2 n_o \pi \left[\mathrm{Re}\,(T_{CA} + T_{CB}) \sin\theta_s \cos\theta_i \sin\theta_i\right] \quad \text{(B.46)}$$

$$p_{41}^{1s} = -|q|^2 n_o \pi \left[\mathrm{Im}\,(T_{CA} + T_{CB}) \sin\theta_s \cos\theta_i \sin\theta_i\right] \quad \text{(B.47)}$$

$$p_{13}^{2s} = |q|^2 n_o \pi \left[\frac{1}{8}(T_{A2} + T_{B2} + T_{ABBA}) \cos^2\theta_s \cos\theta_i\right] \quad \text{(B.48)}$$

$$p_{23}^{2s} = -|q|^2 n_o \pi \left[\frac{1}{8}(T_{A2} + T_{B2} + T_{ABBA}) \cos\theta_i\right] \quad \text{(B.49)}$$

$$p_{31}^{2s} = -|q|^2 n_o \pi \left[\frac{1}{4}(T_{A2} + T_{B2} + T_{ABBA}) \cos\theta_s \cos^2\theta_i\right] \quad \text{(B.50)}$$

$$p_{32}^{2s} = |q|^2 n_o \pi \left[\frac{1}{4}(T_{A2} + T_{B2} + T_{ABBA}) \cos\theta_s\right] \quad \text{(B.51)}$$

with

$$q = \frac{k^2}{4\pi} v_o \frac{(\epsilon_s - \epsilon)}{\epsilon} \quad \text{(B.52)}$$

and

$$T_{A2} = \left|\frac{1}{1+v_d A_a}\right|^2 \tag{B.53}$$

$$T_{B2} = \left|\frac{1}{1+v_d A_b}\right|^2 \tag{B.54}$$

$$T_{C2} = \left|\frac{1}{1+v_d A_c}\right|^2 \tag{B.55}$$

$$T_{ABBA} = \frac{1}{(1+v_d A_a)}\frac{1}{(1+v_d A_b)^*} + \frac{1}{(1+v_d A_b)}\frac{1}{(1+v_d A_a)^*} \tag{B.56}$$

$$T_{BCCB} = \frac{1}{(1+v_d A_b)}\frac{1}{(1+v_d A_c)^*} + \frac{1}{(1+v_d A_c)}\frac{1}{(1+v_d A_b)^*} \tag{B.57}$$

$$T_{CAAC} = \frac{1}{(1+v_d A_c)}\frac{1}{(1+v_d A_a)^*} + \frac{1}{(1+v_d A_a)}\frac{1}{(1+v_d A_c)^*} \tag{B.58}$$

$$T_{CA} = \frac{1}{(1+v_d A_c)}\frac{1}{(1+v_d A_a)^*} \tag{B.59}$$

$$T_{CB} = \frac{1}{(1+v_d A_c)}\frac{1}{(1+v_d A_b)^*} \tag{B.60}$$

where v_o, v_d and A_t are given by (B.9), (B.10) and (B.11), respectively.

B.2.2 Randomly Oriented Ellipsoids

In this subsection the phase matrix for a set of ellipsoids of dimension a_o, b_o and c_o, with random orientation distribution is given. The joint probability density function is given by

$$\mathrm{p}(a,b,c,\alpha,\beta,\gamma) = \delta(a-a_o)\delta(b-b_o)\delta(c-c_o)\frac{1}{2\pi}\frac{\sin\beta}{2}\frac{1}{2\pi} \tag{B.61}$$

The phase matrix can be calculated from (B.2) and is given by

$$\overline{\overline{P}}(\theta_s, \phi_s; \theta_i, \phi_i) = \frac{1}{1+\delta_m} \sum_{m=0}^{\infty} \left(\overline{\overline{P}}^{mc} \cos(m(\phi_s - \phi_i)) + \overline{\overline{P}}^{ms} \sin(m(\phi_s - \phi_i)) \right) \quad \text{(B.62)}$$

and

$$\overline{\overline{P}}^{0c} = \begin{bmatrix} p_{11}^{0c} & p_{12}^{0c} & 0 & 0 \\ p_{21}^{0c} & p_{22}^{0c} & 0 & 0 \\ 0 & 0 & 0 & 0 \\ 0 & 0 & 0 & p_{44}^{0c} \end{bmatrix} \quad \text{(B.63)}$$

$$\overline{\overline{P}}^{1c} = \begin{bmatrix} p_{11}^{1c} & 0 & 0 & 0 \\ 0 & 0 & 0 & 0 \\ 0 & 0 & p_{33}^{1c} & 0 \\ 0 & 0 & 0 & p_{44}^{1c} \end{bmatrix} \quad \text{(B.64)}$$

$$\overline{\overline{P}}^{2c} = \begin{bmatrix} p_{11}^{2c} & p_{12}^{2c} & 0 & 0 \\ p_{21}^{2c} & p_{22}^{2c} & 0 & 0 \\ 0 & 0 & p_{33}^{2c} & 0 \\ 0 & 0 & 0 & 0 \end{bmatrix} \quad \text{(B.65)}$$

$$\overline{\overline{P}}^{1s} = \begin{bmatrix} 0 & 0 & p_{13}^{1s} & 0 \\ 0 & 0 & 0 & 0 \\ p_{31}^{1s} & 0 & 0 & 0 \\ 0 & 0 & 0 & 0 \end{bmatrix} \quad \text{(B.66)}$$

$$\overline{\overline{P}}^{2s} = \begin{bmatrix} 0 & 0 & p_{13}^{2s} & 0 \\ 0 & 0 & p_{23}^{2s} & 0 \\ p_{31}^{2s} & p_{32}^{2s} & 0 & 0 \\ 0 & 0 & 0 & 0 \end{bmatrix} \quad \text{(B.67)}$$

where

$$p_{11}^{0c} = |q|^2 n_o \pi \left[(\frac{4}{15}T_1 + \frac{1}{30}T_2)\cos^2\theta_s \cos^2\theta_i + (\frac{2}{5}T_1 + \frac{2}{15}T_2)\sin^2\theta_s \sin^2\theta_i \right.$$
$$\left. + (\frac{2}{15}T_1 - \frac{1}{15}T_2)(\sin^2\theta_s \cos^2\theta_i + \cos^2\theta_s \sin^2\theta_i) \right] \quad \text{(B.68)}$$

$$p_{12}^{0c} = |q|^2 n_o \pi \left[(\frac{4}{15}T_1 + \frac{1}{30}T_2)\cos^2\theta_s + (\frac{2}{15}T_1 - \frac{1}{15}T_2)\sin^2\theta_s \right] \quad \text{(B.69)}$$

$$p_{21}^{0c} = |q|^2 n_o \pi \left[(\frac{4}{15}T_1 + \frac{1}{30}T_2)\cos^2\theta_i + (\frac{2}{15}T_1 - \frac{1}{15}T_2)\sin^2\theta_i \right] \quad \text{(B.70)}$$

$$p_{22}^{0c} = |q|^2 n_o \pi \left[\frac{4}{15}T_1 + \frac{1}{30}T_2 \right] \quad \text{(B.71)}$$

$$p_{44}^{0c} = |q|^2 n_o \pi \left[\frac{1}{3}T_2 \cos\theta_s \cos\theta_i \right] \quad \text{(B.72)}$$

$$p_{11}^{1c} = |q|^2 n_o \pi \left[(\frac{4}{15}T_1 + \frac{1}{5}T_2)\cos\theta_s \sin\theta_s \cos\theta_i \sin\theta_i \right] \quad \text{(B.73)}$$

$$p_{33}^{1c} = |q|^2 n_o \pi \left[(\frac{2}{15}T_1 + \frac{1}{10}T_2)\sin\theta_s \sin\theta_i \right] \quad \text{(B.74)}$$

$$p_{44}^{1c} = |q|^2 n_o \pi \left[\frac{1}{6}T_2 \sin\theta_s \sin\theta_i \right] \quad \text{(B.75)}$$

$$p_{11}^{2c} = |q|^2 n_o \pi \left[(\frac{1}{15}T_1 + \frac{1}{20}T_2)\cos^2\theta_s \cos^2\theta_i \right] \quad \text{(B.76)}$$

$$p_{12}^{2c} = -|q|^2 n_o \pi \left[(\frac{1}{15}T_1 + \frac{1}{20}T_2)\cos^2\theta_s \right] \quad \text{(B.77)}$$

$$p_{21}^{2c} = -|q|^2 n_o \pi \left[(\frac{1}{15}T_1 + \frac{1}{20}T_2)\cos^2\theta_i \right] \quad \text{(B.78)}$$

$$p_{22}^{2c} = |q|^2 n_o \pi \left[(\frac{1}{15}T_1 + \frac{1}{20}T_2) \right] \quad \text{(B.79)}$$

$$p_{33}^{2c} = |q|^2 n_o \pi \left[\left(\frac{2}{15} T_1 + \frac{1}{10} T_2 \right) \cos\theta_s \cos\theta_i \right] \tag{B.80}$$

$$p_{13}^{1s} = |q|^2 n_o \pi \left[\left(\frac{2}{15} T_1 + \frac{1}{10} T_2 \right) \cos\theta_s \sin\theta_s \sin\theta_i \right] \tag{B.81}$$

$$p_{31}^{1s} = -|q|^2 n_o \pi \left[\left(\frac{4}{15} T_1 + \frac{1}{5} T_2 \right) \sin\theta_s \cos\theta_i \sin\theta_i \right] \tag{B.82}$$

$$p_{13}^{2s} = |q|^2 n_o \pi \left[\left(\frac{1}{15} T_1 + \frac{1}{20} T_2 \right) \cos^2\theta_s \cos\theta_i \right] \tag{B.83}$$

$$p_{23}^{2s} = -|q|^2 n_o \pi \left[\left(\frac{1}{15} T_1 + \frac{1}{20} T_2 \right) \cos\theta_i \right] \tag{B.84}$$

$$p_{31}^{2s} = -|q|^2 n_o \pi \left[\left(\frac{2}{15} T_1 + \frac{1}{10} T_2 \right) \cos\theta_s \cos^2\theta_i \right] \tag{B.85}$$

$$p_{32}^{2s} = |q|^2 n_o \pi \left[\left(\frac{2}{15} T_1 + \frac{1}{10} T_2 \right) \cos\theta_s \right] \tag{B.86}$$

with

$$q = \frac{k^2}{4\pi} v_o \frac{(\epsilon_s - \epsilon)}{\epsilon} \tag{B.87}$$

and

$$T_1 = T_{A2} + T_{B2} + T_{C2} \tag{B.88}$$

$$T_2 = T_{ABBA} + T_{BCCB} + T_{CAAC} \tag{B.89}$$

where T_{A2}, T_{B2}, T_{C2}, T_{ABBA}, T_{BCCB} and T_{CAAC} are respectively given by (B.53)-(B.55) and (B.56)-(B.58).

B.3 Extinction Matrix

B.3.1 Vetically Aligned Ellipsoids

In this section, the absorbtion and scattering loss matrices due to vertically aligned ellipsoidal scatterers are presented. The joint probability density function for orientation and size distribution is given by (B.22).

The absorption matrix due to the scatterers is calculated using the extinction theorem and is given by:

$$\bar{\bar{\kappa}}_{as} = \begin{bmatrix} \kappa_{as_{11}} & 0 & 0 & 0 \\ 0 & \kappa_{as_{22}} & 0 & 0 \\ 0 & 0 & \kappa_{as_{33}} & \kappa_{as_{34}} \\ 0 & 0 & \kappa_{as_{43}} & \kappa_{as_{44}} \end{bmatrix} \tag{B.90}$$

where

$$\kappa_{as_{11}} = \text{Im}\left\{\frac{4\pi n_o q}{k}\left[\frac{1}{2}\cos^2\theta\,(T_A+T_B)+\sin^2\theta\,T_C\right]\right\} \tag{B.91}$$

$$\kappa_{as_{22}} = \text{Im}\left\{\frac{4\pi n_o q}{k}\,\frac{1}{2}\,(T_A+T_B)\right\} \tag{B.92}$$

$$\kappa_{as_{33}} = \frac{\kappa_{as_{11}}+\kappa_{as_{22}}}{2} \tag{B.93}$$

$$\kappa_{as_{44}} = \kappa_{as_{33}} \tag{B.94}$$

$$\kappa_{as_{34}} = \text{Re}\left\{\frac{4\pi n_o q}{k}\,\sin^2\theta\left[\frac{1}{2}\,(T_A+T_B)-T_C\right]\right\} \tag{B.95}$$

$$\kappa_{as_{43}} = -\kappa_{as_{34}} \tag{B.96}$$

and

$$T_A = \frac{1}{1 + v_d A_a} \tag{B.97}$$

$$T_B = \frac{1}{1 + v_d A_b} \tag{B.98}$$

$$T_C = \frac{1}{1 + v_d A_c} \tag{B.99}$$

where n_o is the scatterer density and q, v_d and A_t are given by equations (B.52), (B.10) and (B.11), respectively.

The scattering loss matrix is

$$\kappa_{sv} = \frac{4\ n_o \pi |q|^2}{3} \left\{ \cos^2\theta\ (T_{A2} + T_{B2}) + 2\sin^2\theta\ T_{C2} \right\} \tag{B.100}$$

$$\kappa_{sh} = \frac{4\ n_o \pi |q|^2}{3} (T_{A2} + T_{B2}) \tag{B.101}$$

where T_{A2}, T_{B2} and T_{C2} are given by equations (B.53- B.55).

B.3.2 Randomly Oriented Ellipsoids

In this section, the absorbtion and scattering loss matrices due to randomly orientated ellipsoidal scatterers are obtained. The joint probability density function for orientation and size distribution is given by (B.61).

The absorption matrix due to the scatterers is calculated using the extinction

theorem and is given by

$$\overline{\overline{\kappa}}_{as} = \begin{bmatrix} \kappa_{as_{11}} & 0 & 0 & 0 \\ 0 & \kappa_{as_{22}} & 0 & 0 \\ 0 & 0 & \kappa_{as_{33}} & 0 \\ 0 & 0 & 0 & \kappa_{as_{44}} \end{bmatrix} \tag{B.102}$$

where

$$\kappa_{as_{11}} = \text{Im}\left\{\frac{4\pi n_o q}{k}\,\frac{1}{3}\,(T_A + T_B + T_C)\right\} \tag{B.103}$$

$$\kappa_{as_{22}} = \kappa_{as_{11}} \tag{B.104}$$

$$\kappa_{as_{33}} = \kappa_{as_{11}} \tag{B.105}$$

$$\kappa_{as_{44}} = \kappa_{as_{11}} \tag{B.106}$$

T_A, T_B and T_C are given by equations (B.97-B.99), n_o is the scatterer density and q, v_d and A_t are given by equations (B.52), (B.10) and (B.11), respectively.

The scattering loss matrix is

$$\kappa_{sv} = n_o \pi |q|^2 \,\frac{8}{9}\, T_1 \tag{B.107}$$

$$\kappa_{sh} = \kappa_{sv} \tag{B.108}$$

where T_1 is given by equation (B.88).

Appendix C

Single Dipole Scattering

C.1 Radiation Pattern of a Dipole

The electromagnetic scattering from a scatterer which is much smaller than a wavelength is characterized as Rayleigh scattering. A plane wave polarized in the $\hat{z}$ direction is incident upon a spherical scatterer with permittivity ϵ_s and permeability μ_s, and radius a. The scattered electric and magnetic fields are given by

$$E_\theta = -(\frac{\epsilon_s - \epsilon}{\epsilon_s + 2\epsilon})k^2 a^2 E_0 \frac{a}{r} e^{ikr} \sin\theta \tag{C.1}$$

$$H_\phi = \sqrt{\frac{\epsilon}{\mu}} E_\theta \tag{C.2}$$

The radiation pattern has the same pattern as that of the Hertzian dipole. Figure C.1 shows the radiation field pattern.

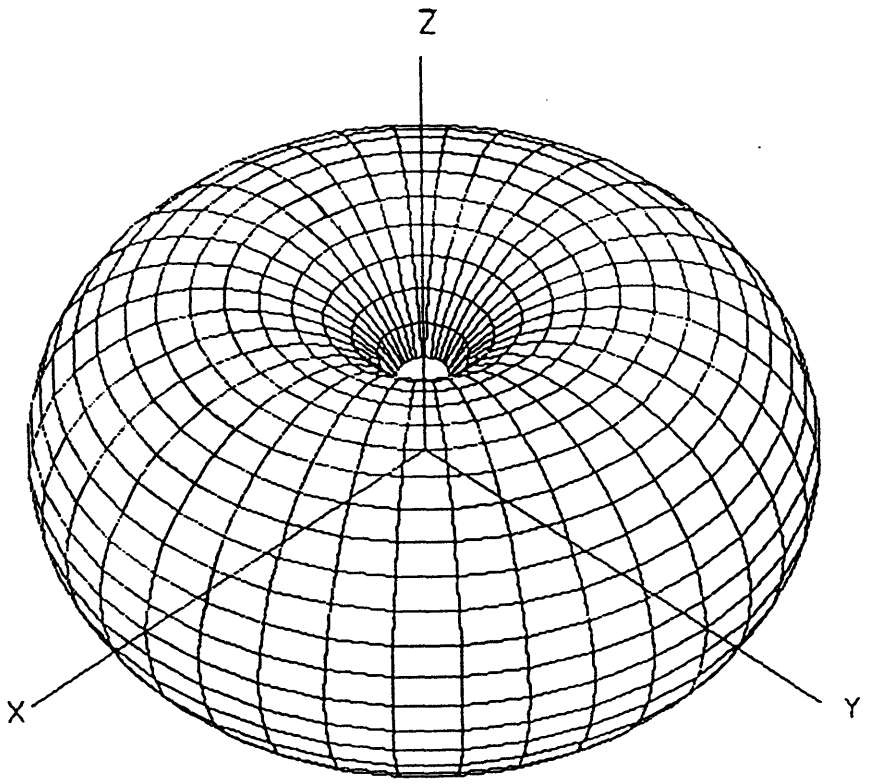

Figure C.1: Radiation field pattern for a scatterer ($ka << 1$).

The scattering cross section is

$$\Sigma_s = \frac{P_s}{\frac{1}{2}\frac{|E_0|^2}{\eta}} = \frac{8\pi}{3}(\frac{\epsilon_s - \epsilon}{\epsilon_s + 2\epsilon})^2 k^4 a^6 \tag{C.3}$$

C.2 Bistatic Scattering Pattern

If we move around the scatterer, the received E field will vary depending on the observation angle and the polarization of the receiver. Imagine that the induced dipole axis of a scatterer will be parallel to the incident $\overline{E}$ field; for an incident angle of $\theta_i = 0^o$, the dipole will be orientated horizontally and for $\theta_i = 30^o$, the dipole will make a 60^o degree elevation angle with the $\hat{z}$ axis. By transforming the local coordinates to the global coordinates and also taking into account the orientation of the scatterer, we can plot the normalized scattering returns as a function of azimuthal angle ϕ as shown in Figure C.2.

As we can see, the HH, VH and HV returns are symmetrical about $\phi = 90^o$, but is not true for the VV case. We observed the same trend in the numerical calculations in Chapter 2.

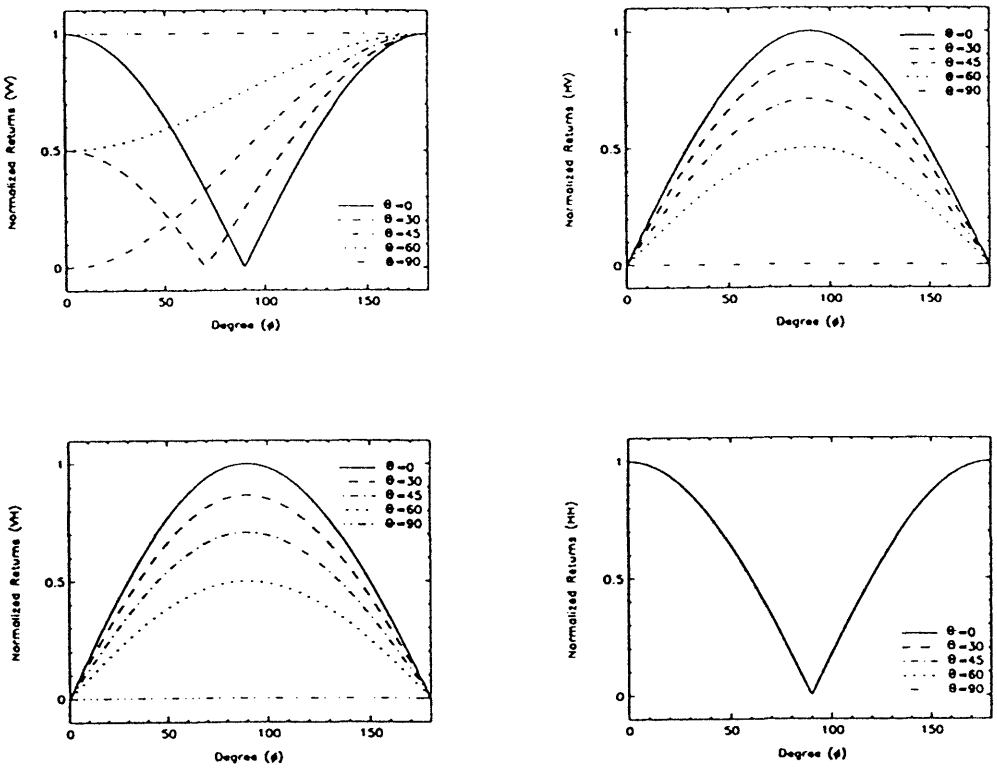

Figure C.2: Scattering for a single scatterer ($ka << 1$).

Bibliography

[1] Hall, D.K. and Martinec, J.(1985), *Remote Sensing of Ice and Snow*, Chapman and Hall, New York, NY.

[2] Massom, R. (1991), *Satellite Remote Sensing of Polar Region*, Belhave Press, London, U.K.

[3] Onstott, R.G., Moore, R.K. and Weeks W.F.(1979), "Surface-Based Scatterometer Results of Arctic Sea-Ice", *IEEE Trans. Geosci. Remote Sensing,* GE-17(3), pp. 78-85.

[4] Kim, Y.S., Moore, R.K., Onstott, R.G. and Gogineni(1985), "Towards Identification of Optimum Radar Parameters for Sea-Ice Monitoring", *J. Glaciol.,* 31(109), pp. 214-219.

[5] Kim, Y.S., Moore, R.K. and Onstott, R.G. (1984), "Theoretical and Experimental Study of Radar Back Scatter from Sea Ice", *RSL Tech. Rep. 331-37,* University of Kansas Center for Research, Inc., Lawrence , Kansas.

[6] Lin, F.C (1988), "Theoretical Models for Microwave Remote Sensing of Snow-covered Sea Ice", *Ph.D. Thesis,* Department of Physics, Massachusetts Institute of Technology, Cambridge MA.

[7] Drinkwater, M.K. (1989), "LIMEX'87 Ice Surface Characteristics : Implications for C-Band SAR Backscatter Signatures", *IEEE Trans. Geosci. Remote Sensing,* GE-27(5), pp. 501-513.

[8] Livingstone, C.E. and Drinkwater, M.K. (1991), "Springtime C-Band SAR Backscatter Signatures of Labrador Sea Marginal Ice : Measurements versus Modeling Predictions", *IEEE Trans. Geosci. Remote Sensing,* GE-29(1), pp. 29-41.

[9] Bredow, J.W. and Gogineni, S. (1990), "Comparison of Measurements and

Theory For Backscatter from Bare and Snow-Covered Saline Ice", *IEEE Trans. Geosci. Remote Sensing,* GE-28(4), pp. 456-463.

[10] Onstott, R.G. (1992), "Examination of the Physical, Electrical, and Microwave Evolution of Sea Water Into Young Ice", *IGARSS'92 Conf. Proc.,* pp. 1259-1261.

[11] Hosseinmostafa, R. and Lytle, V. (1992), "Comparison of Radar Backscatter from Antarctic and Arctic Sea Ice", *IGARSS'92 Conf. Proc.,* pp. 1533-1535.

[12] Toikka, M. and Hallikainen, M. (1992), "Radar Backscatter Signatures of Baltic Sea Ice", *IGARSS'92 Conf. Proc.,* pp. 1527-1529.

[13] Ulander, L.M.H and Carlstr; A. (1992), "C-Band Signatures of Old Ice in the Central Arctic", *IGARSS'92 Conf. Proc.,* pp. 958-960.

[14] Golden, K.M. *et. al,* (1993), "Electromagnetic Properties of Sea Ice, Year 1:Theory Summary", *Technical Report,* The Office of Naval Research.

[15] Tooma, S.G., Mennella, R.A., Hollinger, J.P. and Ketchum, R.D. (1975), "Comparison of Sea-Ice Type Identification between Airborne Dual-Frequency Passive Microwave Radiometry and Standard Laser Infrared Techniques", *J. Glaciol.,* 15(73), pp. 225-239.

[16] Rotman, S.R., Fisher, A.D. and Staelin, D.H. (1981), "Analysis of Multiple-Angle Microwave Observations of Snow and Ice Using Cluster- Analysis Techniques", *J. Glaciol.,* 27(95), pp. 89-97.

[17] Tiuri, M., Hallikainen, M. and Lääperi, A. (1978), "Radiometer Studies of Low-Salinity Sea Ice", *Boundary-Layer Meteorology,* 13, pp. 361-371.

[18] Carsey, F.D. and Pihos, G. (1989), "Beaufort-Chukchi Seas Summer and Fall ice Margin Data From Seasat: Conditions With Similarities to the Labrador Sea", *IEEE Trans. Geosci. Remote Sensing,* GE-27(5), pp. 541-550.

[19] Cavlieri, D.J., Gloersen, P. and Wilheit, T.T.J. (1986), "Aircraft and Satellite Passive Microwave Observations of the Bering Sea Ice Cover During MIZEX West", *IEEE Trans. Geosci. Remote Sensing,* GE-24(3), pp. 541-550.

[20] Grenfell, T.C. (1986), "Surface-Based Passive Microwave Observations of Sea Ice in the Bering and Greenland Seas", *IEEE Trans. Geosci. Remote Sensing,* GE-24(3), pp. 378-382.

[21] Swift, C.T., Dehority, D.C., Tanner, A.B. and McIntosh, R.E. (1986), "Passive Microwave Spectral Emission from Saline Ice at C-Band during the Growth Phase", *IEEE Trans. Geosci. Remote Sensing,* GE-24(6), pp. 840-848.

[22] Grenfell, T.C., Winebrenner and Wensnahan, M.R. (1992), "Passive Microwave signatures of Simulated Pancake Ice and Young Pressure Ridges", *IGARSS'92 Conf. Proc.,* pp. 1253-1255.

[23] Gray, A.L. , Hawkins, R.K., Livingstone, C.E., Arsenault, L.D. and Johnstone, W.M. (1982), "Simultaneous Scatterometer and Radiometer Measurements of Sea-Ice Microwave Signatures", *IEEE J. Oceanic Engineer.,* OE-7(1), pp. 20-32.

[24] Livingstone, C.E., Keshava, P.S. and Gray, A.L. (1987), "Seasonal and Regional Variations of Active/Passive Microwave Signature of Sea Ice", *IEEE Trans. Geosci. Remote Sensing,* GE-25(2), pp. 159-173.

[25] Pounder, E.R. (1965), *The Physics of Ice* , Prgamon Press Ltd., New York, NY.

[26] Weeks, W. and Ackley, S. (1982), *The Growth, Properties and Structure of Sea Ice, CRREL Monograph 82-1,* US Army CRREL, Hanover, NH.

[27] Strogryn, A. and Desargant, G.J. (1982) "The Dielectric Properties of Brine in Sea Ice at Microwave Frequencies", *IEEE Trans. Ant. Propag.,* AP-33(5), pp. 523-532.

[28] Strogryn, A. (1987), "An Analysis of the Tensor Dielectric Constant of Sea Ice at Microwave Frequency", *IEEE Trans. Geosci. Remote Sensing,* GE-25(2), pp. 147-157.

[29] Arcone, S.A., Gow, A.J. and Mcgrew, S.(1986) "Microwave Dielectric, Structural, and Salinity Properties of Simulated Sea Ice", *IEEE Trans. Geosci. Remote Sensing,* GE-24(6), pp. 832-838.

[30] Hallikainen, M. (1992), "Review of the Microwave Dielectric and Extinction Properties of Sea Ice and Snow", *IGARSS'92 Conf. Proc.,* pp. 961-965.

[31] Nakawo, M. and Sinha, N.K. (1981), "Growth Rate and Salinity Profile of First-Year Sea Ice in the High Antarctic", *J. Glaciology,* 27(96), pp. 315-330.

[32] Nghiem, S.V (1991), "Electromagnetic Wave Models for Polarimetric Remote

Sensing of Geophysical Media", *Ph.D. Thesis,* Department of Electrical Engineering and Computer Science, Massachusetts Institute of Technology, Cambridge MA.

[33] Zuniga, M.A., Habash, T.M. and Kong J.A. (1979), "Active Remote Sensing of a Layered Random Media", *IEEE Trans. Geosci. Remote Sensing,* GE-17(4), pp. 296-302.

[34] Tsang, L., Kong, J.A. and Newton, R.W. (1982), "Application of Strong Fluctuation Random Medium Theory to Scattering of Electromagnetic Waves from a Halfspace of Dielectric Mixture", *IEEE Trans. Ant. Propagat.,* AP-30-2, pp. 292-302.

[35] Tsang, L., Kong, J.A. and Newton, R.W. (1981), "Application of Strong Fluctuation Random Medium Theory to Scattering of Electromagnetic Waves from a Vegetation-Like Half Space", *IEEE Trans. Geosci. Remote Sensing,* GE-19(1), pp. 62-69.

[36] Fung, A.K. and Fung, H.S.(1977), "Application of First-Order Renormalization Me-thod to Scattering from a Vegetation-Like Half Space", *IEEE Trans. Geosci. Remote Sensing,* GE-15(4), pp. 189-195.

[37] Lang, R.H. (1981), "Electromagnetic Backscattering from a Sparse Distribution of Lossy Dielectric Scatterers", *Radio Science,* 16-1, pp. 15-30.

[38] Borgeaud, M., Kong, J.A. and Lin , F.C. (1986), "Microwave Remote Sensing of Snow-covered Sea Ice", *IGARSS'86 Conf. Proc.,* pp. 73-89.

[39] Borgeaud, M., Nghiem, S.V., Shin, R.T. and Kong, J.A. (1989), "Theoretical Models for Polarimetric Microwave Remote Sensing of Earth Terrain", *J. Electromagnetic Waves and Applications,* 3-1, pp. 61-81.

[40] Lin, F.C. , Kong, J.A. and Shin, R.T. (1987), "Theoretical Models for Active and Passive Microwave Remote Sensing of Snow-covered Sea Ice", *IGARSS'87 Conf. Proc.,* pp. 1121-1125.

[41] Lee, J.K. and Kong, J.A. (1985), "Active Microwave Remote Sensing of an Anisotropic Random Medium Layer", *IEEE Trans. Geosci. Remote Sensing,* GE-23(6), pp. 910-923.

[42] Lee, J.K. and Kong, J.A. (1985), "Passive Microwave Remote Sensing of an Anisotropic Random Medium Layer", *IEEE Trans. Geosci. Remote Sensing,* GE-23(6), pp. 924-932.

[43] Tsang, L. and Kong, J.A. (1980), "Thermal Microwave Emission from a Three-Layer Random Medium with Three-Dimensional Variations", *IEEE Trans. Geosci. Remote Sensing,* GE-18(2), pp. 212-216.

[44] Tsang, L. and Kong, J.A., (1979), "Radiative Transfer Theory for Scattering by Layered Media", *J. Appl. Phys.,* 50(4), pp. 2465-2469.

[45] Coutu, P. (1993), "Radiative Transfer Theory for Active Remote Sensing of Sea Ice", *SM. Thesis*, Department of Electrical Engineering and Computer Science, Massachusetts Institute of Technology, Cambridge MA.

[46] Shin, R.T. and Kong, J.A. (1989), "Radiative Transfer Theory for Active Remote Sensing of Two-layer Random Media", pp. 359-417, *PIER1, Progress in Electromagnetics Research*, Elsevier, New York, NY

[47] Han, H.C. (1992), "Electromagnetic Wave Phenomena in Inhomogeneous and Aniso-tropic Media", *Ph.D. Thesis,* Department of Electrical Engineering and Computer Science, Massachusetts Institute of Technology, Cambridge MA.

[48] Shin, R.T. (1980), "Radiative Transfer Theory for Active Remote Sensing of Layered Homogeneous Media Containing Spherical Scatterers", *M.S. Thesis,* Department of Electrical Engineering and Computer Science, Massachusetts Institute of Technology, Cambridge MA.

[49] Shin, R.T. and Kong, J.A. (1981), "Radiative Transfer Theory for Active Remote Sensing of a Homogeneous Layer Containing Spherical Scatterers", *J. Appl. Phys.,* 6, pp. 4221-4230.

[50] Tsang, L., Kong, J.A. and Shin, R.T. (1984), "Radiative Transfer Theory for Active Sensing of a Layer of Nonspherical Scatterers", *Radio Science,* 19, pp. 629-642.

[51] Chuang, S.L., Kong, J.A. and Tsang, L. (1980), "Radiative Transfer Theory for Passive Microwave Remote Sensing of a Two-layer Random Medium With Cylindrical Structure", *J. Appl. Phys.,* 51-11, pp. 5588-5593.

[52] Ishimaru, A., Lesselier, D. and Yeh C. (1984), "Multiple Scattering Calculations for Nonspherical Particles Based on the Vector Radiative Transfer Theory", *Radio Science,* 19-5, pp. 1356-1366.

[53] Tsang, L., Kubacsi, M.C. and Kong, J.A. (1981), "Radiative Transfer Theory for Active Remote Sensing of a Layer of Small Ellipsoidal Scatterers", *Radio Science,* 16-3, pp. 321-329.

[54] Shin, R.T. and Kong, J.A. (1981), "Theory for Thermal Microwave Emission from a Homogeneous Layer with Rough Surfaces Containing Spherical Scatterers", *J. Geophys. Res.*, 87-B7, pp. 5566-5576.

[55] Shin, R.T. (1984), "Theoretical Models for Microwave Remote Sensing of Earth Terrain", *Ph.D. Thesis,* Department of Electrical Engineering and Computer Science, Massachusetts Institute of Technology, Cambridge MA.

[56] Chandrasekhar, S., (1960), *Radiative Transfer*, Dover, New York, NY.

[57] Tsang, L., Kong, J.A. and Shin, R.T. (1985), *Theory of Microwave Remote Sensing*, John Wiley Sons Inc., New York, NY.

[58] Ulaby, F.T., Moore, R.K. and Fung, A.K. (1982), *Microwave Remote Sensing Active and Passive*, Volume I-II-III, Addison-Wesley Publishing Company, Reading, MA.

[59] Yueh, H.A., Shin, R.T. and Kong, J.A. (1989), "Scattering from Randomly Perturbed Periodic and Quasiperiodic Surfaces", pp. 297-358, *PIER1, Progress in Electromagnetics Research*, Elsevier, New York, NY.

[60] Winebrenner D.P., Grenfell T.C. and Tsang, L. (1992), "On Microwave Sea Ice Signature Modeling: Connecting Models to the Real World", *IGARSS'92 Conf. Proc.,* pp. 1268-1270.

[61] Fung, A.K. Dawson M. and Tjuatja S. (1992), "An Analysis of Scattering from a Thin Saline Ice Layer", *IGARSS'92 Conf. Proc.,* pp. 1262-1264.

[62] Fung, A.K. (1982), "Application of a Combined Rough Surface and Volume Scattering Theory to Sea Ice and Snow Backscatter", *IEEE Trans. Geosci. Remote Sensing,* GE-20(4), pp. 528-536.

[63] Tsang, L. and Kong J.A. (1977), "Thermal Microwave Emission from a Random Homogeneous Layer over a Homogeneous Medium Using the Method of Invariant Imbedding", *Radio Science,* 12, pp. 185-195.

[64] Kong, J.A. (1990), *Electromagnetic Wave Theory*, John Wiley Sons Inc., New York, NY.

[65] Rice, S.O. (1951), "Reflection of Electromagnetic Waves from Slightly Rough Surfaces", *Commun. Pure Appl. Math.*, 4, pp. 351-378.

[66] Valenzuela, G.R. (1967), "Depolarization of EM Waves by Slightly Rough Surfaces", *IEEE Trans. Ant. Propagat.,* AP-15-4, pp. 552-557.

[67] Veysoglu, M.E., Yueh, H.A., Shin, R.T. and Kong, J.A. (1991), "Polarimetric Passive Remote Sensing of Periodic Surfaces", *J. Electromagnetic Waves and Applications,* 5-3, pp. 268-280.

[68] Carsey, F.D., (1992), *Microwave Remote Sensing of Sea Ice*, American Geophysical Union, Washington, DC

[69] Beaven, S.G. *et. al.*, (1993), "Radar Backscatter Measurements From Simulated Sea Ice During CRRELEX 90", *Technical Report*, RSL, Lawrence, Kansas.

[70] Zabel, I.H.H.and Jezek, K.C., (1993), "CRRELEX 93: Surface Roughness and Physical Properties Measurements", *Technical Report*, Byrd Polar Research Center, Columbus, Ohio.

[71] Perovich, D. K. and Gow, A. J., (1991), "A Statistical Description of the Microstructure of Young Sea Ice", *Journal of Geophysical Research*, Vol. 96, No. C9, PP. 16,943-16,953.

[72] Perovich, D. K., (1993), CRRELEX93 measurement data, Cold Region Research and Engineering Laboratory (CRREL).